STRUCTURAL AND TRANSPORT PROPERTIES OF

DIRECTLY ASSEMBLED NANOWIRES

By

BIROL OZTURK

Bachelor of Science
Bogazici University
Istanbul, Turkey
1999

Master of Science
Oklahoma State University
Stillwater, Oklahoma
2003

Submitted to the Faculty of the
Graduate College of the
Oklahoma State University
in partial fulfillment of
the requirements for
the Degree of
DOCTOR OF PHILOSOPHY
July, 2007

STRUCTURAL AND TRANSPORT PROPERTIES OF

DIRECTLY ASSEMBLED NANOWIRES

Dissertation Approved:

Dr. Bret N. Flanders

Thesis Adviser

Dr. Daniel R. Grischkowsky

Dr. John Mintmire

Dr. Albert T. Rosenberger

Dr. A. Gordon Emslie

Dean of the Graduate College

ACKNOWLEDGEMENTS

I would like to acknowledge many people for helping me during my doctoral work. I would like to especially thank my research advisor Dr. Bret N. Flanders for his supervision, financial support and motivation, he has provided throughout the course of this work. I would like to express my gratitude for the many helpful comments and suggestions, I have received from him in the preparation of this dissertation. It is a pleasure to thank Dr. Daniel Grischkowsky, Dr. Albert Rosenberger and Dr. John Mintmire for their time as members of my advisory committee. I would like to express my deep and sincere gratitude to colleagues Ishan Talukdar, Prem Thapa, Ghazal Behin-Aein, and Srinavasa Vennupasa for their contributions to this work and for their friendship. I would like to also thank Dr. Daniel Grischkowsky for providing valuable comments on the collaboration projects. The lithographic electrodes provided by Dr. Grischkowsky had a substantial effect in the quality of this work. I owe a special note of gratitude to Dr. Charles Blackledge and Dr. Tetsuya Mishima; this work would not have been possible without their inputs.

I am extremely grateful to my parents for their support, love, and care, they provided in my life. They have always been very supportive of my decisions. My final thanks go to my wife Münire and to my son Ömer. Münire has been a constant source of

support, motivation, encouragement, and enthusiasm to me. Ömer has given me joy and a new perspective in life. His never ending energy is a marvel and inspiration.

TABLE OF CONTENTS

LIST OF TABLES

LIST OF FIGURES

CHAPTER I

INTRODUCTION

Photolithography has been used extensively in the microfabrication industry and in fundamental research studies for decades. Photolithographic methods have improved very fast and are keeping up with the well-quoted Moore's Law.[1] In terms of high-volume fabrication, photolithography leads all other techniques with the capability of producing structurally and functionally reproducible 65 nm features.[3] However, there are inherent properties associated with this technique, limiting its application to fundamental nanoscience. For example, the minimum feature size that can be produced with conventional photolithography is defined by the diffraction-limit, constituting a challenge for further reduction of feature sizes with this method. Additionally, dopants are commonly used in order to alter electrical properties of the semiconductors. This process is essential for the functioning of the photolithographically fabricated devices. In the near future, the concentration of the dopants is expected to exceed the solid solubility[4] with the further reduction of dimensions of the semiconductor components. The excess amount of dopants will cause unwanted tunneling of electrons that generates leakage currents,[5] a major impediment to the proper functioning of devices. Such limitations have motivated the development of alternative methods for the fabrication of materials with reduced dimensions.

Nanotechnology is one such approach that has attracted much attention in the last 20 years. A widely accepted size-range for nanostructures is 1-100 nm. A key nano-fabrication strategy is the controlled assembly of individual nanostructures in a bottom-up fashion. While nanotechnology is not expected to replace photolithography in the near future, a wide and growing range of applications exploit the attractive properties of nanostructures and nanofabrication strategies. For example, due their small size and intriguing properties, nanostructures are foreseen as building blocks for microelectronics[6-8] and sensors.[9, 10] Likewise, carbon nanotubes (CNTs) have unprecedented properties: their Young's modulus was found to be in the terapascal range[11]; multi-walled carbon nanotubes exhibited a tensile strength up to 63 GPa, more than 50 times higher than steel[12]; and single-walled carbon nanotubes can be metallic or semiconducting depending on their diameter and chirality.[13-15] Due to these characteristics, CNTs are being used as components in numerous applications such as displays[16], logic circuits[17, 18], and high-strength fibers and sheets.[19, 20] The increasing interest in the use of nanostructures in biological applications has led to the formation of a new subfield, known as bionanotechnology. For instance, targeted drug delivery using nanostructures is a highly studied research area where the delivery of medication to exact location is the ultimate goal. Successful realization of this objective will assist in avoiding the side effects of the medication.[21] In a recent study, nanowires were used to form high-density field effect transistors (FETs) for the stimulation and clocking of neuronal signals in electrophysiological experiments. Such systems are useful in the studies of synaptic processes in neuronal networks. Another proposed application for these hybrid structures is the fabrication of flexible real-time cellular assays for drug

discovery and testing.[22] There are many other examples of application ideas for nanotechnology; however most of them have yet to be demonstrated.

In order to utilize nanostructures in applications, their properties must be characterized, understood and controlled. Investigations of nanostructured materials have resulted in the discovery of various novel phenomena. One example of such a finding is the size-dependent energy bandgaps of semiconductor nanoparticles. While bulk semiconductors have fixed energy-bandgap, the size of semiconductor nanoparticles can be tuned to control their bandgaps.[2] In a similar manner, the properties of metallic particles are substantially different than bulk metallic properties when the diameter is reduced to less than 100 nm. In this size range, gold is no longer a noble and unreactive metal; rather, gold nanoparticles with diameters 2 to 3 nm can actually catalyze chemical reactions.[23, 24] These new material characteristics depend on the size, shape and composition of nanostructures, where each nanofabrication method enables a degree of control over these properties.

Most proposed applications of nanostructures require a certain degree of assembly. To this end, two strategies are frequently employed: self and directed assembly. In self-assembly, the interactions between a particle, its neighbors, and possibly a substrate, induce spontaneous organization in the system. The interparticle potential is the fundamental property that dictates the nature of these interactions and the resulting ordering. A distinctive advantage of the self-assembly is that this approach enables large scale ordering with minimal effort. A detailed understanding of the

underlying factors in the self-assembly of nanostructures is essential for achieving efficient targeted ordering, and a significant amount of research has been done to address this issue.[2, 25-29] Moreover, the assembled nanostructures themselves are intriguing systems for a wide range of fundamental studies.[30, 31] For example, self-assembled superlattices have been shown to exhibit modified behavior compared to isolated nanostructures due to interparticle potential.[32]

The main disadvantage of self-assembly is that the rate of growth, shape, and position of the self-assembled superstructure cannot be controlled by the user. In an alternative approach, external forces are utilized in the directed-assembly methods in order to induce the assembly of nanostructures at desired locations. These external forces are generated by a variety of fields such as electric[31, 33], magnetic[34, 35] or liquid flow.[6] Consequently, the directed assembly methods provide a higher degree of control over the ordering of nanostructures compared to self-assembly methods. Of the many possible nanoparticle-shapes, nanowires and nanotubes are the most widely used samples in transport experiments and device-applications. Particularly, metallic nanowires are ideal samples for a variety of 1D transport experiments such as diameter-dependent resistivity[24], Kondo Effect[36], 1D superconductivity[37] and spintronics.[38] However, reliable measurements require structural uniformity, diameter-tunability and low resistance-interconnecting of nanowires with external circuitry. Thus, establishment of methods enabling facile fabrication of nanowires with these properties is of great importance to nanoscience.

There has been vigorous research on the development of nanowire-fabrication techniques. Vapor-liquid-solid (VLS)[39-47], wet-chemical synthesis[2, 25, 33, 48, 49], and templated growth[50] are examples of the most frequently used techniques. Vapor-liquid-solid growth has the advantage of producing high quality nanowires of crystalline nature in most cases. In this technique, the vapor form of the source material is transferred onto catalyst nanoclusters such as gold nanoparticles. While the substrate is heated in order to form a liquid droplet of gold and substrate material, the source vapor enters these liquid droplets, saturates and solidifies at the liquid-solid boundary. The nanowires grow vertically on the substrate surface beneath each droplet.[46, 51] In VLS growth, the diameters of the nanowires as well as their growth axes are correlated with the size of the catalyst nanostructures.[52-54] Thus, the catalyst size control enables tuning of nanowire diameters. However, a distribution of nanowire diameters is inevitable even when catalysts with monodisperse size distributions are used.[52, 53] Templated growth is another type of commonly used nanowire fabrication method, where porous substrates[55, 56], DNA[57, 58], viruses[59], and other biomolecules[60] have been used as templates. The diameter control of nanowires in templated growth is enabled through the selection of templates with desired dimensions. While the diameter of the DNA is commonly reported as ~2 nm,[61] the porous substrates, the naturally occurring viruses and biomolecules are available with a range of size distributions, providing a reasonably wide-range of diameter-control of nanowires in templated growth. Wet-chemical synthesis methods are widely employed in the fabrication of nanostructures with a broad range of shapes including nanowires.[27] In most wet-chemical methods, stabilizers are used in order to encapsulate nanostructures and they alter the physical and chemical properties of the

nanostructure core material.[62] While these alterations can be useful in various applications,[25, 63, 64] the insulating nature of stabilizers reduce the conductivity of metallic nanostructures.[31] Achieving monodisperse size distributions of nanostructures is a challenging issue regarding the wet-chemical synthesis methods.[65]

The above-cited nanowire fabrication strategies have a particular limitation in common. Most applications of nanowires are based on their use as components in electronic circuits. Thus, nanowires have to be interfaced with external electrodes in order to characterize their charge-transport properties. *A major drawback of the described nanofabrication techniques is the requirement of secondary processing steps for connecting the nanowires to the external circuitry.* To this end, a common method is the placement of nanowires on a substrate, followed by the fabrication of electrodes via optical lithography[7, 66, 67]. This method is known as "blind sampling" and its success depends on the probability of properly placing electrodes on the targeted nanowires. Sophisticated equipment, such as e-beam lithography, can be used for the controlled deposition of electrodes on an individual nanowire.[68] Although this approach is helpful for electrical characterization of individual samples, it is not useful for the large-scale fabrication of functional devices. Scanning probe microscopy[67, 69], liquid flow[6] and Langmuir-Blodgett[44] techniques are other types of methods that are used to align nanowires on a substrate surface prior to electrode deposition. A critical issue regarding these methods is the difficulty of controlling electrical properties of the electrode-nanowire junctions. The contact resistances of these junctions are usually high, causing non-linear current-voltage behavior.[70] Consequently, this effect inhibits the efficient

characterization of the charge-transport properties of the nanowires and their use in applications.[71-73] Focused-ion-beam milling[58, 74] or annealing[75] are among the further steps, employed to reduce the high resistances of the contacts.

To circumvent the difficulty of synthesizing nanostructures and interconnecting them with electrodes in separate steps, a variety of techniques are being developed that directly grow and interconnect the nanostructures in a single step. As a directed assembly method, dielectrophoresis[76] is proving to be useful, as it allows for simple interfacing and characterization of nanostructures. In dielectrophoresis, a stock solution containing the particles is deposited across a pair of electrodes. The application of alternating voltage to the electrodes produces electric field gradients in the interelectrode region. These gradients induce the dielectrophoretic forces on the particles. The inhomogenities on flat electrode surfaces or at tips of the protruded electrodes produce electric field maxima near the biased electrode. When the strength of the dielectrophoretic trapping force exceeds Brownian motion, the particle-field interactions draw the particles to these field maxima and populate these regions. Particles with a polarizable nature become dipolar, and the heel-to-toe chaining of particles into an interconnect that spans the gap between electrodes is induced. This occurrence is illustrated in Figure I.1 for 1 μm diameter polymer spheres (see caption for details).[33, 77-80] We employed dielectrophoresis to form interconnects from semiconductor CdS nanoparticles and gold nanorods.[31, 33] Detailed structural characterization and charge transport properties of these interconnects are explained in the following chapters. A

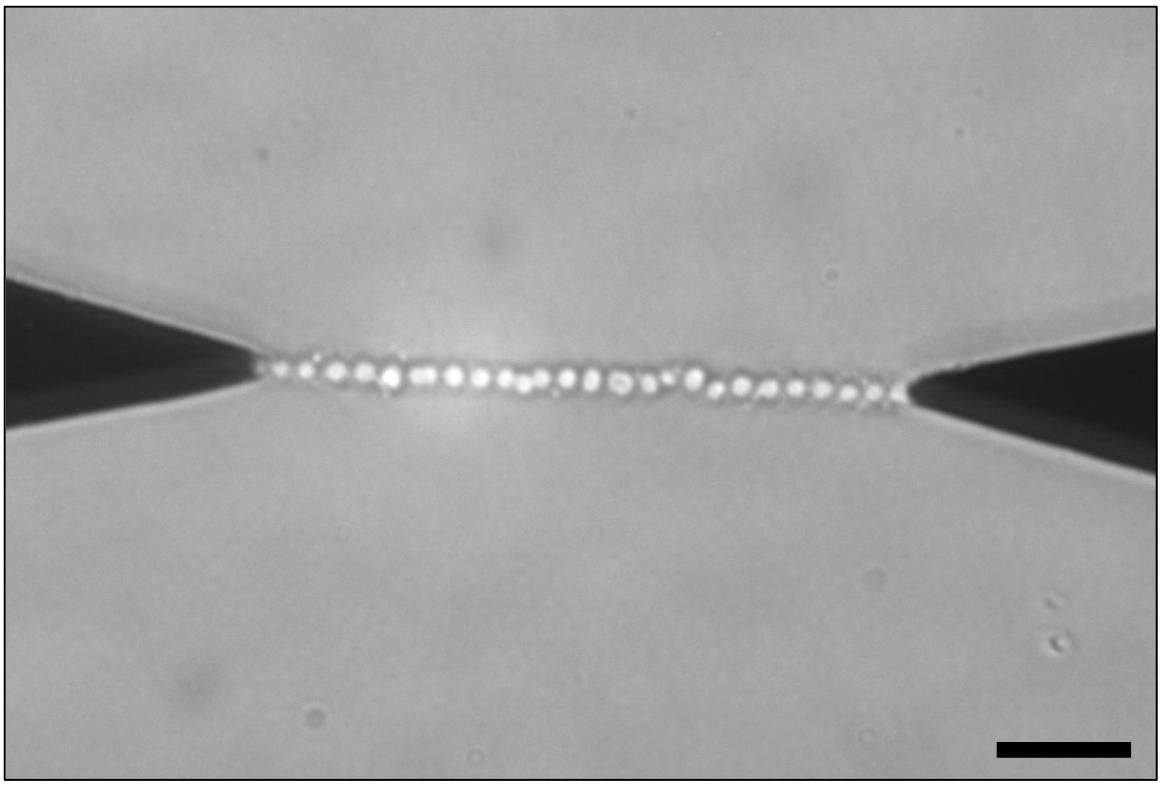

Figure I.1. Optical micrograph of a dielectrophoretically formed interconnect from ~1 μm diameter polymer spheres. The protruded tips on each side of the image are lithographic electrodes. The stock solution was diluted and deposited across the electrode gap. Upon the application of 1 MHz, ±25 V square wave signal to the electrodes, the particles start chaining at the biased electrode and form the interconnect. Scale bar represents 10 μm. (Unpublished result)

distinctive approach in our experiments was the use of a protruded electrode-design that forms non-uniform electric fields in the interelectrode region upon the application of voltage. This enabled the targeted placement of interconnects between the protruded electrode tips (Figure I.1) as opposed to multiple wires between parallel electrodes.[31, 79, 81]

Although the dielectrophoretic fabrication of interconnects from nanostructures is an attractive route, the nanoparticulate structure of these interconnects limits their conductivity.[31] While such interconnects may prove useful in devices like variable capacitors[82], highly conductive, metallic nanowires are essential components in nanoelectronics. In 2005, Haynie and coworkers demonstrated the electrochemical fabrication of multiple palladium nanowires from palladium acetate solutions.[81] More recently, we developed a method to fabricate individual crystalline metallic nanowires from simple salt solutions between targeted points in external circuitry.[83, 84] This technique is called *Directed Electrochemical Nanowire Assembly* (*DENA*). This approach differs from dielectrophoretic assembly in that simple salt solutions were used as the nanowire growth medium. This allows for the removal of the nanoparticle synthesis step, thereby simplifying the fabrication-procedure. The DENA technique enables the single-step growth and interconnecting of crystalline diameter-tunable nanowires with external electrodes and the wire composition can be chosen from a wide variety of metals such as indium, gold, nickel, cobalt, copper, silver, zinc, and lead. Finally, we demonstrated that the DENA-grown gold nanowires have low electrode-nanowire contact resistances of the order of ~10 Ω. To our best knowledge, such small contact resistances are not attainable by any single-step growth and interconnecting

technique.[84] Due to these properties, DENA-grown nanowires are ideal samples for the aforementioned 1D transport experiments. Motivated by this idea, DENA-grown gold nanowires were employed in diameter-dependent resistivity studies. Chapter VIII summarizes the preliminary results of these studies.

I.1 Organization of the thesis

As described above, the interparticle potential plays a critical role in the self-assembly of nanostructures. Thus, we initially probed this potential by performing quantitative film balance studies of trioctylphosphine oxide (TOPO) stabilized CdSe nanoparticles. In these experiments, self-assembly was employed in the organization of the nanoparticles at the air-water interface. This study demonstrated that CdSe nanoparticles of a given size behave as particles of smaller diameter in generating surface pressure. This behavior was attributed to an attractive component of interparticle potential. The dipolar potential is the most probable candidate. This work is presented in Chapter II.

The dielectrophoretic formation of interconnects from nanostructured building blocks is an example of the directed-assembly approach. Chapter III details the dielectrophoretic fabrication of CdS interconnects from 3.7 nm CdS nanoparticles. The mechanism of interconnect formation is also presented. Chapter IV is about the dielectrophoretic fabrication of gold nanorod interconnects and their transport properties. A detailed analysis of the charge conduction mechanism in these gold nanorod interconnects is provided, where we observed Coulomb-Blockade behavior at low

temperatures. As the results in Chapters III and IV showed, dielectrophoretically fabricated interconnects are nanostructured, limiting their conductivity.

The need for highly conductive and structurally uniform nanowires in fundamental research and device applications motivated the development of the DENA technique. In chapter V, the DENA technique is introduced by its application to the fabrication of indium nanowires. Electron diffraction based structural analysis showed that the DENA-grown indium nanowires are near single-crystalline. Further experiments and theoretical analysis have helped to gain an insight into the DENA mechanism. Chapter VI covers the mechanism of diameter-tunable nanowire growth with the DENA technique. The frequency of the growth voltage was observed to be the key parameter to control the diameters of DENA-grown indium and gold nanowires. A diffusion-limited growth mechanism for this behavior is also described. Initially DENA-grown nanowires exhibited high-contact resistance interconnecting with external electrodes. A feedback controlled growth voltage termination method was developed which helped to realize low contact resistance interconnecting of the DENA-grown gold nanowires with the external electrodes. DENA growth and structural characterization of these gold nanowires are presented in Chapter VII. After this further refinement by lowering the electrode-nanowire contact resistances, the DENA-grown nanowires became ideal samples for 1D transport experiments. Thus, the DENA-grown gold nanowires were used in the diameter-dependent resistivity measurements. Chapter VIII presents the recent results of these measurements. Chapter IX includes conclusions and future directions.

Chapter II: Hard-Disk Behavior and Beyond in Langmuir Films of CdSe Nanoparticles

Reproduced with permission from B. Ozturk, G. Behin-Aein, and B.N. Flanders, *Langmuir*, 21, 4452-4457, 2005.

CHAPTER II

HARD-DISK BEHAVIOR AND BEYOND IN LANGMUIR FILMS OF CDSE NANOPARTICLES

Abstract

Harnessing the spontaneous behavior of a population of particles is an attractive approach to the fabrication of targeted nanostructures. Underlying this goal is the interparticle potential, as it dictates the spontaneous behavior of the system. To this end, we present methodology for using quantitative film balance studies of trioctylphosphine oxide (TOPO) stabilized CdSe nanoparticles to determine their effective interparticle potential on the air-water interface. A simple protocol for reducing the quantity of excess TOPO to negligible levels of surface activity is established. In studying clean populations of 2.08, 2.22, 2.36, 2.49, 2.63, and 2.91 nm nanoparticles, quantitative agreement between their pressure-area isotherms and the Carnahan- Starling hard-disk equation of state is achieved. This analysis indicates that CdSe nanoparticles of a given diameter behave how hard disks with significantly smaller diameters would behave. This finding suggests that an attractive contribution to the interparticle potential, such as the dipolar potential, plays a significant role in the spontaneous organization of these particles.

II.1 Introduction

The production of nanoparticles with widely tunable properties has focused a substantial amount of effort on assembling these building blocks into targeted structures, such as miniaturized electronic devices[85-89] and sensors.[90-92] A significant portion of this effort focuses on controlling self-assembly in nanoparticle populations in order to develop device fabrication strategies that enable precise positioning but circumvent piecewise manipulation of the particles.[93, 94] At the heart of this goal lies the interparticle potential. This property determines the spontaneous organization of a population and, thus, figures prominently in the directed assembly of targeted structures from the population.[93] While insight into the interparticle potential in many types of nanoparticles is lacking, dispersions of CdSe nanoparticles have been found to possess substantial dipolar character.[95, 96] The extent to which this character overcomes Brownian motion to influence the spontaneous organization of these structures remains unknown. It is important that this gap be addressed because interactions of this nature underlie the dielectrophoretic assembly of interconnects,[97-99] so knowledge of the spontaneous behavior induced by the dipolar potential could serve as a guide in optimizing this assembly-strategy.

Monolayers of nanoparticles represent favorable systems for studying the interparticle potential due to their reduced dimensionality, as evidenced by the several recent investigations into the spontaneous organization of *metallic* nanoparticles.[100-103] *Floating* (*i.e.* Langmuir) monolayers present particularly intriguing opportunities for studying spontaneous assembly because the mobility afforded the particles by the liquid

interface allows them to organize in accordance with their interparticle potential and thermal energy. Langmuir-Blodgett (LB) films, by contrast, present the added challenge of characterizing the strong particle-substrate interactions. The unconstrained environment of Langmuir monolayers is especially important in studying the spontaneous organization of *semiconductor* nanoparticles because subtle interactions due to the permanently dipolar nature of these particles are expected to influence the spontaneous behavior;[95, 96, 104, 105] it would be difficult to identify this effect amongst the more complex range of interaction types associated with LB films. However, with the exception of a few recent studies, the spontaneous behavior of floating monolayers of *semiconductor* nanoparticles has been overlooked.[106, 107]

A major impediment to studying semiconductor nanoparticles at air-water interfaces is that these particles are often synthesized in trioctylphosphine oxide (TOPO) or other amphiphilic stabilizers. Because TOPO is a surfactant, trace amounts disrupt the interparticle potential-induced organization of these particles at these interfaces. Therefore, clean populations of surface-active particles are necessary before experimental interrogation of the spontaneous behavior of the populations can be reliably performed. The most direct means of interrogating the interparticle potential is to image the configurations into which particle populations assemble. This structure is directly related to the interparticle potential.[108] However, imaging techniques that can resolve individual particles, such as transmission electron microscopy or atomic force microscopy (AFM), are extremely difficult to implement at the air-water interface.[109] A notable exception is grazing incidence X-ray diffraction, which is routinely used to probe the nanoscopic

structure of Langmuir films.[110, 111] Attaining a working knowledge of the interparticle potential in nanoparticulate systems would be advantageous prior to initiating the collaborative effort that would be necessary to perform such diffractive studies. To this end, film balance techniques present an attractive, straight-forward means of probing the interparticle potential of nanoparticulate films, as has previously been done for copolymer films.[112]

In the following, we present a simple and effective protocol for reducing the quantity of excess TOPO to negligible levels of surface activity in size-dependent populations of CdSe nanoparticles. After demonstrating how the attainment of clean nanoparticle populations enables the measurement of quantitative pressure-area isotherms, we present a simple analysis formalism that is capable of identifying deviation from ideal hard-disk behavior in this system. Hence, in determining the extent to which CdSe nanoparticles behave like hard-disks, this study develops a working knowledge of the interparticle potential in Langmuir films composed of these particles. Ultimately, this outcome establishes a foundation for future, complementary studies of Langmuir-Blodgett films that will assess how the deposition process affects the interparticle potential-induced organization of the particles. This insight would facilitate the development of Langmuir-Blodgett techniques for depositing precisely structured nanoparticulate films, as well as dielectrophoretically-assembled interconnects onto solid substrates, capabilities that are required of viable device fabrication strategies.

II.2 Materials and Methods

We employed an established route to synthesizing CdSe nanoparticles[113, 114] that are dissolved in a mixture of Cd, Se, trioctylphosphine, and trioctylphosphine oxide (TOPO),[115] from which the nanoparticles must be separated. Conventional approaches to purification entail the addition of methanol to precipitate the particles, followed by separation and dissolution of the particles in 1-butanol.[115] A second washing with methanol precipitates the particles while retaining excess trioctylphosphine and TOPO in the liquid phase, and centrifugation isolates the precipitated nanoparticles. For many applications, it is sufficient to stop purification after two washing cycles. For quantitative Langmuir studies, it is necessary to further reduce the excess TOPO-content of the populations. In this study, this is done by exploiting the enhanced solubility of TOPO in methanol (1.154 g/ml) over the negligible solubility of TOPO-capped nanoparticles. That is, the precipitated populations were washed with methanol, stirred for five minutes, and centrifuged to precipitate the nanoparticles an additional five times, for a total of seven washing cycles. The clean particles were dissolved in chloroform, producing the nanoparticle stock solutions.

II.2.1 *Characterization of the Nanoparticle Populations*

The mean particle diameters of the stock populations were determined through UV-visible absorbance spectroscopy by invoking an empirical function established elsewhere.[116] The nanoparticle concentrations of these solutions were determined by employing diameter-dependent extinction coefficients for TOPO-capped CdSe

nanoparticles and Beer's law.[116, 117] These quantities are reported in Table II.1.

II.2.2 *Fluorescence Imaging of Langmuir Films*

Langmuir films of the nanoparticles were prepared for fluorescence imaging by drop-wise dispersion of the stock solutions onto the air-water interface of a homebuilt trough of fixed surface area until a target pressure of 11.0 ± 0.5 mN/m was reached. Imaging was commenced after 25 minutes, providing time for the surface pressure to stabilize and the solvent to evaporate. This trough was mounted on an inverted microscope (Leica, IRB), equipped with a mercury lamp and a 340-380 nm band-pass filter to narrow the spectral range of the excitation intensity. A 10× objective (Leica, 11506075) was used to collect emission from the diffusely illuminated film. A long-pass dichroic mirror (cutoff wavelength = 505 nm) removed residual excitation light from the collected light and directed the fluorescence to a high sensitivity digital camera (Hamamatsu, Orca ER II) where the 1.3 mm × 1.7 mm fluorescence images were captured.

II.2.3 *Atomic Force Microscopy-Based Imaging*

High resolution topographical images of the nanoparticulate films were attained by employing the Langmuir-Blodgett technique to deposit the nanoparticle films onto freshly cleaved mica substrates at targeted surface pressures. LB deposition was performed on the Langmuir trough discussed below. The topographical images were collected by a Veeco MultiMode atomic force microscope operating in tapping mode and

TABLE II.1.

KEY PROPERTIES OF THE CDSE NANOPARTICLE POPULATIONS

Soln.	Wavelength Abs. Max. (nm)	Mean Particle Diameter (nm)	Concentration (M)	Hard-disk Diameter (nm)
1	467	2.08	3.68×10^{-5}	1.63
2	486	2.22	4.70×10^{-5}	1.71
3	502	2.36	4.97×10^{-5}	1.92
4	514	2.49	7.51×10^{-5}	1.92
5	524	2.63	5.82×10^{-5}	2.31
6	543	2.91	3.11×10^{-5}	2.43

employing UltraSharp silicon-nitride tips (MikroMasch). This instrument was controlled by a Nanoscope IIIa control station. Image analysis was limited to flattening and adjustment of the contrast and color-level settings.

II.2.4 *Quantitative Pressure-Area Isotherms*

Isotherms of Langmuir films composed of 2.08, 2.22, 2.36, 2.49, 2.63, and 2.91 nm nanoparticles were measured on a two-barrier Langmuir trough (Nima Technology, 700BAM) equipped with a Wilhelmy surface pressure sensor (Nima, Type PS4). With the barriers fully separated, a small volume (typically 150 μl) of stock solution was dispersed onto the air-water interface of the trough. Independent knowledge of the particle concentrations of the stock solutions, attained through the optical absorbance studies, enabled measurement of quantitative isotherms in which the surface pressure was recorded as a function of the area-per-particle.

II.3 Results and Discussion

Figure II.1 displays the absorbance spectra of the nanoparticle stock solutions. These spectra were used to determine the mean particle diameters of the populations and the particle-concentrations of the stock solutions, as reported in Table II.1.

There are two approaches to monitoring the effects of the cleaning procedure on the nanoparticle populations: indirectly, by studying the supernatants from which the particles were separated, and directly, by studying the particles themselves. Here we do

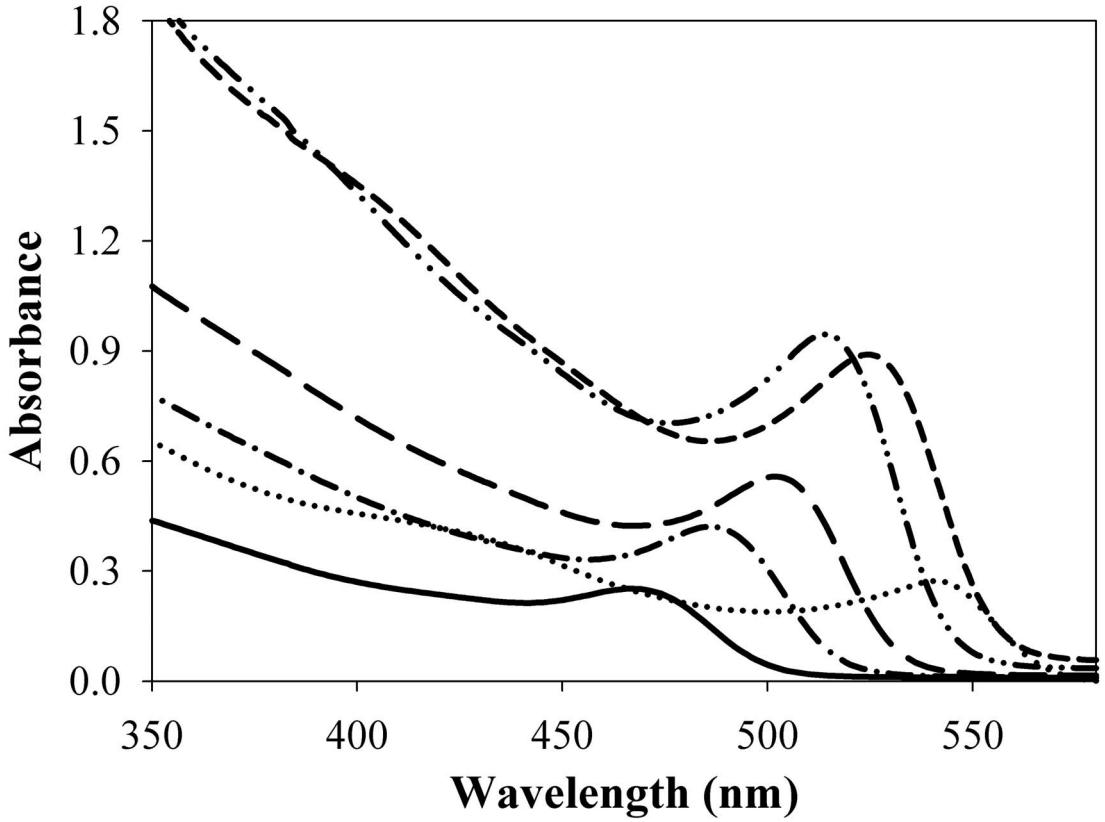

Figure II.1. Absorbance spectra of the series of TOPO-capped CdSe nanoparticles of varying mean particle size. The solid line denotes the 2.08 nm population, the dot-dashed line denotes the 2.22 nm population, the long-dashed line denotes the 2.36 nm population, the dot-dot-dashed line denotes the 2.49 nm population, the short-dashed line denotes the 2.63 nm population, and the dotted line denotes the 2.91 nm population. Matched quartz cells (Hellma) with 0.20 cm path lengths were used to obtain these spectra.

both. Pressure-area isotherms of the supernatants from successive washings of the 2.22 nm population are shown in Figures II.2a and II.2b. The data in Figure II.2a indicate that the primary contaminant in the nanoparticle populations is TOPO. That is, the filled circles depict an isotherm of a film cast from the supernatant of the third washing cycle. This isotherm exhibits a plateau at ~31 mN/m that extends indefinitely upon further compression of the film, an unusual profile that is characteristic of TOPO. To confirm this assignment, a pressure-area isotherm for a pure TOPO film is designated by the solid line. Its position along the horizontal axis was adjusted to coincide with the supernatant-isotherm. The high degree of overlap indicates that the major amphiphilic component of the supernatant is TOPO and that even after three washing cycles, a substantial quantity of TOPO is removed from the nanoparticle population.

The isotherms from the supernatants of six successive methanol washings are plotted in Figure II.2b. All exhibit the characteristic profile of TOPO. These data indicate that successive washing cycles removed diminishing amounts of TOPO from the populations. That is, larger supernatant volumes of the more heavily washed samples were required to populate the surface with measurable quantities of TOPO, as the trough can only be closed to a minimum area of 91 cm^2. Hence, to render the isotherms of the successive supernatants comparable while working around this minimum area-of-compression, the surface pressure was plotted against the logarithmic ratio of the trough-area to the supernatant-volume. The isotherms of the more heavily washed samples lie to the left of the lesser washed samples, indicating that the supernatants of successive

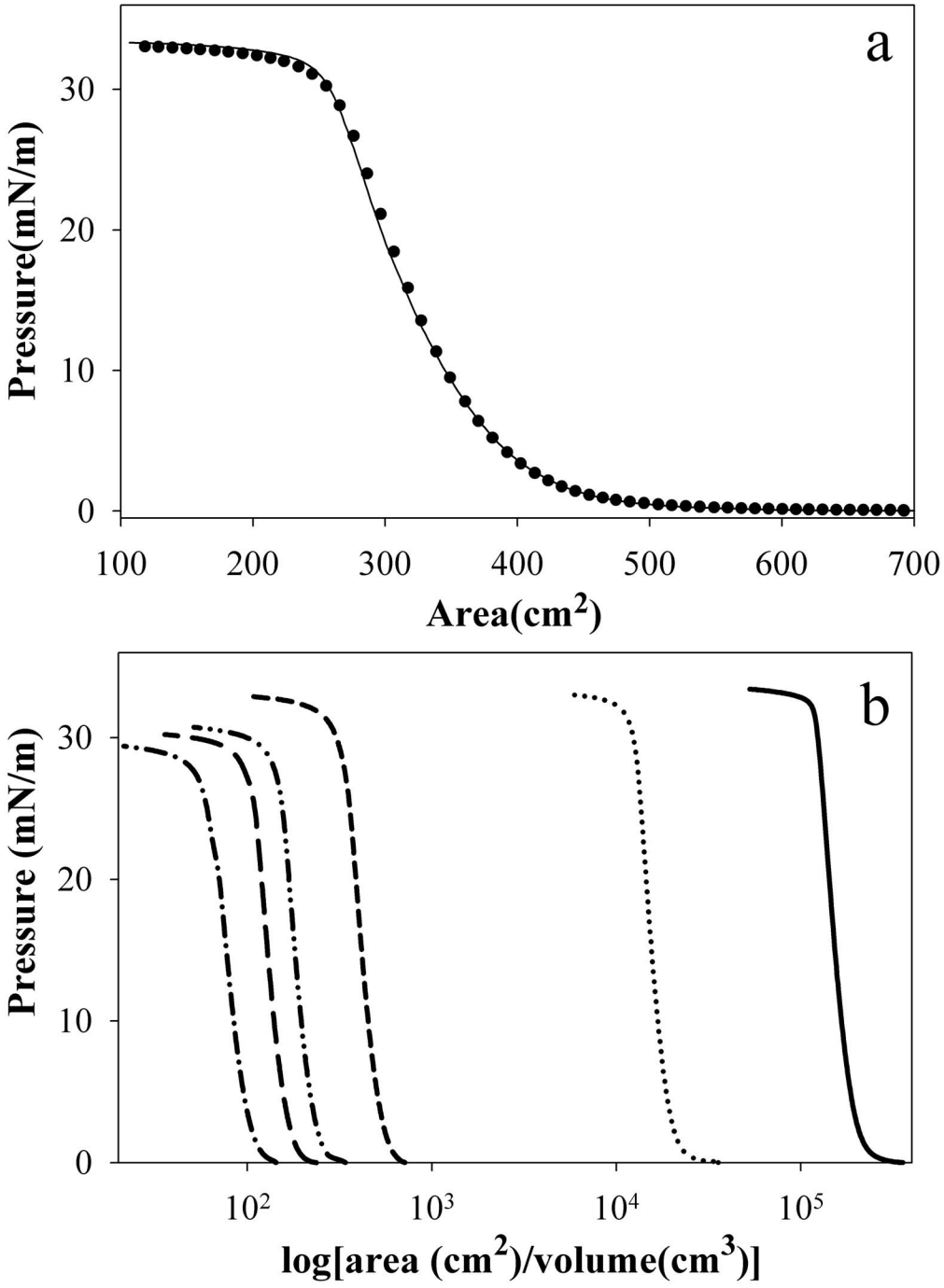

Figure II.2. (a) The filled circles denote a pressure-area isotherm for a film cast from the supernatant of the third washing cycle, and the solid line denotes an isotherm for a pure TOPO film. (b) Isotherms for films cast from the supernatants of the second (solid line), third (dotted line), fourth (medium- dashed line), fifth (dot-dot-dashed line), sixth (long-dashed line), and seventh (dot-dashed line) washing cycles.

washings contain decreasing quantities of TOPO. It is reasonable to conclude that this reduction in the TOPO-content across the series of supernatants reflects a commensurate reduction in the excess TOPO-content of the nanoparticle populations. To test this hypothesis, we have performed optical and topographical imaging of the nanoparticulate films at different points in the cleaning procedure in order to directly observe the cleansing effect on the populations.

The images in Figure II.3 depict 1.3 mm × 1.7 mm fluorescence micrographs of Langmuir films that were cast from the 2.22 nm nanoparticle population. The CdSe nanoparticles are the only fluorescent entities in these films; hence, the bright features indicate the presence of these particles. Figure II.3a depicts a film cast from a population that had been subjected to one washing cycle. The film is highly inhomogeneous, exhibiting a dark expanse in which a bright, ~1 mm globule resides. No thermal motion of the globule was observed, indicating that the dark expanse was densely populated with non-fluorescent material, holding the globule in place. Figure II.3b depicts a film cast from a population that had been subjected to three washing cycles. In contrast to Figure II.3a, most of this film exhibits fluorescence; however, ~30 μm-wide ribbons traverse the film, the fluorescent expanse exhibits biphasic contrast, and filaments of intense fluorescence coexist with both phases. Figure II.3c depicts a film cast from a population subjected to five washing cycles. With the exception of the dark ribbons and ~60 μm points of intense fluorescence (indicating nanoparticle clustering), the fluorescent expanse in which these features coexist is uniformly bright, and the film is noticeably more homogeneous than that of Figure II.3b. Figure II.3d depicts a film cast from a

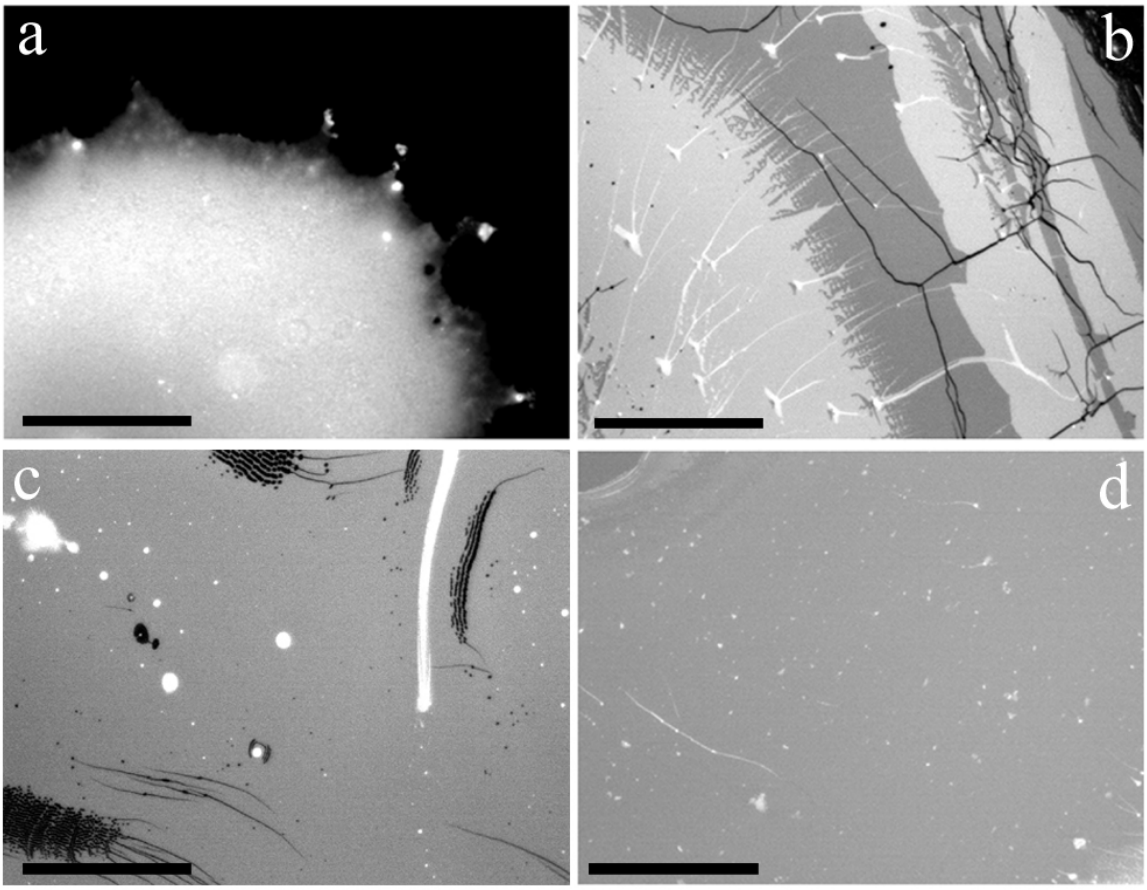

Figure II.3. Fluorescence micrographs (1.3 mm × 1.7 mm) of Langmuir films cast from the 2.22 nm nanoparticle populations after (a) one washing cycle, (b) three washing cycles, (c) five washing cycles, and (d) seven washing cycles. The films were prepared at surface pressures of 11.0 ± 0.5 mN/m, and the scale bars denote 0.5 mm.

population subjected to seven washing cycles. The dark ribbons are no longer apparent, and with the exception of ~30 μm features of anomalous brightness, the film exhibits uniform fluorescence intensity across the entire 1.3 mm × 1.7 mm field-of-view. This imaging study shows that the uniformity of the nanoparticle films increases with the number of washing cycles that the population has undergone. The correspondence between this emergence of film uniformity and the diminishing TOPO-content of the supernatants strongly suggests that TOPO is the primary contaminant that disrupts the spontaneous organization of these films. To verify that the washing procedure produces populations that are clean on the nanoscopic level, we have performed high resolution topographical imaging of these films as a function of washing cycle.

Figure II.4 illustrates a series of 400 nm × 400 nm topographical images of Langmuir-Blodgett films deposited onto mica substrates at a surface pressure of 5.0 mN/m. This series shows that the more times the population is washed, the better the AFM can resolve the 2.91 nm particles that constitute the films. Figure II.4a depicts a film that was deposited after the third washing cycle. This image exhibits both high (bright) and low (dark) regions each of which exhibits uniform topography. Individual nanoparticles are not discernible in this image. Figure II.4b represents a film that was deposited after the fifth washing cycle. Individual nanoparticles are identifiable in these regions. The low regions contain elongated shapes of intermediate brightness that tend to lay parallel to each other. While these features may correspond to TOPO, their nature remains unknown. The film in Figure II.4c was deposited after the seventh washing cycle. This image depicts high regions composed of clearly-resolved nanoparticles. The

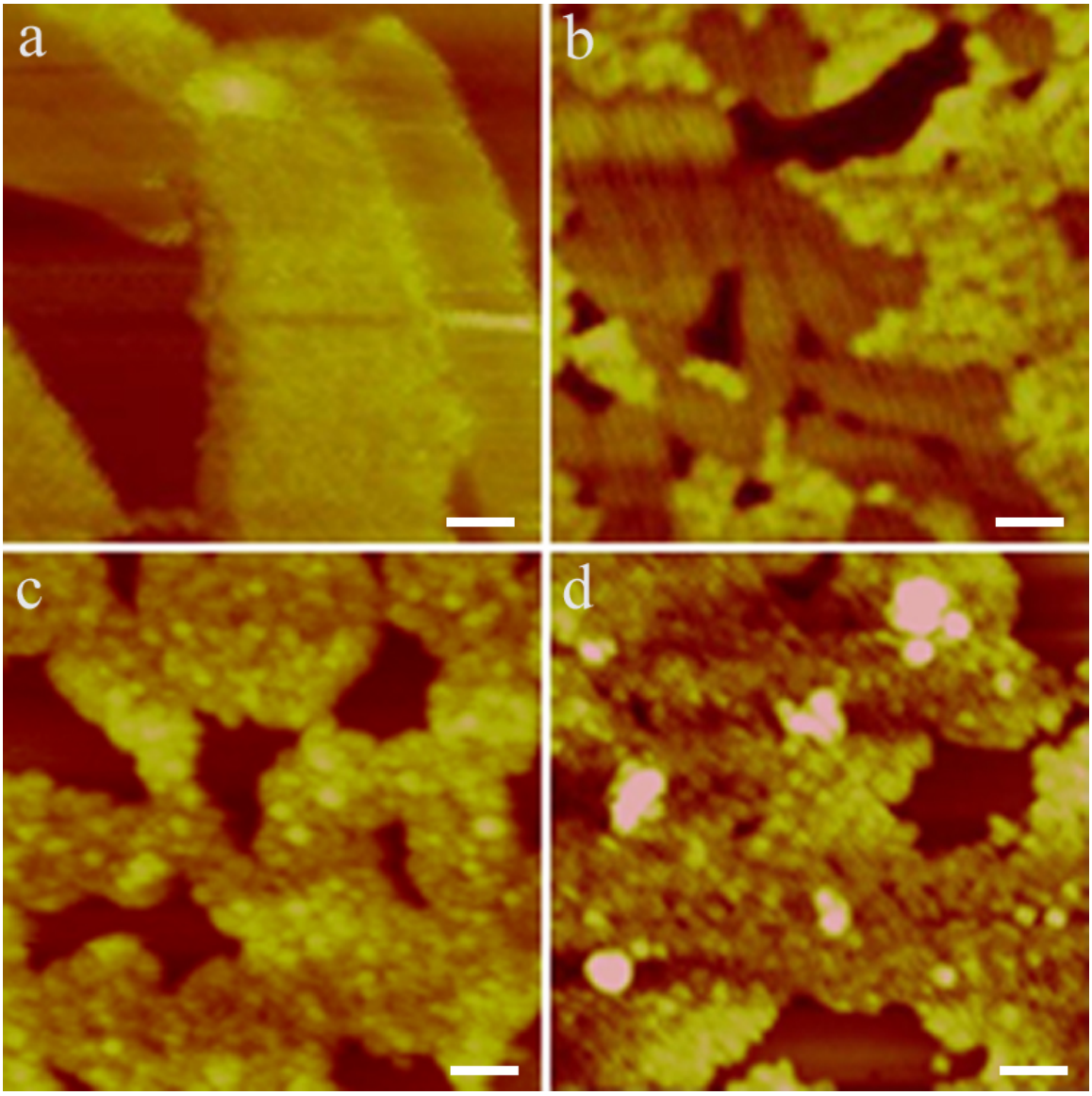

Figure II.4. Topographical images (400 nm × 400 nm) of Langmuir-Blodgett films of 2.91 nm nanoparticles deposited on mica at a surface pressure of 5.0 mN/m after (a) 3 washing cycles, (b) 5 washing cycles, (c) 7 washing cycles, and (d) 11 washing cycles. The scale bars denote 50 nm.

low regions are featureless, indicating that the material responsible for the elongated shapes in the low similar to Figure II.4c, suggesting that washing cycles eight through eleven do little to modify these populations. The emergence of nanoparticulate resolution across these series of images indicates that the succession of washing steps, particularly steps 1 through 7, removes excess TOPO from the populations, producing populations that are clean on the nanoscopic level. In extracting TOPO from these populations, it is possible that some TOPO molecules are removed from the nanoparticle surfaces. However, the nanoparticle populations remain fluorescent and maintain good surface activity for ~15 days after being subjected to the cleaning procedure. These properties would be compromised by the removal of significant amounts of the stabilizer. Hence, these observations indicate that the cleaning procedure mainly targets unbound TOPO for removal.

Figure II.5a exhibits pressure-area isotherms of films composed of cleaned 2.08, 2.22, 2.36, 2.49, 2.63, and 2.91 nm nanoparticles. Each isotherm exhibits a region of zero surface pressure at large area-per-particle that transitions to a monotonic rise in the surface pressure. This series of isotherms exhibits the following trend: the smaller the mean particle size, the smaller the area-per-particle at which lift-off occurs. This simple dependence resembles the hard-disk equation-of-state and, hence, a hard-disk fitting function was employed to analyze these isotherms. We have chosen the Carnahan-Starling expansion of the pressure of a 2D system of disks to fit our isothermal data.[118] This expansion closely approximates the known values for the virial coefficients of a hard-disk system,[119] and it has the virtue of being easily expanded to arbitrarily high

order. The functional form of this fitting equation is

$$\text{Surface Pressure} = k_B T\left(\rho + \sum_{k=2}^{25} B_k \rho^k\right). \qquad \text{(II.1)}$$

$k_B T$ is the thermal energy, ρ is inverse of the area-per-particle (*i.e.* ρ is the number density of particles), and B_k is the k^{th} virial coefficient attained in this expansion procedure. The explicit values for the coefficients that were employed in this study are reported elsewhere.[118] Because this expansion comprises a fitting function with only one adjustable parameter, the hard-disk diameter, of which the B_k are functions, this analysis formalism enables the extraction of unique values for the hard-disk diameters by fitting the measured isotherms. These quantities may be directly compared with the experimental values for the diameters of the nanoparticle populations, establishing a basis for unambiguously assessing the extent to which the hard-disk model represents CdSe nanoparticles.

Figure II.5b depicts the 0-10 mN/m regions of the fitted isotherms for the 2.08, 2.22, 2.36, 2.63, and 2.91 nm populations. For the sake of clarity, the isotherm of the 2.49 nm population is not shown, as it overlaps significantly with that of the 2.36 nm population in this pressure region. It is apparent that Equation. (II.1) closely fits the measured isotherms within experimental error, enabling extraction of unique values for the hard-disk diameters. Figure II.5c plots these fit-extracted quantities against the experimental values for the mean core-diameters of the nanoparticles. The solid line denotes a best-fit to the points under the constraint of unity-slope; the y-intercept, which

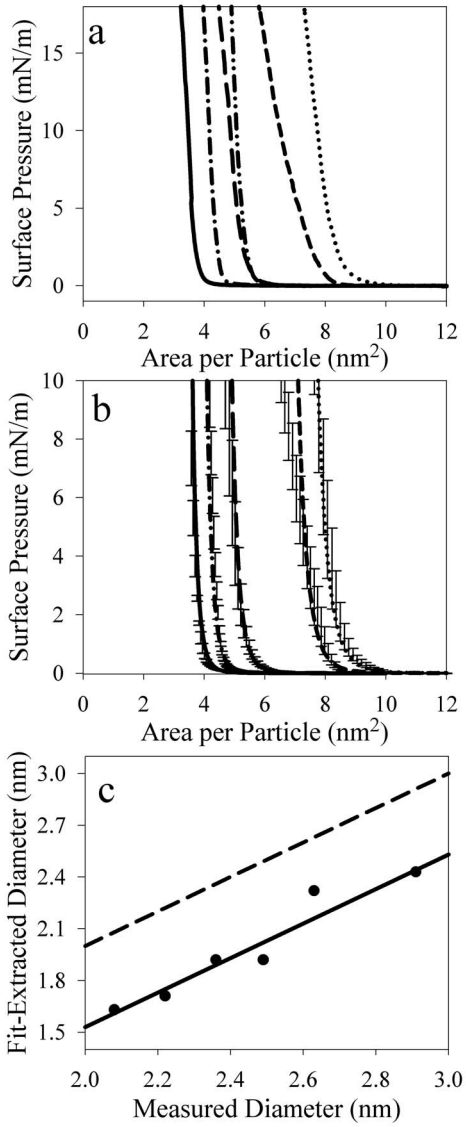

Figure II.5. (a) Pressure-area isotherms of clean populations of TOPO-capped semiconductor nanoparticles. The solid line corresponds to the population of 2.08 nm particles, the dot-dashed line corresponds to the population of 2.22 nm particles, the long-dashed line corresponds to the population of 2.36 nm particles, the dot-dot-dashed line corresponds to the population of 2.49 nm particles, the short-dashed line corresponds to the population of 2.63 nm particles, and the dotted line corresponds to the population of 2.91 nm particles. (b) The 0-10.0 mN/m regions of the isotherms for the 2.08 nm (solid line), 2.22 nm (dot-dashed line), 2.49 nm (long-dashed line), 2.63 nm (short-dashed line), and 2.91 nm (dotted line) populations of CdSe nanoparticles. For the sake of clarity, every third data point is shown. The lines represent the hard-disk fitting functions. The error bars represent the standard deviation of the mean of three independent measurements. (c) The fit-extracted values for the particle diameter plotted against the experimentally determined values for the particle diameters. The solid line denotes a best linear fit to the data, and the dashed line denotes the line expected for the ideal case of pure hard-disk interaction.

was freely adjustable, was determined to be -0.47 nm. This linear-fit, as characterized by an *R*-squared fitting factor of 0.93, establishes a direct correlation between the theoretical and experimental particle sizes and indicates that the hard-disk potential contributes significantly to the total interparticle potential of these 2D populations. However, pure hard-disk behavior would yield a y-intercept of zero, denoting perfect correlation between fit-extracted and experimental diameters; TOPO-capped particles would be expected to yield a slightly positive y-intercept to account for the capping layer thickness that is ignored in the experimental determination of the diameter. The dashed line in Figure II.5c depicts a line with a y-intercept of zero (and unity slope). Clearly it does not fit the data, and clearly a *negative* y-intercept is needed. The negative y-intercept found in this study indicates that in generating surface pressure, CdSe nanoparticles of a given size behave as if their diameters are smaller, by ~0.5 nm. This finding suggests that an attractive contribution to the interparticle potential is significant in these populations, a likely candidate for which is the dipolar potential identified in earlier studies.

This insight into the interparticle potential in Langmuir films of CdSe nanoparticles is significant because it will enable investigation into the effect of Langmuir-Blodgett deposition of such populations onto solid substrates. Figure II.6 illustrates a representative AFM image of 2.91 nm particles deposited at a surface pressure of 300 μN/m onto a freshly cleaved mica substrate. The random configuration of particles in Figure II.6a is consistent with their spatial distribution being determined solely by the hard-disk potential: as the hard-disk potential carries no attractive component, low densities of hard-disks exhibit random organization. Figure II.6b

illustrates a typical AFM image of the 2.91 nm particles deposited at a surface pressure of 5.0 mN/m. In contrast to Figure II.6a, this image depicts extensive particle-aggregation. An intriguing interpretation is that at low pressures, the mean particle spacing exceeds the distance at which the interparticle potential attracts a neighboring particle, whereas at high pressures, the mean particle spacing falls within this distance, and particle aggregation ensues. This interpretation awaits explicit determination of the occupancy statistics for the deposited particles,[120] correlation of the deposited number densities with those measured isothermally on the air-water interface, and characterization of how these properties depend on the surface pressure. However, Figure II.6 illustrates the potential of LB techniques for the deposition of nanostructured materials with precise control over the interparticle spacing. This capability would expedite the production of gas sensors based on whispering-gallery mode microlasers,[91] and it could provide a novel means of interrogating the nature of superlattice formation in 2D nanoparticle populations.[101, 121]

This study has demonstrated methodology for using quantitative film balance studies and a simple analysis-formalism to assess the extent to which 2D populations of CdSe nanoparticles deviate from ideal hard-disk behavior. This work establishes a foundation for future work on both directed assembly strategies for nanoparticle building blocks and on the controlled deposition of precisely structured LB films. In particular, it will be intriguing to continue these Langmuir studies with high resolution imaging studies of supported films to determine the extent to which the microscopic structure is consistent with the potential indicated by the isothermal studies. Studies addressing this issue are currently underway.

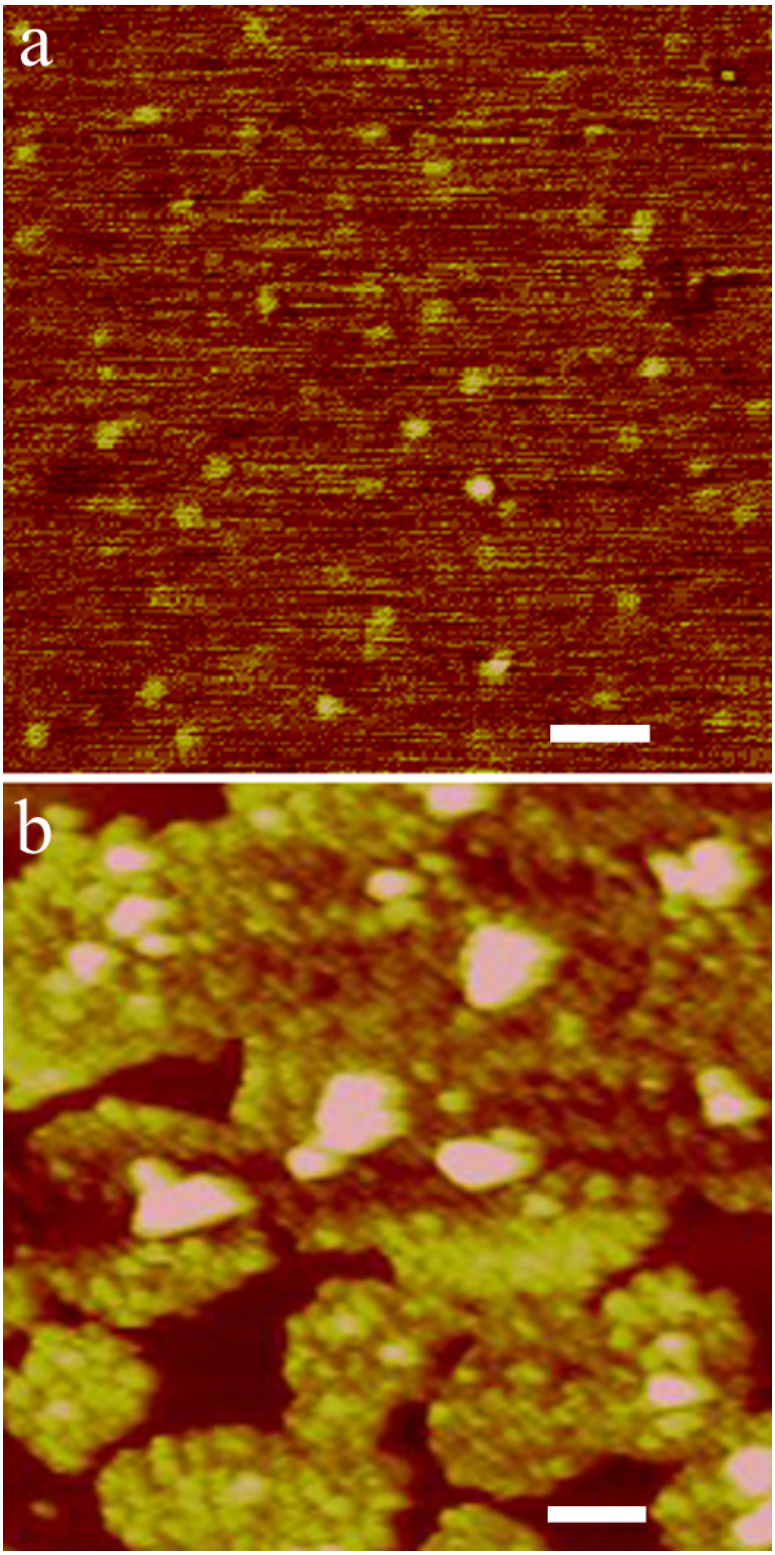

Figure II.6. Topographical images (500 nm × 500 nm) of Langmuir-Blodgett films of 2.91 nm nanoparticle populations deposited on mica at surface pressures of (a) 300 mN/m and (b) 5.0 mN/m. The scale bars denote 50 nm.

II.4 Acknowledgement

The work presented here was supported by start-up funds from Oklahoma State University and by grants from the National Science Foundation (NER 0304413), Oklahoma EPSCoR (EPS-132354), and the Center for Energy Research at OSU.

Chapter III: The Directed-Assembly of CdS Interconnects between Targeted Points in a Circuit

Reprinted with permission from B. Ozturk, I. Talukdar, and B. N. Flanders,

Applied Physics Letters, 86 (18), 183105, 2005.

CHAPTER III

THE DIRECTED-ASSEMBLY OF CDS INTERCONNECTS BETWEEN TARGETED POINTS IN A CIRCUIT

Abstract

We demonstrate the one-step dielectrophoretic assembly and interfacing of individual interconnects from populations of 3.7 nm CdS nanoparticles between targeted points in a circuit. We further show that the nanoparticles fuse into bulk CdS during the fabrication process. This finding is significant because it establishes a critical step towards the fabrication of structurally continuous semiconducting interconnects from nanoscopic building blocks.

III.1 Introduction

The controlled assembly of nanoscopic building blocks into electronic devices has the potential to revolutionize integrated circuitry. Lithographic approaches to integrated circuit production are diffraction-limited in the minimum feature sizes (~100 nm) they can produce. Assembling nanoparticles into targeted structures has yielded devices with feature sizes as small as the nanoparticle-size (~5 nm), as evidenced by the fabrication of field effect transistors from single-walled carbon nanotubes.[85, 86] It is even possible to

produce sophisticated circuitry from such devices, as evidenced by recent demonstrations of on-chip, digital logic operations.[89, 122] While these results are impressive, the low-yield production of these devices presents a serious obstacle to their use in electronic applications. Hence, Lieber and co-workers employed electric fields to interface dielectrophoretically individual InP nanowires with diametrically opposed electrodes,[94] as others have done in the trapping of single metallic nanoparticles.[123, 124] These efforts demonstrate the targeted placement of nanoscopic components by macroscopic fields, an important assembly-strategy that circumvents the piecewise manipulation of the building blocks. However, in all of these studies, dielectrophoresis[76] was used only to integrate pre-fabricated components with existing electronics.

Remarkably, Velev and co-workers have shown that dielectrophoresis may be used to assemble microscopic wires composed of metallic nanoparticles and to interface them with macroscopic electrodes, all in one step.[93] In a similar manner, Tinkham and co-workers have assembled *nanoscopic* wires from nanoparticle-populations,[125] demonstrating the dielectrophoretic production of interconnects with feature-sizes comparable to the building blocks. However, due to the essential role of semiconductors in electronic devices, the fabrication of *semiconducting interconnects* remains an outstanding issue in the dielectrophoretic production of electronic devices. In the present study, we report on the fabrication of *individual* microwires composed of *CdS* nanoparticles between *targeted points* in a circuit. In combination with recently established methods for doping II-VI nanoparticles,[126, 127] this work constitutes a critical

step towards the dielectrophoretic assembly of nanoscopic, on-chip field-effect transistors.

III.2 Experimental

III.2.1 CdS nanoparticle Synthesis

We employed an established approach to synthesizing the CdS nanoparticles.[128] 10 mmol of $Cd(CH_3COO)_2 \cdot 2H_2O$ (98%, Aldrich) were dissolved in 10 mL of deionized water. We then prepared a second solution composed of 10mmol of $CS(NH_2)_2$ (99%, Aldrich) in 10 mL of 2-methoxyethanol (99%, Alfa Aesar) and mixed the two solutions at room temperature. After increasing the temperature to 40°C to promote reduction of the Cd^{2+} moieties, the solution was stirred for ~5 hours. A color change from clear to yellow correlated with the presence of CdS nanoparticles, most likely stabilized by the amine groups. Passing this mixture through a 1 μm filter (Millipore) provided the stock solution for this study.

III.2.2 Size Analysis

Figure III.1 depicts a 100,000× transmission electron microscope (TEM) image of these CdS nanoparticles. This image was obtained by sonnicating the stock solution for 30 minutes, dispersing a 3 μL aliquot onto a grid, and imaging the dried dispersion with a TEM (JEOL JEM 100 CX II). The mean particle diameter obtained by histogramming the particle sizes in a series of such images is 3.7 nm $\pm$ 0.7 nm. This diameter falls in the

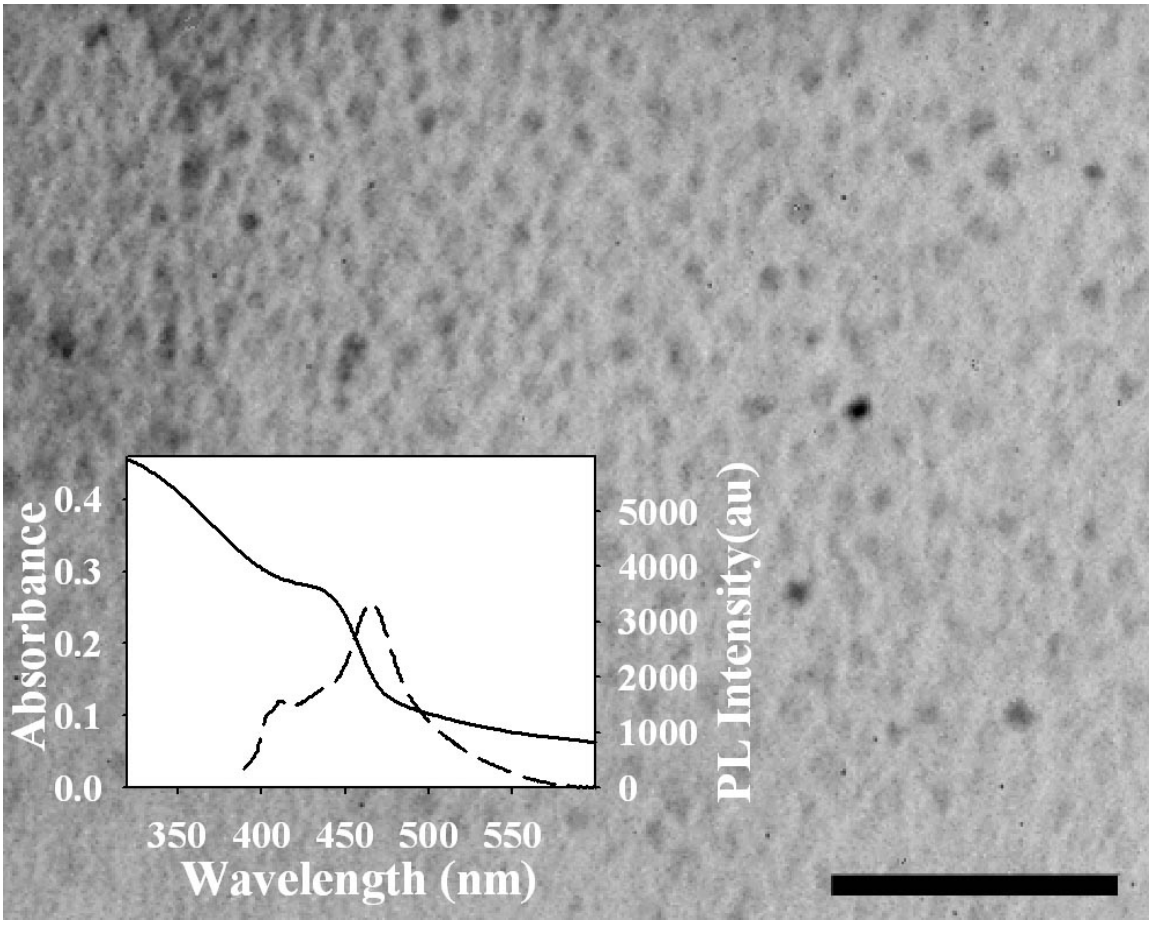

Figure III.1. 100 000× TEM image of 3.7 nm CdS nano-particles where the scale bar is 50 nm. The inset depicts the absorbance (solid line) and photoluminescence (dashed line) spectra of the stock solution.

size-confinement regime for CdS, as illustrated by the absorbance and photoluminescence spectra of the stock solution, shown in the inset. The absorbance spectrum (solid line) exhibits a peak at 440 nm due to the first excitonic transition of the size-confined particles. The photoluminescence spectrum (dashed line) is peaked at 465 nm, which corresponds to an emission-energy of 2.67 eV. The Brus Equation relates the energy of excitonic emission to the particle size.[129] Employing the measured emission-energy and the quantities for CdS used in Brus's seminal work,[129] we extracted a mean particle diameter of 3.66 nm, consistent with the TEM result.

III.2.3 Interconnect Fabrication Setup

Figure III.2a illustrates the dielectrophoretic cell-design that enables targeted interconnect-placement. Fabrication details are provided in the caption to Figure III.2. After diluting the stock solution by 10^4, a 20 μL drop is deposited across the gap between the protruded electrodes. Charged species in the stock solution give rise to deleterious electrophoretic effects, such as migration and deposition of the charged species; however, rapidly oscillating the applied field, at a frequency of 100-400 kHz, prevents the net motion of these species, effectively suppressing these effects. Instead, the geometry of these protrusions gives rise to electric field gradients in the inter-electrode region upon application of a voltage. The sense of the gradient defines the sense of the dielectrophoretic force on the particles, and, provided that the dielectrophoretic trapping force can overcome Brownian motion, particle-field interactions draw the particles to the field maximum near the floating (*i.e.* ungrounded) electrode. The polarizable particles

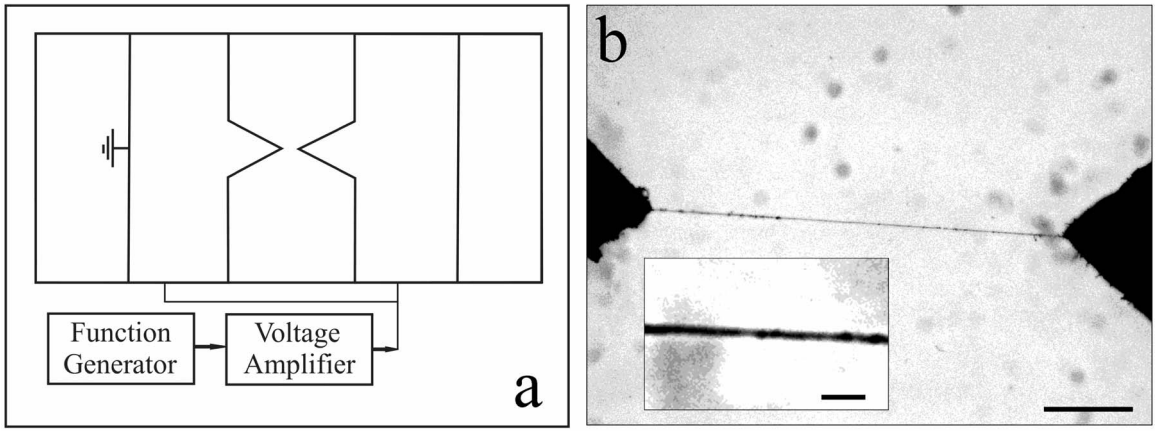

Figure III.2. (a) Cell design that enables the *targeted placement* of the interconnects. These cells were made by adhering electrode pairs that were hand-cut from copper tape onto a microscope slide. The 100–400 kHz sinusoidal output from the function generator (Hewlett Packard, HP 8111A) was passed through the voltage amplifier (FLC Electronics, F10A), the leads of which were soldered to the electrodes; (b) CdS interconnect that was dielectrophoretically assembled from the CdS nanoparticles. The scale bar denotes 200 mm. The inset depicts a magnified view of this interconnect, and the scale bar denotes 2.5 mm. The imaging system is described elsewhere.[2]

grow strongly dipolar under the field, and the close proximity of neighboring particles induces spontaneous chaining of particles along the inter-electrode line of electric field maxima.[130, 131] This behavior, which is analogous with ferro-fluidic chaining,[132, 133] results in interconnect formation and interfacing with the opposing electrodes. Figure III.2b depicts a 1.51 mm CdS interconnect that was grown in this manner; the inset indicates an interconnect diameter of ~500 nm.

III.3 Results and Discussion

Underlying interconnect growth are the abilities of the particle-field and particle-particle interactions to overcome Brownian motion, enabling the trapping and chaining of the particles. The large fields in the inter-electrode region induce large dipole moments on the particles. Hence, the strength of the *particle-field interaction* relative to ambient energy k_BT may be characterized by the unitless trapping parameter $\eta = \mu E/(k_BT)$.[133] Here, μ is the magnitude of the induced dipole moment defined as $\mu = \alpha E$, α is the excess polarizability of the particle (defined below), and E is the applied field magnitude. Similarly, the strength of dipolar interparticle attraction relative to thermal effects may be characterized by the unitless chaining parameter $\lambda = \mu^2/(4\pi\varepsilon_s\varepsilon_o(2a)^3 k_BT)$,[132] where a is the particle radius, ε_s is the dielectric constant of the solvent, and ε_o is the permittivity of free space. A particle with dielectric constant ε_p that is suspended in the solvent is characterized by an excess polarizability of $\alpha = 4\pi\varepsilon_s\varepsilon_o a^3(\varepsilon_p - \varepsilon_s)/(\varepsilon_p + 2\varepsilon_s)$.[134] To gain insight into the interactions that enable the growth of these interconnects, we estimate η and λ. Typically, a root-mean square (RMS) voltage of 110 V is applied across a ~1 mm

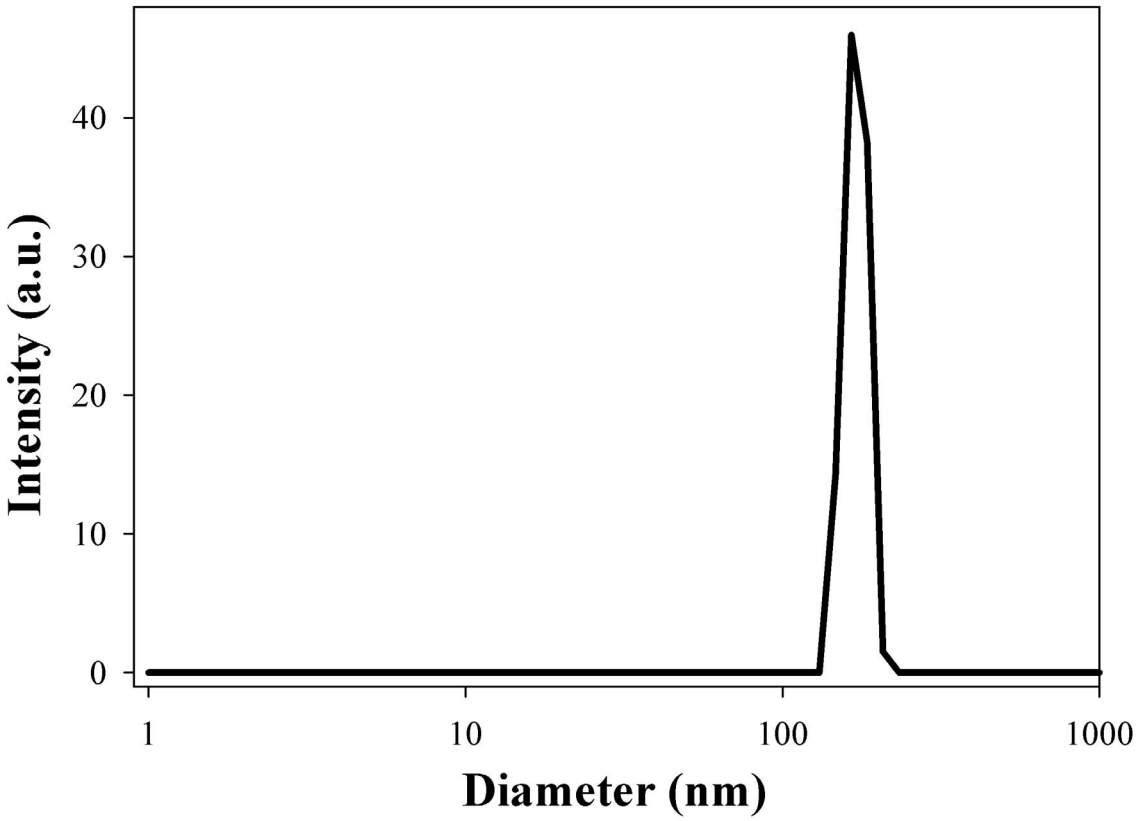

Figure III.3. Diameter distribution of bodies suspended in the stock solution.

gap to induce interconnect formation, indicating 110 kV/m as an approximate value for the field exerted upon a particle positioned one radius from the protrusion-apex. Using T = 290K, a = 1.85nm, ε_p = 5.7, and ε_s = 80 for the aqueous solvent,[135] we find that $\eta \sim 1\times10^{-4}$ and $\lambda \sim 1\times10^{-6}$, both much less than unity. This analysis argues against the direct trapping and chaining of the nanoparticles. Rather, an intermediate step must enable the process.

Figure III.3 depicts the size distribution of bodies suspended in the stock solution, obtained via dynamic light scattering-based particle sizing (performed on a Malvern, HPP5001). These sizes range from 170 nm to 210 nm in diameter. In combination with the photoluminescence spectrum in Figure III.1, which confirms the presence of 3.7 nm nanoparticles in the stock solution, this distribution indicates that the nanoparticles form aggregates with diameters of 170-210 nm while retaining their nanoparticulate identity. Due to their large polarizability, 205 nm aggregates give rise to trapping and chaining parameters of $\eta \sim 10$, $\lambda \sim 1$, demonstrating that interconnect growth is feasible with these aggregates. Interestingly, the ~205 nm diameter of the aggregates is comparable to the ~500 nm diameter of the interconnects, suggesting that the feature size may be controlled via the aggregate-size.

While assembling interconnects from nanoparticles is an attractive route to reduced feature sizes,[125] ultimately, these structures are to be used for charge conduction. The resistive interparticle junctions associated with particulate matter obstruct this

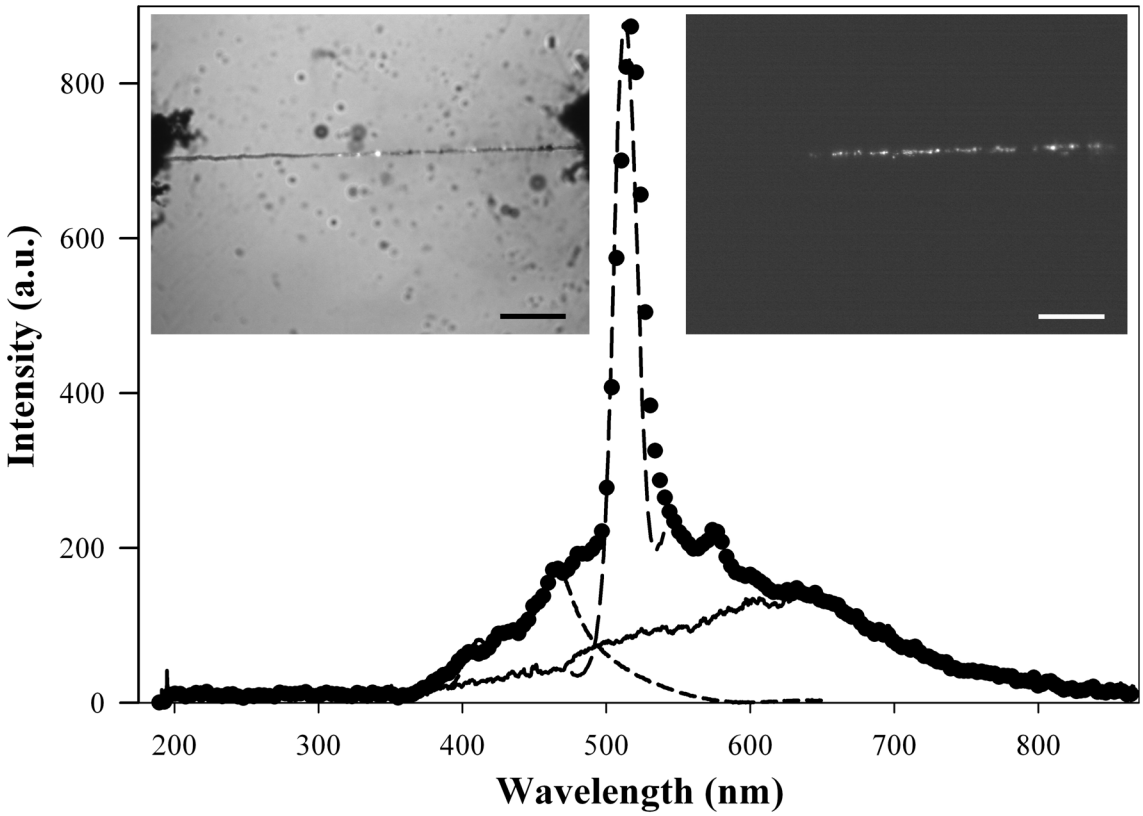

Figure III.4. The left inset depicts a bright field image of a CdS interconnect, and the right inset depicts an illumination-free image of the same interconnect. The scale bars denote 200 μm. The main figure depicts the electroluminescence spectrum of this interconnect (filled circles). Also shown are the arbitrarily scaled photoluminescence spectra of bulk CdS (long dashed line) and the stock solution (short dashed line), as well as the background electroluminescence spectrum (solid line). The interconnect spectrum was captured by using an inverted microscope, equipped with 1.25 NA 63× oil-immersion objective, to collect the luminescence, then fiber coupling the output into a monochromator (Ocean Optics, S2000) that was set to signal average for 1 s.

process, so it would be a distinct advantage to assemble structurally continuous interconnects from the nanoscopic building blocks. The left inset of Figure III.4 displays a bright field micrograph of a CdS interconnect, and the right inset shows an *illumination-free* micrograph of the same interconnect under a RMS voltage of 10.7 V.The horizontal chain of bright features in this image denotes electroluminescence along the length of the interconnect. A real-time movie of a luminescing CdS interconnect has been provided as supplementary material. Figure III.4 illustrates the corresponding electroluminescence spectrum (filled circles), which will be referred to as the interconnect-spectrum. Its dominant feature is peaked at 516.7 nm and overlaps closely with the photoluminescence spectrum of bulk CdS (long-dashed line), demonstrating the presence of bulk CdS in the interconnect. This is an interesting result because only weak intensity at 516.7 nm is evident in the photoluminescence spectrum of the stock solution (short dashed line), indicating a negligible amount of bulk CdS in the starting material. *These results imply that nanoparticulate CdS converts to bulk CdS during interconnect fabrication.* This conversion is incomplete, as the blue edge of the interconnect-spectrum overlaps closely with the photoluminescence spectrum of the stock solution, revealing the residual presence of nanoparticles in the interconnect. Furthermore, the close overlap between the red shoulder of the interconnect spectrum and the spectrum captured after electrolytic destruction of the interconnect indicates that this shoulder is largely due to background electroluminescence from the surrounding solution. In sum, the spontaneous structural conversion that these findings establish reveals the possibility of controlling the structural nature of interconnects assembled from nanoparticulate building blocks.

This study has demonstrated methodology for the one-step assembly and interfacing of individual semiconducting interconnects from nanoparticle solutions. We are currently seeking to control the feature size and structural continuity of the interconnects through variation of the aggregate-diameter and the nanoparticle capping layer, respectively. In pursuing these studies, we anticipate developing methodology for fabricating interconnects of arbitrary composition, well controlled structure, and feature-size significantly less than is attainable via conventional microfabrication methods.

III.4 Acknowledgements

This work was supported by Oklahoma State University and by grants from the National Science Foundation (NER 0304413), Oklahoma EPSCoR (EPS-132354), and the Center for Energy Research at OSU. We thank Professor Eduardo Yukihara for use of the Spex FluoroLog-3 spectrofluorometer and the Ocean Optics monochromator employed in these studies.

Chapter IV: Reproducible Interconnects Assembled from Gold Nanorods

Reprinted with permission from B. Ozturk, C. Blackledge, D. R. Grischkowsky, and B. N. Flanders, *Applied Physics Letters*, 88, 073108, 2006.

CHAPTER IV

REPRODUCIBLE INTERCONNECTS ASSEMBLED FROM GOLD NANORODS

Abstract

By using cleanroom-based lithographic procedures to produce identical electrode-arrays, we have fabricated dielectrophoretic nanowires that vary in their conductance by ±10%. Transmission electron microscopy established the presence of interconnect segments composed of densely aggregated nanoparticles and of individual nanorods lying in the current-carrying path. The current-voltage profiles of these interconnects exhibited barriers to charge transport at temperatures less than ~225 K; furthermore, their conductances increased exponentially with temperature with an activation energy comparable to the nanorod charging energy. These results indicate that the Coulomb blockade associated with individual nanorods in the interconnects is the primary conductance-limiting feature.

IV. Introduction

Dielectrophoretic assembly has emerged as a promising approach to in-parallel device fabrication that exploits the spontaneous behavior of building block populations. In dielectrophoretic assembly, the dipolar term of the interparticle potential of a colloidal dispersion is amplified, leading to the single-step assembly and interfacing of electrical

interconnects with surrounding circuitry.[76, 93] Several groups have used this approach to integrate nanowires, nanoparticles, and interconnects with existing electronics.[93, 125, 136, 137] Because of the lack of reproducibility in the fabrication conditions of individually fabricated samples, there have been relatively few detailed investigations of the charge-transport properties of dielectrophoretic interconnects.[125]

IV.2 Experimental

IV.2.1 *Lithographic electrodes*

Here, we have employed standard photolithography to fabricate sets of identical electrode-pairs on 500 μm-thick quartz substrates, eliminating much of the non-uniformity that hampers wire-by-wire assembly and enabling the simultaneous fabrication of up to six interconnects under identical growth conditions (electrode-geometry, voltage amplitude and frequency, and concentration of nanoparticle solution). Figure IV.1a depicts the simple circuit that facilitates the targeted placement of reproducible interconnects. An optical micrograph depicts the three electrode-pairs, between which three simultaneously grown interconnects span the 100 μm gaps. The initial metal layer on these substrates was 100 nm of Ti onto which 500 nm of Al was deposited.

IV.2.2 *Synthesis and size analysis of gold nanorods*

We have previously demonstrated the dielectrophoretic assembly of interconnects composed of 3.7 nm diameter CdS nanoparticles.[138] However, this work[138] stopped short

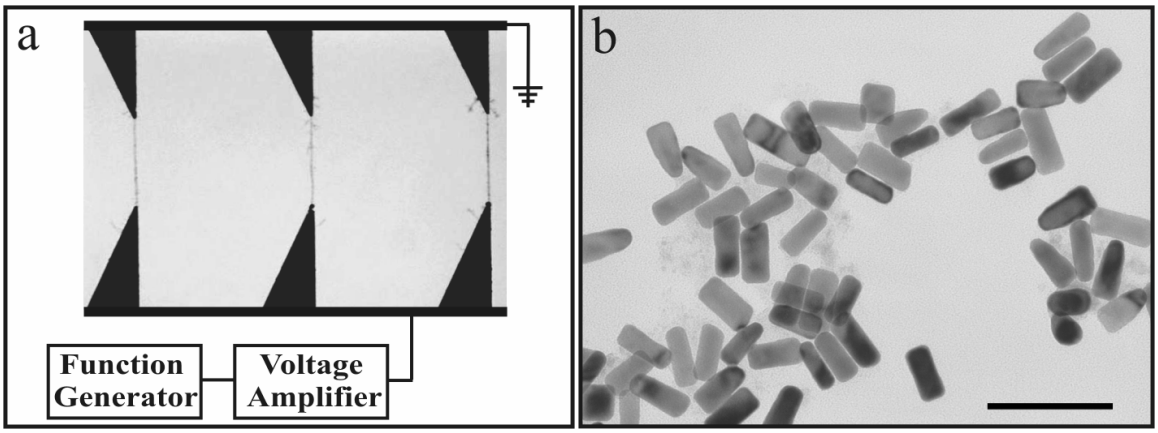

Figure IV.1.(a) The electrode array consists of 120 μm wide conducting lines (resistance 1.35 Ω/mm) that extend from macroscopic contact pads (not shown) to the electrodes. The conducting lines taper across a length of 250 μm to 2 μm diameter tips. The 100–400 kHz sinusoidal output from the function generator (Hewlett Packard, HP8111A) was passed through the voltage amplifier (FLC Electronics, F10A) connected to the three electrode-pairs. (b) A transmission electron micrograph of 30 nm long and 11 nm wide Au nanorods. The scale bar represents 100 nm.

of revealing the structural and transport properties of these interconnects because the small size of the CdS nanoparticles inhibited resolution of the mesoscopic (*i.e.* particle-level) structure of the interconnect. To gain this knowledge, the present study employs ~30 nm gold nanorods as the building blocks, easily visible with a transmission electron microscope (TEM) of moderate resolving power. We employed an established wet chemical approach to synthesize the gold nanorods.[139, 140] The resulting stock solution of nanorods contained large excesses of cetyl trimethylammonium cations and bromide anions that prevented dielectrophoretic fabrication. Hence, we centrifuged the suspensions (at 15 krpm for 20 min) to separate the nanorods from the salt solution. After re-suspending the nanorods in water, this process was repeated three additional times. Figure IV.1b depicts a transmission electron micrograph of these Au nanorods, obtained by dispersing a 7 μL aliquot of the aqueous nanorod solution onto a grid and imaging the dried dispersion with the microscope (JEOL JEM 100 CX II). Analysis of 5 such images yielded a mean rod diameter of 10.8 nm and length of 31.2 nm.

IV.3 Results and Discussion

After diluting the nanorod suspension by 10^4, a 60 μL drop is deposited across the electrode-gap. The geometry of the electrodes gives rise to strong electric field gradients upon application of a ±30 V alternating voltage. The field gradient determines the dielectrophoretic trapping force that draws the particles to the field maximum near the floating electrode. The polarizable particles become strongly dipolar under the field, inducing spontaneous chaining of neighboring particles along the inter-electrode line.[76]

The lower inset of Figure IV.2 depicts a typical interconnect of ~140 nm diameter and 60 μm length.

The upper inset to Figure IV.2 depicts DC current-voltage (*I*-*V*) profiles of 15 different 60 μm-long interconnects that were assembled three-at-a-time between lithographic electrodes. Fourteen of the interconnects show linear response with measured resistances between 20 kΩ and 48 kΩ. Twelve of the interconnects have measured resistances between 27 kΩ and 41 kΩ. The dashed black line denotes the *I*-*V* profile of the nanorod solution in the absence of an interconnect. The average of the resistances obtained from these 60 μm-long interconnects was 34 kΩ ± 3 kΩ, where the uncertainty is the standard error. The electrical properties of the interconnects are remarkably reproducible. By performing similar analyses on 15 samples each of 100 μm-long, 220µm-long, and 500µm-long interconnects, we obtained length-dependent resistances of 113 kΩ ± 7 kΩ, 165 kΩ ± 8 kΩ, and 450 kΩ ± 50 kΩ, respectively. Figure IV.2 shows that the resistance increases linearly, indicating lengthwise structural uniformity. Additionally, the linear fitting function passes through the origin, indicating that the electrode-interconnect contact-resistance is negligible.

Figure IV.3 depicts transmission electron micrographs of an interconnect dielectrophoretically assembled from the 30 nm-long nanorods. These images were collected after transfer of the interconnect from the electrode-array to a nickel grid for high resolution imaging. The inset depicts a ~10 μm segment of the interconnect, while Figure IV.3 shows a more highly magnified view of the right-central portion of this

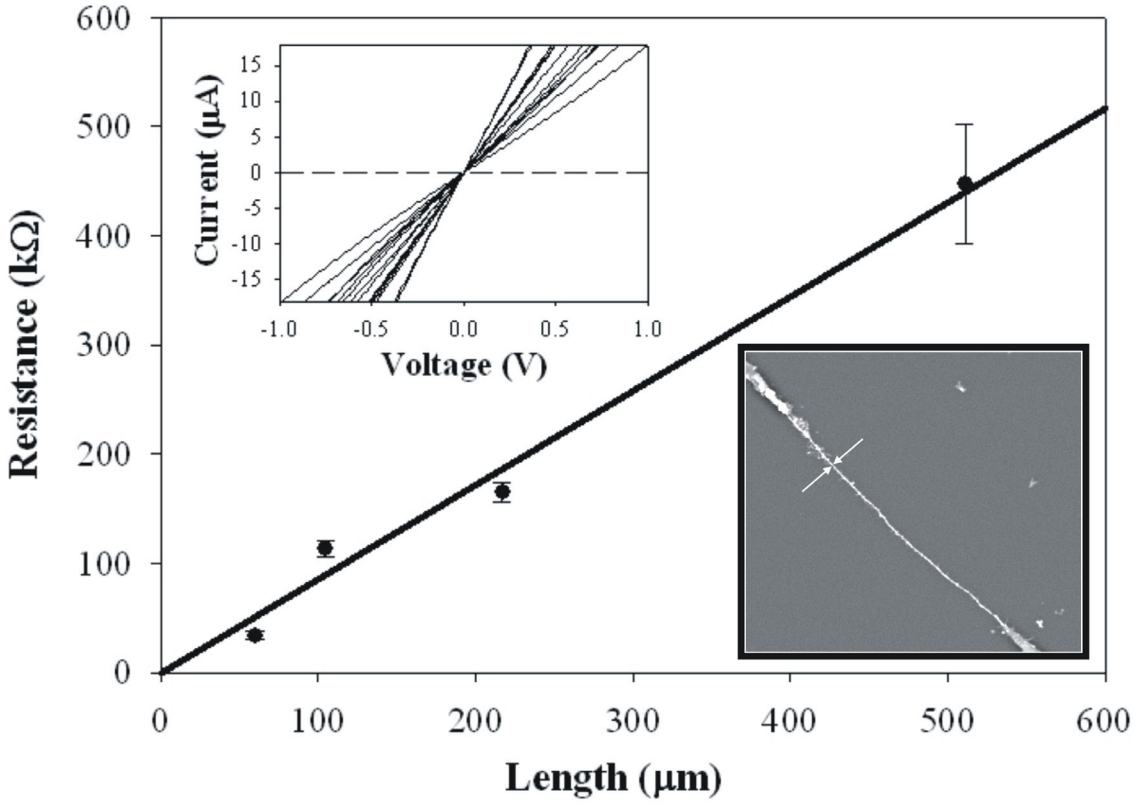

Figure IV.2. Interconnect resistance vs. length, measured at 300 K. The upper inset depicts *I-V* profiles of 15 different 60 μm long interconnects. The lower inset depicts a scanning electron micrograph of a gold nanorod interconnect.

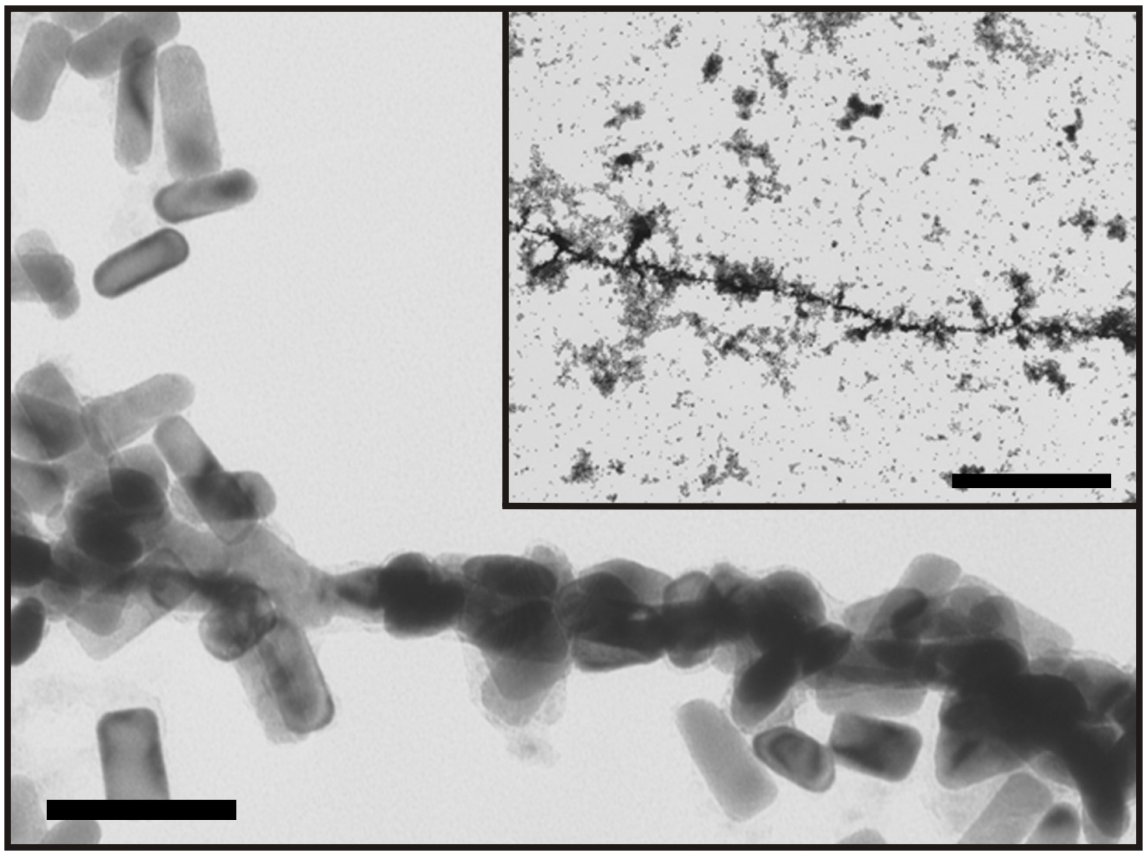

Figure IV.3. Transmission electron micrographs of an interconnect dielectrophoretically assembled from the Au rods. The main panel shows an enlarged view of the right-central portion of this interconnect (50 nm scale bar). The inset depicts a 10 μm segment of a typical interconnect (2 μm scale bar).

segment. The interconnect is 2-4 particles wide at most points along its length with substantial contact between the particles. The absence of gaps between the particles suggests that the assembly-process induces the electro-migration of gold to the regions between particles, effectively welding them into continuous segments significantly larger than the nanorods; however, high resolution TEM imaging is required to substantiate this interpretation. Moreover, individual nanorods that are not tightly integrated with their neighbors are also apparent. For example, at one point along this interconnect segment, its diameter narrows to a single nanorod. In order for current to flow, charge must move onto this nanorod. Of course, the process of transferring the interconnect to the TEM grid may disrupt the structure of the nascent wire. Nevertheless, it is reasonable that individual, unfused nanorods lie in the current-conduction path. Due to the small capacitance C of such nanorods, there is a substantial charging energy $E_c = e^2/2C$ that must be overcome in order for an electron of charge e to occupy the neutral particle.[141, 142] This barrier, known as the Coulomb blockade, is estimated as follows. We approximate the nanorod capacitance by the self-capacitance of a cylinder,[143] $C = 2\pi\varepsilon\varepsilon_o l/\ln(l/r)$, where $\varepsilon_o = 8.854 \times 10^{-12}$ C^2/Nm^2, the nanorod radius $r = 5.4$ *nm*, the nanorod length $l = 31.2$ *nm*, and we approximate the dielectric constant of the stabilizing layer as $\varepsilon = 2.7$.[144] Hence, these single particle junctions present a *30 meV* Coulomb blockade to charge transport.

To probe the extent to which the Coulomb blockade dictates the transport properties of these interconnects, we have measured and performed detailed analyses of the temperature dependent current-voltage profiles of three interconnects. Those of a

representative 500 μm-long interconnect are shown in Figure IV.4a for temperatures between 50 K and 300 K; while ohmic at room temperature, a voltage threshold V_t to charge transport becomes apparent below 225 K (dashed line) and increases in magnitude as the temperature is further reduced. This transition to nonlinear current-voltage profiles at reduced temperatures is expected when the conductance is Coulomb blockade-limited; we have observed such transitions in 12 different wires. The V_t of the low temperature *I-V* profiles shown in Figure IV.4a were determined by locating the intersection between the line describing the ohmic portion of each profile above 0.035 μA and the voltage axis. The inset to Figure IV.4a depicts the linear V_t versus *T* data, from which $V_t(T=0) = 3.83$ *V* was determined. In the absence of any thermal assistance, the applied bias must exceed $V_t(0)$ in order for current to flow through this interconnect.

Converting the *I-V* profiles shown in Figure IV.4a to conductance (*G*)-voltage profiles, where $G = I/V$, shows that the profiles vary more weakly with voltage as the temperature increases and that the conductance increases strongly with temperature. These *G-V* profiles are displayed across the 0-3 V region in Figure IV.4b. To analyze this behavior, we fit the *G-V* profiles to a simple model for the conductance:[145] $G = \sigma_o(T)\exp[(eV)/(N_b k_B T)]$, where *V* is the voltage applied across the interconnect, N_b is the number of barriers along the length of the interconnect, $k_B T$ is the thermal energy, and $\sigma_o(T)$ is the conductance at 0 V. If electrons were to experience significant barriers to charge transport between all nanorods along the entire length of this interconnect, N_b would approximate *500,000 nm/31.2 nm ~ 16,000*. We determined N_b though a global

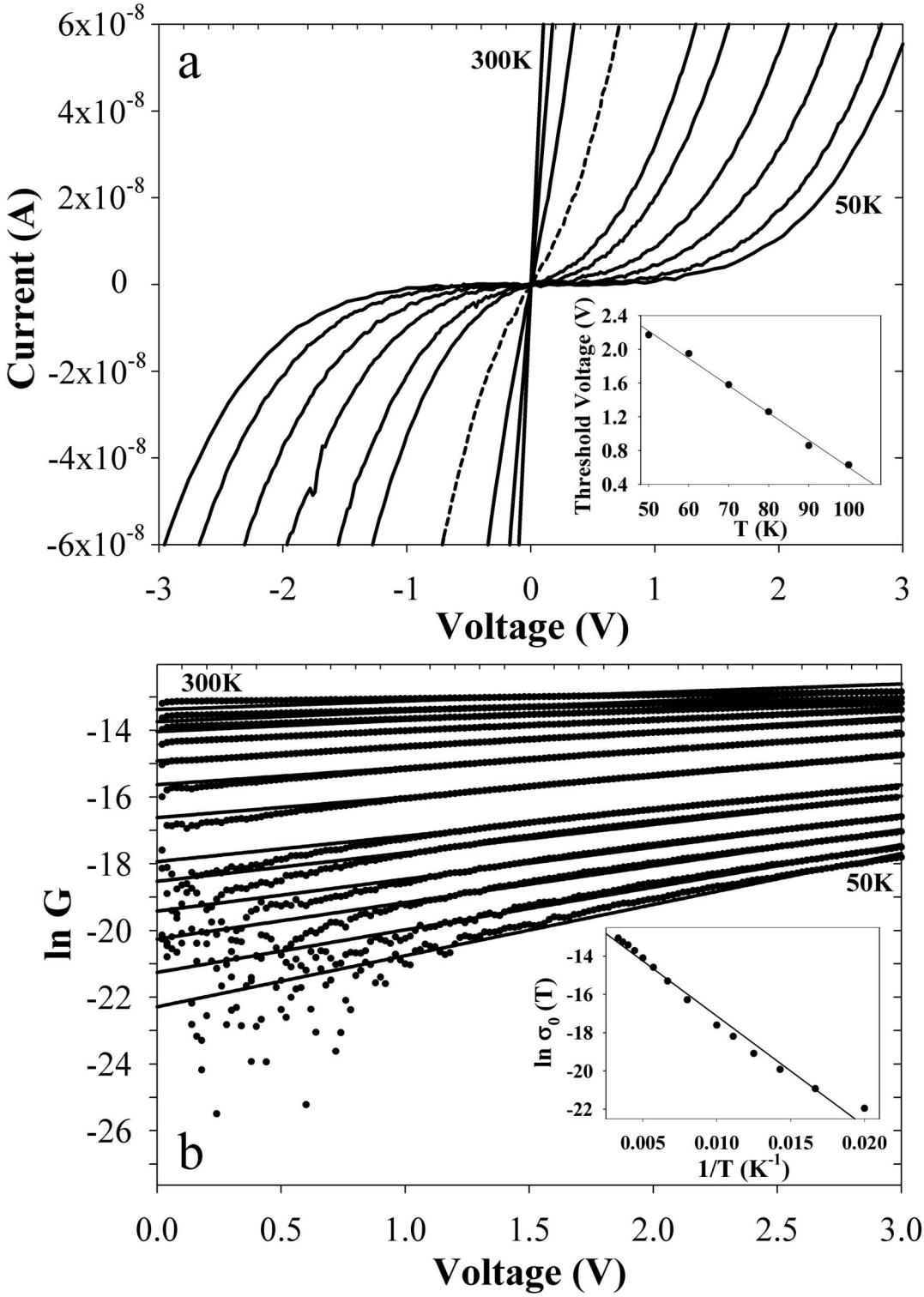

Figure IV.4. (a) The *I-V* profiles of a 500 μm long interconnect for a series of temperatures. The dashed line denotes 225 K. The inset shows the voltage threshold vs. temperature. (b) The conductance-voltage profiles for temperatures between 50 K and 300 K. The inset depicts the temperature dependence of the conductance at 0 V.

fitting procedure in which a single value for N_b was chosen that best satisfied the voltage dependence of all 15 conductance profiles, and treated $\sigma_o(T)$ as the only adjustable parameter. Figure IV.4b shows that qualitative agreement between the model and the measured profiles of the 500 μm wire was attained for $N_b = 150 \pm 30$, two orders of magnitude smaller than the value expected for charge transport between individual, unfused nanorods. This result suggests that the nanorods undergo extensive fusing during interconnect formation. Supporting this finding, the TEM images in Figure IV.3 are consistent with interparticle fusing, and we have detected analogous behavior in interconnects composed of CdS nanoparticles.[138] Knowledge of N_b and $V_t(0)$ enables calculation of the average magnitude of an individual barrier in the 500 μm wire: $E_b = eV_t(0)/N_b \sim 26$ meV. This barrier height is in good agreement with the charging energies of a 30 nm nanorod, $E_c \sim 30$ meV, suggesting that the Coulomb blockade is the primary barrier to charge transport in these interconnects.

To confirm this interpretation, we plot the natural log of the fit-extracted values for $\sigma_o(T)$ versus T^{-1} in the inset to Figure IV.4b and find that the natural log of the conductance decreases linearly with T^{-1}. This Arrhenius behavior is expected for systems in which the primary mode of conduction is electronic tunneling onto a mesoscopic island that sits at a higher energy than the neighboring segments.[146] The 574 K slope of this plot indicates that an activation energy E_a of 50 meV is associated with transport onto these islands. This energy barrier falls within a factor of 2 of both E_c and E_b. Moreover, the analyses of the other two interconnects investigated in this study yielded values for E_a and E_b that fall within a factor of 4 of E_c. Given the approximate nature of the dielectric

constant in the E_c calculation and the uncertainty in N_b in the E_b calculation, the agreement is acceptable. Hence, this work, based on reproducible data from lithographically fabricated electrode-arrays, demonstrates the significance of the Coulomb blockade in the activated transport of dielectrophoretic interconnects. The ability to produce such wires will facilitate the development of innovative electronic devices, such as variable capacitors that require Coulomb blockade-exhibiting materials.[147]

IV.4 Acknowledgements

The work was partially supported by the National Science Foundation (NER 0304413) and Oklahoma EPSCoR (EPS-132354). Additionally, we acknowledge the lithographic mask design by Sharmila Rajendran, the fabrication of the electrode-arrays by Yuguang Zhao, and the custom-milled chip-mounts by Mike Lucas.

Chapter V: The Directed Growth of Single Crystal Indium Wires

Reprinted with permission from I. Talukdar, B. Ozturk, T. D. Mishima, and B. N. Flanders, *Applied Physics Letters*, 88, 221907, 2006.

CHAPTER V

THE DIRECTED GROWTH OF SINGLE CRYSTAL INDIUM WIRES

Abstract

Tailored electric fields were used to direct the dendritic growth of crystalline indium wires between lithographic electrodes immersed in solutions of indium acetate. Determination of the conditions that suppress side branching on these structures has enabled the fabrication of arbitrarily long needle-shaped wires with diameters as small as 370 nm. Electron diffraction studies indicate that these wires are crystalline indium, that the unbranched wire segments are single-crystal domains, and that the predominant growth-direction is near ⟨110⟩. This work constitutes a critical step towards the use of simply prepared aqueous mixtures as a convenient means of controlling the composition of submicron, crystalline wires.

V.1 Introduction

Directed wire-growth techniques enable the one-step assembly and interfacing of submicron interconnects composed of a wide variety of materials[93, 125, 138, 148] and, therefore, are promising approaches to the fabrication of high quality photonic, mechanical, and electronic devices. To realize these goals, precise control over the

structure of the wires is necessary, as their structural properties will dictate their optical, mechanical, and electronic properties in device-applications. Recent studies have revealed the potential of dielectrophoresis for attaining impressive structural control over assembled wires. In a solution-phase study, Fritzche and co-workers produced wires composed of 30 nm-diameter gold nanoparticles that were arranged in a pearl-necklace configuration;[137] this outcome demonstrates the assembly of interconnects with *mesoscopic* structural precision, where the organization of the particles composing the wire is periodic. In a separate, gas-phase study, Libbrecht and coworkers used dielectrophoretic forces to direct the growth of ice crystals;[149] this work demonstrates the growth of dendrites with *microscopic* structural precision, where the organization of the molecules composing the dendrite is periodic. Attaining such *microstructural* control in solution-phase directed assembly would provide a straight-forward means of growing high quality wires of composition determined simply by choice of solute. To this end, Haynie and coworkers have fabricated wires from simple, aqueous solutions of palladium acetate.[99] While this work stopped short of determining the stoichiometric composition or crystallinity of the wires, it demonstrated directed wire-growth in solutions containing only dissolved salt. The present work builds on these previous studies to demonstrate methodology for the electrochemical growth of single crystal indium wires from aqueous solutions of indium acetate. This work demonstrates the use of a simple salt solution as a medium in which to grow single crystal metal wires between targeted sites in a circuit.

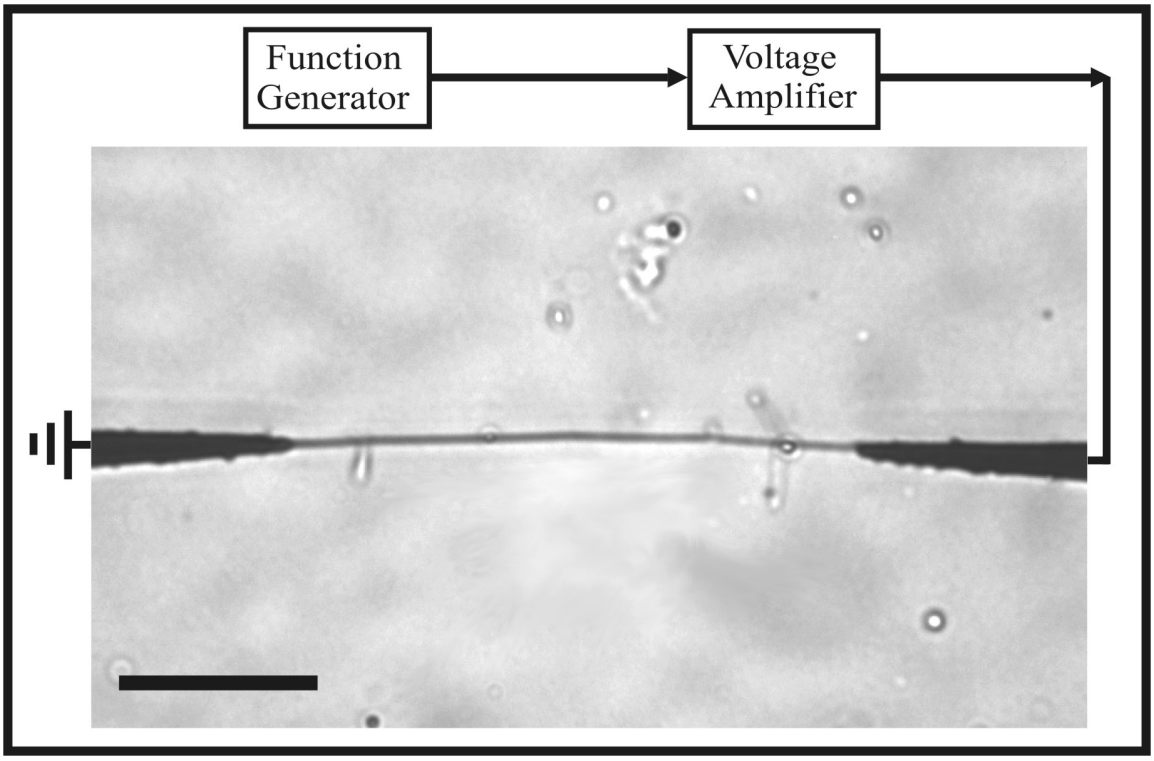

Figure V.1. Apparatus for directed electrochemical wire growth. The image is an optical micrograph of a wire grown from indium acetate solution. The scale bar denotes 20 μm.

V.2 Experimental Setup

Figure V.1 shows a diagram of the wire-growth apparatus. The function generator (Hewlett Packard, 8111A) supplies an alternating voltage that is passed through an amplifier (FLC Electronics, F10A) and applied across the lithographic electrodes. These electrodes are deposited on 1 mm-thick Pyrex substrates, using standard lithographic techniques, as described elsewhere.[150] The optical micrograph in Figure V.1 depicts the ends of a tapered electrode pair. The wire spanning the 60 μm electrode gap was grown by depositing a 10 μl drop of a 0.055 M aqueous solution of indium acetate ($In(CH_3COO)_3$) over the gap and applying a 1.0 MHz square-wave with an amplitude of 18 V and no DC offset. The wire grew from the alternating electrode to the grounded electrode immediately (to the eye) after switching on the alternating voltage. When the wire interfaced with the opposing electrode, the voltage was terminated manually. The growth-process was observed on an inverted microscope (Leica, IRB) equipped with a digital camera (Roper, CoolSnap).

V.3 Results and Discussion

For a given electrode gap and geometry, variation of the voltage amplitude, its frequency, and the $In(CH_3COO)_3$ concentration gives rise to a wide range of wire-structures. Figure V.2a depicts a concentration-voltage phase diagram of interconnect structural types, all of which were fabricated between electrodes spaced by 60 μm, with an AC frequency of 1.0 MHz. When the peak-to-peak voltage amplitude was less than

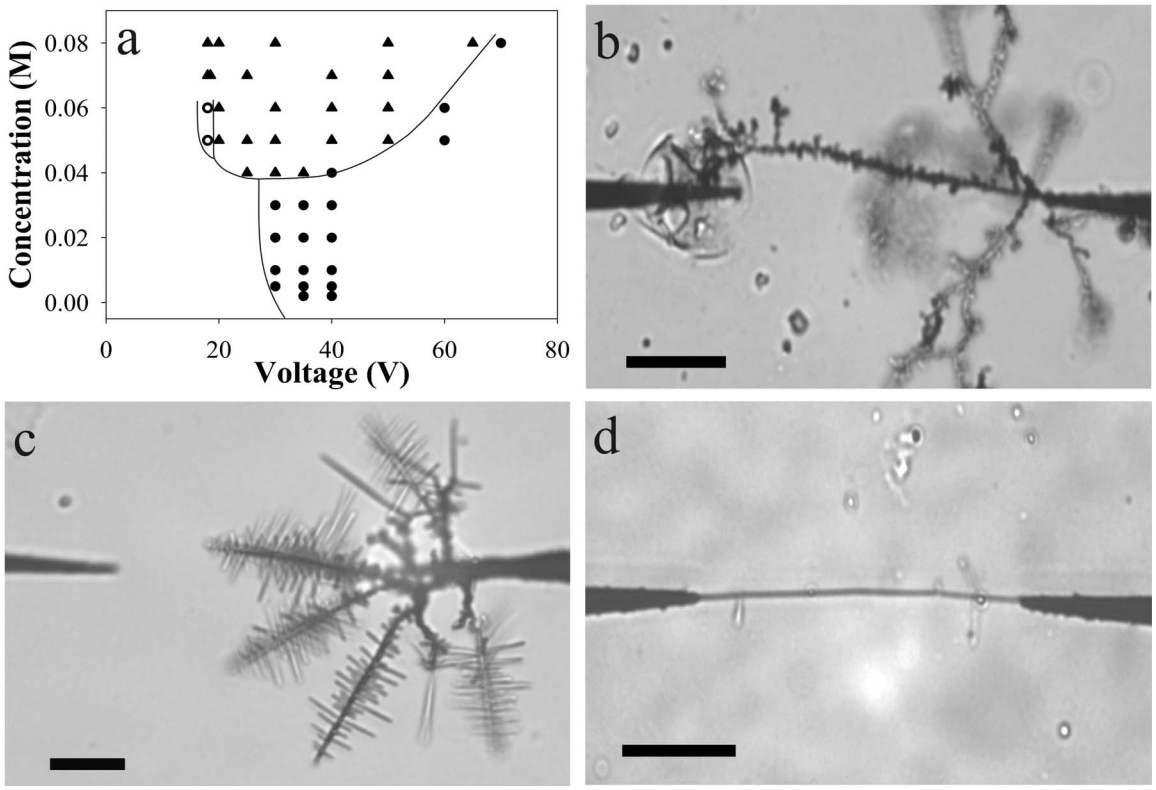

Figure V.2. (a) Concentration-voltage phase diagram of interconnect types. The conditions that give rise to amorphous, dendritic and needle-shaped wires are denoted by the filled circles, the filled triangles, and the unfilled circles, respectively. (b) A representative image of an amorphous wire. (c) A representative image of a dendritic structure. (d) A representative image of a needle-shaped wire. The scale bars in images (b)–(d) represent 20 μm.

18 V, interconnect formation did not occur, regardless of the $In(CH_3COO)_3$ concentration. For concentrations less than 0.040 M and voltages greater than 30 V, wires with an amorphous appearance spontaneously grew. The filled circles denote this region in Figure V.2a, and Figure V.2b depicts a typical amorphous wire. Increasing the $In(CH_3COO)_3$ concentration to greater than 0.040 M, caused dendritic wire-growth. The filled triangles denote this region in Figure V.2a, and Figure V.2c depicts a typical dendritic sample. Setting the voltage to 18 V and using a saturated (0.055 M) indium acetate solution gives rise to suppressed side-branching and the formation of individual, needle-shaped wires. The unfilled circles denote this small region of phase space in Figure V.2a, and Figure V.2d depicts a representative wire. The dendritic wires presented here are similar in appearance to the dendritic structures that were previously observed in $ZnSO_4$ solutions;[151, 152] however, in the present case, their growth is directed.

A 200 kV transmission electron microscope (TEM) made by JEOL (JEM-2000FX) was used to obtain detailed crystallographic information of the dendritic wires. Because the pyrex substrates of the electrode arrays are not thin enough to transmit the electron beam, it was necessary to transfer the wires to TEM grids. The transfer process consisted of using an actuator to push a holey carbon grid (Ted Pella) across the wire-laden electrode gap. To increase the probability of successful transfer, we populated the liquid in the inter-electrode region with several wire-segments, breaking each wire free of the electrode after its growth. Translating the TEM grid through this dispersion caused the wires to flow onto the grid. Figure V.3a shows a TEM micrograph of a group of

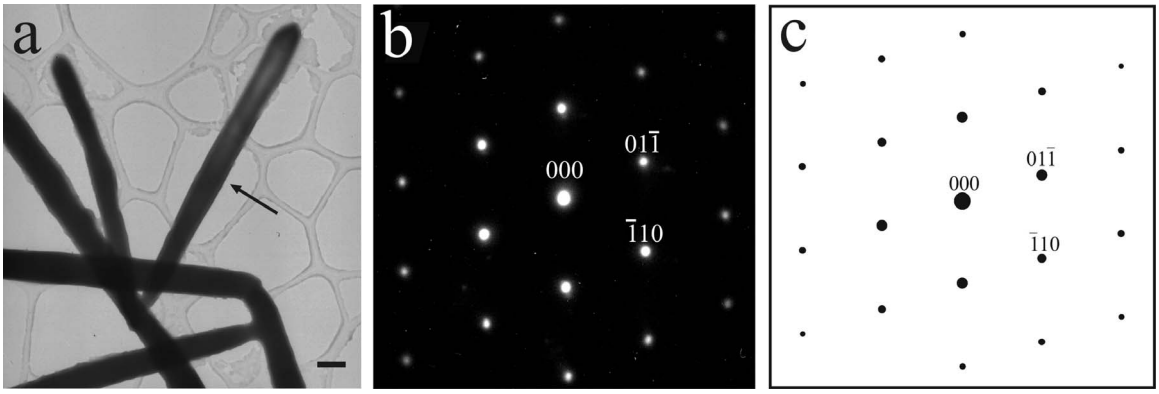

Figure V.3. (a) A group of needle-shaped wires, transferred onto a TEM grid. The scale bar denotes 500 nm. (b) The measured diffraction pattern of the wire segment indicated by the arrow in (a). (c) The simulated diffraction pattern of crystalline indium, observed from the [111] direction.

wires that were mounted in this manner. The wires are needle-shaped with sparse side-branching. The six wires depicted in this image range in diameter from 367 nm to 556 nm.

Figure V.3b depicts a selected area electron diffraction pattern collected from the wire-segment indicated by the arrow and oriented as shown in Figure V.3a. Because the area selected by the ~1 μm-diameter aperture did not include any portion of the carbon grid, no ring patterns due to amorphous carbon are evident in this figure. Figure V.3c shows a simulated $\langle 111 \rangle$ diffraction pattern that was calculated using a commercial software package (Virtual Laboratories, Desktop Microscopist), requiring as input the camera length (790.8 mm), the electron wavelength (2.51×10^{-3} nm), and the known structural parameters of crystalline indium: a tetragonal crystal structure, with $a = b = 0.3251$ *nm* and $c = 0.4945$ *nm*, belonging to symmetry group *I4/mmm*.[153] The experimental and simulated diffraction patterns are in excellent quantitative agreement with each other. For example, on the TEM film the distances of the $01\bar{1}$ and $\bar{1}10$ spots from the 000 spot are 7.33 mm and 8.57 mm, respectively; the angle subtended by these diffracted spots is 53.7º ± 0.4º. The corresponding calculated values are 7.31 mm, 8.64 mm and 53.78º. The error for each of these quantities is less than 0.85%. This close agreement indicates that the wire is composed of crystalline indium. Of 13 wires examined in this manner, all were crystalline indium.

To determine the continuity of the crystalline regions of these wires, selected area diffraction patterns were collected from successive positions along their lengths, using an

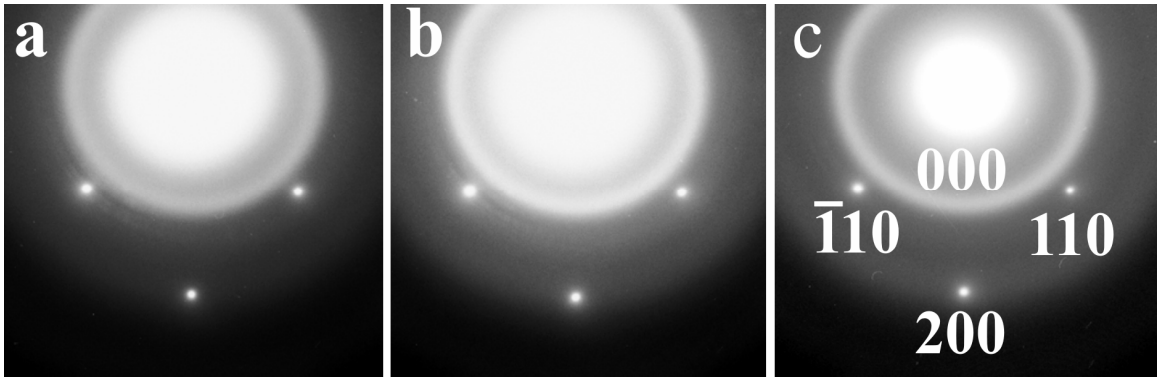

Figure V.4. The selected area diffraction patterns measured from the (a) lower third, (b) middle third, and (c) upper third of the ~5 μm long wire segment indicated by the arrow in Figure V.3 (a).

area selection aperture with a 2.2 μm diameter. Figures V.4a-c represent diffraction patterns captured from the lower, middle, and upper sections of the ~5 μm-long wire indicated in Figure V.3a. For this measurement, the sample was rotated so that the electron beam impinged upon a different face of the wire. Analyses of the discrete patterns in Figures V.4a-c indicate that all three diffraction patterns result from crystalline indium observed from the $\langle 001 \rangle$ direction, confirming the structural assignment made above. The diffuse rings in these images result from the amorphous carbon strands of the TEM grid beneath the wire-segment. Moreover, in each of the three images, the $\langle 001 \rangle$ diffraction pattern is identically oriented, the diffracted spots are located the same distances from the 000 spot, and no double (or multiple) sets of diffracted spots are visible. These observations indicate that this wire-segment is a single-crystal domain of highly pure indium. Of 13 wire-segments examined in this manner, some as long as 25 μm, the crystal structure was found to be invariant along the length of each segment, indicating that this growth-procedure produces indium wire-segments that are single crystals.

We determined the growth-direction of the wires by comparative analysis of the selected area diffraction patterns and the corresponding real-space images. Analysis shows that 8 of the 9 main segments (as opposed to side-branches) examined in this study grew nearly perpendicular to the {110} plane with up to 8^{o} of deviation. Often, the least stable surface of a crystal grows the fastest,[154] and the {110} plane is one of indium's high energy planes, with a surface energy merely 1% smaller than that of the {011} plane, the highest energy surface under ultra-high vacuum.[155] The aqueous environment

and the applied electric fields may further influence the growth-direction, so it is not surprising that the wires grow predominantly in the ⟨110⟩ direction. However, determining the origin of this preference requires further study.

We observed similar dendritic growth-behavior in saturated solutions of lead acetate and nickel sulfate. While a conclusive determination of the electrochemical mechanisms underlying this wire-growth phenomenon is beyond the scope of this work, the necessity that the solutions be saturated with salt suggests that supersaturation drives the dendritic solidification process,[156, 157] just as supercooling drives dendritic growth in pure materials.[158] We expect our ongoing investigation into the growth-mechanism to enable the directed dendritic growth of crystalline wires from a broadened range of materials.

This work establishes an innovative, electrochemical approach to growing single-crystal, metallic wires between targeted sites in on-chip circuitry, demonstrating the possibility of using simply prepared aqueous solutions to grow submicron wires composed of metals-of-choice. As the directed growth and interfacing of wires is not easily attainable with other crystal-growth techniques, such as the vapor-liquid-solid mechanism,[159, 160] this work is expected to prove useful in applications requiring the *in situ* growth of single-crystal interconnects.

V.4 Acknowledgements

This work was supported by the National Science Foundation (NER-0304413) and Oklahoma EPSCoR (EPS-132354). We thank Daniel R. Grischkowsky for generously sharing the cleanroom facilities used to produce the lithographic electrode arrays.

Chapter VI: Directed Growth of Diameter-Tunable Nanowires

CHAPTER VI

DIRECTED GROWTH OF DIAMETER-TUNABLE NANOWIRES

Abstract

This study characterizes a method for controlling the nanowire-diameter in the directed electrochemical nanowire assembly technique, where alternating voltages applied to electrodes in simple salt solutions induce the single-step growth and interconnecting of crystalline metallic wires. Dendritic solidification is identified as an important component of this technique. A characteristic of dendritic solidification is that the *growth-velocity* and tip-radius are anti-correlated. This relationship is exploited to realize diameter-tunable nanowire growth. The experimental parameter that provides this control is ω, the frequency of the alternating voltage. Increasing ω effectively steepens the metal cation concentration gradient at the wire-solution interface, thereby increasing the growth-velocity of the wire. For indium wires, increasing ω from 0.5 to 3.5 MHz increases their *growth-velocity* from 11 to 78 μm/s and reduces their diameter from 770 to 114 nm. Gold wires exhibit diameter-tunability that ranges from 150 nm down to 45 nm. Thus, it is possible to tune the wire diameter from the microscale down to the nanoscale.

VI.1 Introduction

The production of circuitry with sub-diffraction limited feature sizes is a widely pursued goal of nanotechnology, and metallic nanowire fabrication is a fundamental aspect of this goal.[47] Tied to this pursuit is the need for the directed growth and low resistance interconnecting of nanowires with precisely tunable diameters. This level of control would enable fundamental investigations of 1D transport behaviors, which emerge as the wire-diameter is reduced to the fundamental length scales of the wire-material. In particular, as the wire-diameter approaches the electronic mean free path (~31 nm for gold at room temperature[161]), an increase in resistivity due to electron-surface scattering is expected.[162, 163] Although well-established in thin metal films,[164] this effect has yet to be unambiguously characterized in metallic wires.[165-168] To countermand this resistivity-increase, it may be possible to exploit more exotic transport processes. Superconductivity is, perhaps, the most widely studied mechanism for enhanced conductivity. As the wire-diameter becomes comparable to the phase coherence length, anomalous superconducting proximity effects are observed. [169] Improved understanding of this process, as well as of Kondo and ballistic transport processes, is required in order to design viable 1D devices that can take advantage of these high-conductivity transport processes.[169, 170] A convenient means of fabricating diameter-tunable metallic nanowires would expedite the study of these effects.

A number of fabrication techniques are available that provide control over the nanowire-diameter. The vapor-liquid-solid method is one of the best established.[171] This approach uses metallic nanodroplets to catalyze the condensation, nucleation, and axial

growth of vaporous growth-material[172] to produce pristine arrays of near single crystalline nanowires from a wide variety of materials.[42, 47, 160, 172-178] The size of the catalytic nanodroplets dictates the diameter of the nanowires, which can be as small as 1 nm,[179, 180] and influences the crystallographic direction in which the wires grow.[181] In an alternative approach, porous substrates,[182] nanotubes,[183] DNA, and other biomolecules[184] are used as templates for the formation of nanowires with very small diameters and a wide range of intricate shapes. With this technique, the nanowire-diameter is determined by the pore size of the template and can extend from microns down to the sub-nanometer scale. A third technique has recently been developed wherein ultrasonic stimulation of simple salt and sugar solutions induces the growth of metallic nanobelts.[185] In this approach, the width of the nanobelts ranges from 8 nm to 20 nm and is controlled by the duration of the ultrasonic irradiation. A significant drawback to these established nanowire-syntheses is that connecting the individual wires with external instrumentation and with other submicron components is most often accomplished by secondary processing steps that follow the wire-synthesis. Hence, the *single-step* growth and interconnecting of diameter-tunable nanowires has become an important research goal.[186-189]

The recent demonstration of directed electrochemical nanowire assembly (DENA) constitutes significant progress towards this goal.[190] This work has shown that an alternating voltage can be used to induce the electrochemical deposition of ~500 nm diameter indium wires between targeted sites on alternating and grounded electrodes. The growth and interconnecting of these wires is accomplished in a single step. It was

further determined that these structures grew as near single crystals of pure indium.[190] This property is critical to the study of 1D transport effects, as electronic scattering at domain walls could complicate interpretation of the transport data. The DENA technique also enables the fabrication of electrode-nanowire-electrode assemblies with a high degree of structural integrity at the electrode-nanowire junctions. This feature gives rise to small electrode-wire contact resistances that are of the order of 10 Ω (see Chapter VII for details of this study).[191] Resistive junctions between electrodes and nanowires can obscure the 1D transport behavior, so minimization of the contact resistances is important. For these reasons, the DENA technique promises to be a useful tool for studying 1D transport.

In the DENA approach, variation of the salt concentration and the applied voltage dictates the morphology of the deposit, and a phase diagram characterizing these morphologies has been reported for DENA growth in $In(CH_3COO)_3$ solutions.[190] This work shows that under carefully controlled experimental conditions, these structures grow with both needle-shaped (*i.e.* wire-like) and dendritic morphologies. These morphologies were also observed in the DENA-based growth of Au nanowires.[191] The mechanism that is responsible for dendritic structures is known as *dendritic solidification*. Therefore, these results for In and Au wires strongly suggest that dendritic solidification is an important mechanism in the DENA growth process. As such, the DENA-based morphologies bear some resemblance to the electrically induced dendritic structures that have been observed in $CuSO_4$ and $ZnSO_4$ solutions.[151, 152] However, DENA grown structures have lengthwise-uniform diameters and are (roughly) cylindrical, whereas most

previously studied metallic dendrites are paraboloidal in shape.[99, 151, 152, 190] It is their near cylindrical geometry that renders DENA-grown structures potentially useful as electrical interconnects.

Dendritic solidification is a diffusion limited process and is well-described by the diffusion equation. This crystallization mechanism is ubiquitous in nature, underlying diffusion-limited growth processes as disparate as ice crystal formation,[149, 157, 192] alloy solidification,[193, 194] and Saffman-Taylor fingering in Hele-Shaw cells.[195-198] The theoretical cornerstone of dendritic solidification is the Ivantsov solution of the 3D diffusion equation. This analysis shows that the *growth-velocity v* of the parabolic front of the solidifying dendrite and the radius *R* of its foremost tip are anti-correlated functions of the undercooling, supersaturation, or other external condition that induces crystallization.[199-204] Experimental observation has validated the prediction that *v* and *R* are anti-correlated. However, nature has also shown that dendrites grow with *unique* values of *v* and *R* for a given undercooling, a behavior that is *not* predicted by the Ivantsov analysis.[196] It was not until the development of microscopic solvability theory during the 1980s that the critical role of surface tension and surface kinetics in the selection of unique *v* and *R* values was fully appreciated. [205-208] The *v*-*R* selection behavior is technologically interesting because it suggests a method for fabricating diameter-tunable nanowires: using dendritic solidification to grow wires would permit their diameters to be controlled by controlling their *growth-velocity*.

In this chapter we show that ω, the frequency of the alternating voltage used to induce wire-growth in the DENA technique, provides direct control over the *growth-velocity* and diameters of the nanowires. This control provides a precise means of tuning the wire-diameters from the microscale down to the nanoscale. Additionally, we propose a physical picture based on dendritic solidification that explains how this control comes about. In conjunction with the wire-growth methodology that we have previously worked out,[190, 191] this capability will enable a new approach to the investigation of diameter-dependent charge transport in nanowires, an area of intense current debate. To our best knowledge, this study constitutes the first demonstration of precise diameter-tunability in a *single-step* nanowire growth and interconnecting technique.

VI.2 Experimental

The experimental apparatus for the DENA technique is depicted in Figure VI.1a, consisting of sharp, transiently biased electrodes immersed in concentrated salt solution. This apparatus is described in detail elsewhere.[190] Briefly, the optical micrograph in this figure depicts an indium nanowire spanning the 60 µm gap between the ends of a tapered electrode pair. The electrodes were deposited in 12-pair arrays on quartz substrates using standard lithographic techniques[150] and are composed of 100 nm thick base layers of Ti and 500 nm thick top-layers of Al. The wire shown in this micrograph was grown by depositing a 10 µl aliquot of aqueous 0.055 M $In(CH_3COO)_3$ solution across the electrodes and applying an ±18 V square-wave signal to the left electrode while the right electrode was grounded. Wires may be grown from other salts, as well.[99] The Au wires

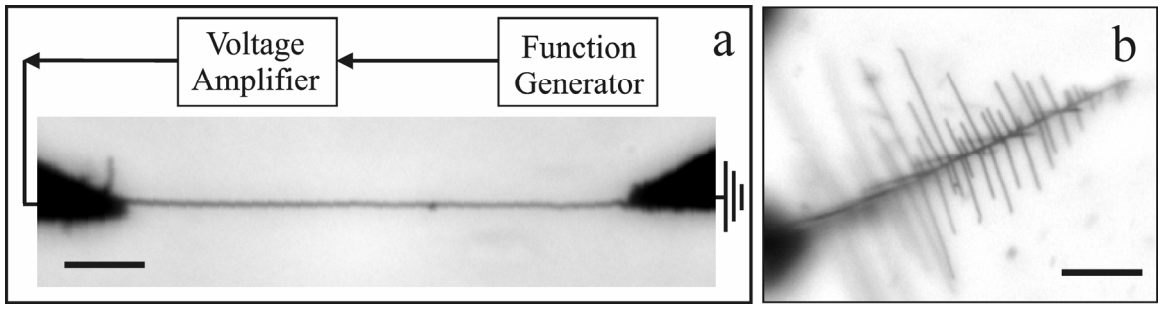

Figure VI.2. (a) Apparatus for the directed electrochemical nanowire assembly (DENA) technique. The image is an optical micrograph of a needle-shaped wire grown between lithographic electrodes immersed in aqueous $In(CH_3COO)_3$ solution. The scale bar denotes 10 μm. (b) An optical micrograph of a highly branched dendritic structure grown by the DENA technique. This phase of growth occurs when a larger voltage amplitude than used in (a) is employed to induce deposition. The scale bar denotes 10 μm.

discussed in this chapter were grown from 20 mM aqueous solutions of $HAuCl_4$. The frequency ω of the alternating voltage is the variable of interest in this study and was varied between 0.5 MHz and 3.5 MHz for In wire-growth and between 10 MHz and 50 MHz for Au wire-growth. Typically, a wire would begin to grow from the alternating to the grounded electrode within 1 s of applying the voltage. Growth occurs almost exclusively at the electrode tip. This is because the sharp tip supports an enhanced negative charge density when it is negatively biased,[209] increasing the rate at which the cations are reduced and crystallized onto this region of the electrode.

VI.3 Theory

VI.3.1 *Dendritic solidification*

Because dendritic solidification is an important mechanism in the DENA process, a brief overview of this theory is provided here to clarify how its properties enable diameter-tunable nanowire fabrication. In the DENA approach, deposition is induced by the application of an alternating voltage across an electrode pair in a salt solution. The solid deposit is composed purely of the crystallized metal species from the salt solution,[190, 191] and no other types of deposits are evident. These observations suggest that the metal cation is electro-active while the counterion is not. Assuming that deposition is diffusion limited, the evolution of *c(r, t)* the metal ion concentration in the solution at arbitrary position *r* and time *t* is described by the diffusion equation:[197]

$$\partial c(r,t)/\partial t = -\nabla \cdot \vec{j}\,. \qquad \text{(VI.1)}$$

where ***j*** is the flux of these cations. Observations of dendritic growth in succinonitrile melts and NH_4Br solutions, indicate that the solidification front of the growing dendrite is paraboloidal; hence, Equation (VI.1) is to be solved in parabolic coordinates.[156] ***j*** is defined by Fick's law as

$$\vec{j} = -\frac{Dc(r,t)}{k_B T}\nabla\mu(r,t) \qquad \text{(VI.2a)}$$

where D and $\mu(r,t)$ are the diffusion coefficient and electrochemical potential of the *metal* species, respectively, while k_BT is the thermal energy. $\mu(r,t)$ is defined as

$$\mu(r,t) = k_B T \ln c(r,t) + zq\phi(r,t) \qquad \text{(VI.2b)}$$

where zq is the charge of a *metal* cation and $\phi(r,t)$ is the electric potential in solution due to the applied voltage.

The rate at which the solidification front advances through the solution is the growth-velocity and is expressed by the mass conservation condition:[197]

$$\hat{n}\cdot j = -v(\rho_m - c_{Int}) \qquad \text{(VI.3)}$$

where $\hat{n}$ is the outward-directed surface normal. ρ_m is the number density of the solid metal deposit, and c_{Int} is the metal cation (number) concentration at the tip-solution interface (see Figure VI.2). Equation (VI.3) states that a wire growing with velocity v requires a net flux j of cations to flow to the tip from the solution. The flux j is less than

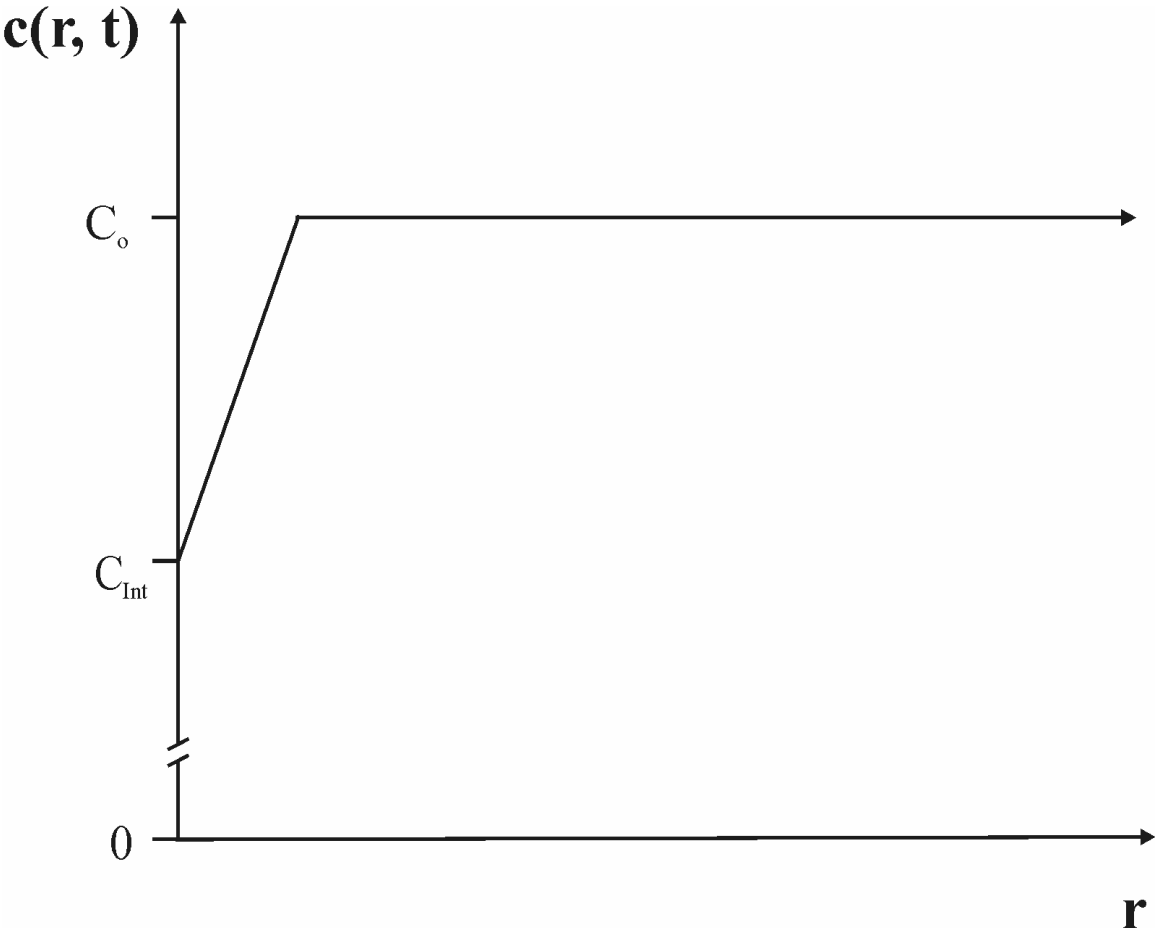

Figure VI.2. Simple concentration profile of metal ions in a supersaturated salt solution near a curved interface.

the product $v\rho_m$ by an amount vc_{Int}, which represents the effective flux that is already available at the interface due to nonzero c_{Int}.

An expression for the wire growth-velocity along the outward normal is obtained by substituting Equations (VI.2a) and (VI.2b) into Equation (VI.3), yielding

$$v = \left[\hat{n} \cdot \frac{D\nabla c(r,t)}{\rho_m - c_{Int}} \right]_{Int} . \qquad \text{(VI.4)}$$

where the simplification $\nabla\phi(r, t) = 0$ has been made and is justified in the *Discussion* section. The quantities in Equation (VI.4) are to be evaluated at the interface between the solution and the solid. Equation (VI.4) shows that the wire *growth-velocity v* depends directly on the cation concentration gradient. Therefore, an experimental means of controlling $\nabla c(r, t)$ would provide the desired control over *v*.

Ivantsov solved the stationary form of Equation (VI.1) (where $\partial c/\partial t = 0$) for a 3D parabolic solidification front without considering the Gibbs-Thompson boundary condition, attachment kinetics, or an electric potential.[199] The main result of this effort is that the growth-velocity *v* of the dendrite and the radius *R* of its foremost tip are found to be anti-correlated with each other. That is, the Ivantsov solution relates Δ, the undercooling or other external condition that induces solidification, to the Péclet number *p*:[199-204]

$$\Delta = pe^{p} E_1(p) . \qquad \text{(VI.5)}$$

Here, $p = Rv/(2D)$ and $E_1(p)$ is the exponential integral. This result indicates that for a given Δ, a unique value for p characterizes the growing dendrite. Despite the neglect of the above-stated boundary conditions, this result captures the anti-correlated relationship between v and R that is observed experimentally: for a particular Δ, a solidification front characterized by a small R grows faster than one with a large R.

Nature is actually even more selective than Equation (VI.5) implies. Observations reveal that not only is p specified by a given Δ, but individual dendrites grow with unique values of v and R, as well:[196] there is spontaneous velocity and radii-selection (not merely p-selection, which would permit a continuum of v and R values for a given p). Following extensive work by a number of groups,[197, 210] Brener solved the stationary form of Equation (VI.1) with $\phi(r, t) = 0$ for a 3D parabolic front and *with* realistic boundary conditions for anisotropic surface energy and attachment kinetics.[211] This analysis shows that the *anisotropic* surface tension of the crystalline solid leads to the selection of unique v and R values in the theory. v-selection emerges because Brener's approach determines a second relationship between v and R:

$$\sigma = \frac{2d_o D}{vR^2}. \qquad \text{(VI.6)}$$

This equation is known as the solvability criteria. σ is derived explicitly in Brener's theory, enabling specification of v. That is, the velocity depends on the Péclet number as $v = 2Dp/R$, where D is known. Δ is a (known) experimental parameter, so Equation (VI.5) determines p. Equation (VI.6) may be used to eliminate R, and after some algebra,

the equation $v = 2D/(Rp)$ uniquely determines v. Because v and R are anti-correlated, this solution also uniquely determines R. Different values of σ and Δ would yield different but still fully specified solutions for v and R.

Equation (VI.4) shows that v depends directly on the cation concentration gradient $\nabla c(r, t)$. Hence, the v and R selection-property suggests the following means of controlling R in the DENA technique. Increasing $\nabla c(r, t)$ would increase v and, by the v-R anti-correlation, reduce R. Technically, R is the tip-radius whereas we seek control over the wire-radius; in most types of dendritic growth, these two properties are not equivalent. In the DENA approach, however, deposition occurs exclusively at the tip, so the wire grows with a fixed diameter. Hence, controlling the tip-radius is effectively the same as controlling the wire-radius. As shown next, the use of a time-varying electric potential to induce deposition enables the desired sort of experimental control over $\nabla c(r, t)$.

VI.3.2 *Spherical diffusion*

Velocity-control may be demonstrated by considering *non-stationary* diffusion onto a spherical solidification front. We invoke the approximation that $\nabla \phi(r,t) = 0$, implying that the extent of spatial variation of the potential is much less than the relevant length scales in this problem; this assumption is justified in the *Discussion* section. While not rigorously correct, one can learn a lot from simple models, and as there is little discussion of non-stationary diffusion in the dendritic solidification literature, we invoke this assumption here. Hence, Equation (VI.1) simplifies to

$$\nabla^2 c(r,t) = \frac{1}{D}\frac{\partial c(r,t)}{\partial t}. \qquad \text{(VI.7)}$$

The time derivative may be converted to an algebraic expression by Laplace transformation of both sides:

$$\nabla^2 \tilde{c}_1(r,s) = \frac{s}{D}\tilde{c}_1(r,s) - \frac{1}{D}c_1(r,0) \qquad \text{(VI.8)}$$

where $c_1(r,t) = c_o - c(r,t)$ is the deviation from the bulk concentration c_o at r and t, and $\tilde{c}_1(r,s) = \int_0^\infty c_1(r,t)e^{-st}dt$ is the Laplace transform of $c_1(r,t)$. The boundary conditions for $c_1(r,t)$ are

$$c_1(r \to \infty, t) = 0 \qquad \text{(VI.9a)}$$
$$c_1(r,0) = 0 \qquad \text{(VI.9b)}$$
$$c_1(R,t) = c_o - c_{Int} \qquad \text{(VI.9c)}$$

where R is the radius of the growing sphere, and c_{Int} is the metal cation concentration at the sphere-solution interface. After invoking conditions (9b) and (9a), the general solution reduces to $\tilde{c}_1(r,s) = r^{-1}Ae^{-\sqrt{\frac{s}{D}}r}$. A is found via boundary condition (9c), and the solution becomes

$$\tilde{c}_1(r,s) = (c_o - c_{\text{int}})\frac{R}{r}\frac{e^{-\sqrt{\frac{s}{D}}(R-r)}}{s}. \qquad \text{(VI.10)}$$

Inverse Laplace transformation yields

$$c(r,t) = c_o - (c_o - c_{\text{int}})\frac{R}{r}erfc\left(\frac{r-R}{\sqrt{4Dt}}\right). \qquad \text{(VI.11)}$$

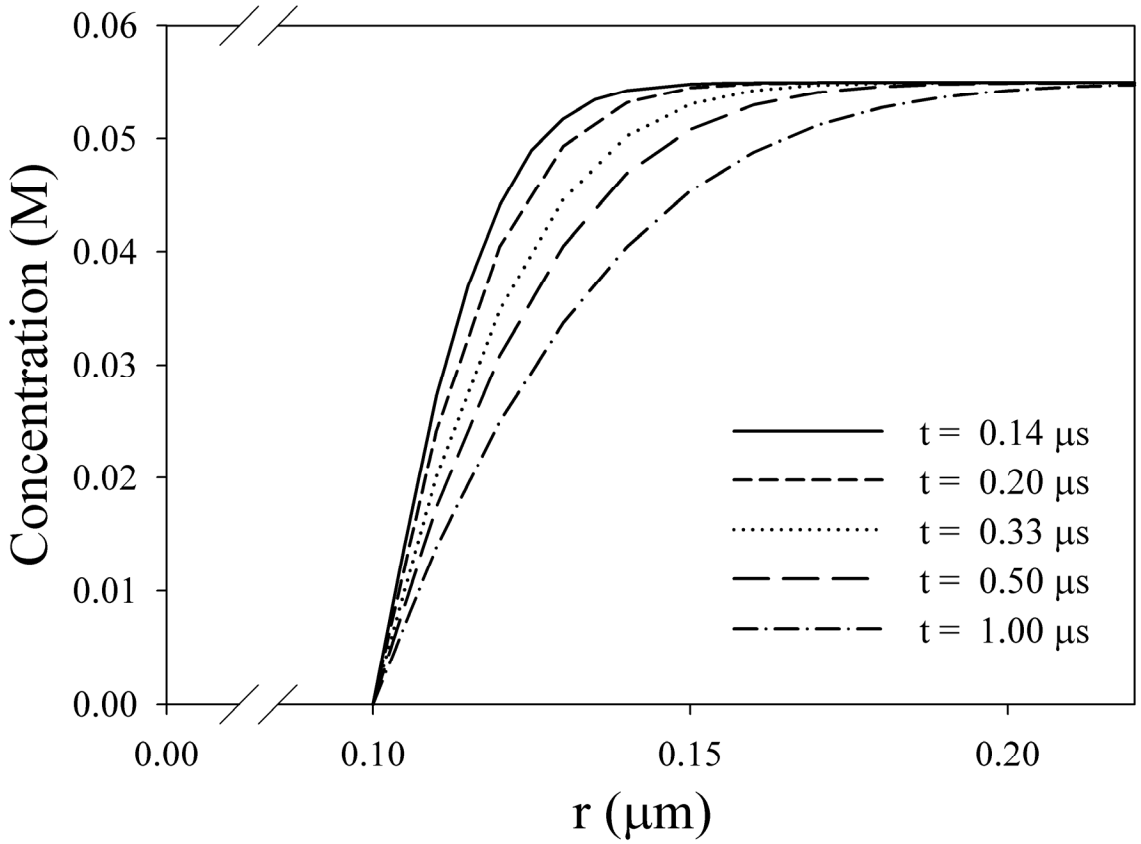

Figure VI.3. Plots of Equation (VI.11) for typical values of t that occur during one half cycle of the applied voltage signal. Values of D = 1000 μm^2/s and R = 0.100 μm were used in calculating these profiles.

Equation (VI.11) is plotted in Figure VI.3 for several values of *t* (0.14, 0.2, 0.33, 0.5, and 1 μs), using reasonable values for the parameters in Equation (VI.11) (see caption). These plots show that the concentration profiles flatten with increasing time *t*, during which deposition takes place. These *t*-values were chosen because they correspond to the *T*-values for the 0.5-3.5 MHz voltage signals used in the indium studies discussed below. This analysis shows that the concentration profiles evolve appreciably on the time scale of the half cycles used in this study.

The gradient of *c(r,t)* may be calculated, and at the sphere-solution interface where *r* = *R*, this quantity reduces to

$$\nabla c(r,t)\big|_{r=R} = (c_o - c_{\text{int}})\left(\frac{1}{R} + \frac{1}{\sqrt{\pi D t}}\right)\hat{r}\,. \qquad \text{(VI.12)}$$

Substituting Equation (VI.12) into Equation (VI.4) yields the following expression for the instantaneous *growth-velocity* of the spherical interface:

$$v(t) = D\left(\frac{c_o - c_{\text{int}}}{\rho_m - c_{\text{int}}}\right)\left(\frac{1}{R} + \frac{1}{\sqrt{\pi D t}}\right). \qquad \text{(VI.13)}$$

Equation (VI.13) describes the growth of a dendrite at time *t* during one half cycle of the applied electric potential, which oscillates rapidly, with a frequency on the order of 1 MHz. To measure the *growth-velocity* in the lab, we record real-time movies of growing wires at a frame capture rate of 9.1 Hz. What is observed, therefore, in these velocity measurements is an average of the instantaneous velocity expressed in Equation (VI.13) over one full voltage cycle (with 50% duty):

$$\bar{v}(T) = \frac{1}{2T}\int_0^T v_n(t)dt\,. \qquad \text{(VI.14)}$$

This definition assumes that no deposition occurs during the positive half-cycle. After making the substitution $\omega = (2T)^{-1}$, the frequency dependent velocity for a growing sphere $v_{obs}(\omega)$ is calculated to be

$$v_{obs}(\omega) = D\left(\frac{c_o - c_{\text{int}}}{\rho_m - c_{\text{int}}}\right)\left(\frac{1}{2R} + \sqrt{\frac{2\omega}{\pi D}}\right)\,. \qquad \text{(VI.15)}$$

Equation (VI.18) shows that the *growth-velocity* increases with square-root of the frequency of the voltage-waveform.

VI.4 Results

To assess the validity of this diameter-tunability approach, the velocities and diameters of DENA grown wires have been measured. Figure VI.4 plots the measured *growth-velocity* of a series of indium wires versus the frequency of the alternating voltage used to induce the growth of the wires. These data were obtained by imaging the electrode arrays on an inverted microscope equipped with a digital camera and recording 100-frame, real-time movies of the growing needle-shaped wires. The observed *growth-velocity* v_{obs} for each movie is constant. The instantaneous *growth-velocity* actually oscillates, with deposition occurring only during the negative half-cycles of the applied voltage-signal; however, this behavior is not observed because the movies are filmed at only 9.1 Hz. Hence, the observed *growth-velocity* is the average of the instantaneous velocity over one voltage cycle, as expressed by Equation VI.14). The measured v_{obs}

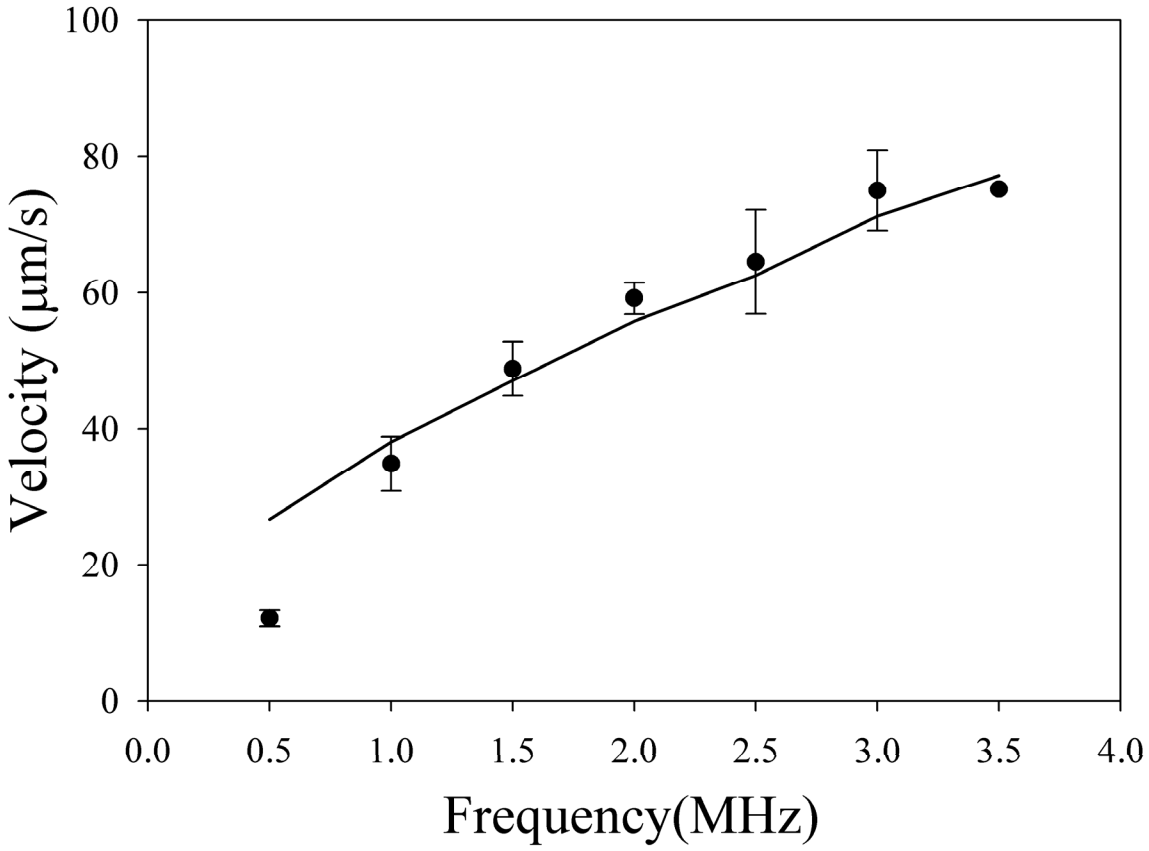

Figure VI.4. Wire *growth-velocity* as a function of the frequency. The solid line denotes a fit of Equation (VI.15) to these data.

values reported in Figure VI.4 were made by dividing the distance the wire grew during the movie by the time required to grow that distance. Each data point reflects the average of four such velocity-determinations per frequency (except for 3.5 MHz, for which only one measurement was made). The error bars represent the standard deviations of these averaged values. The solid line is a fit of Equation (VI.15) to the measured data. These data show that as ω increases, the wires grow with larger velocities.

The scanning electron micrographs in Figures VI.5a-c depict DENA-grown indium wires that were produced using 0.5 MHz, 1.0 MHz, and 3.5 MHz voltage-frequencies, respectively. All other experimental parameters (voltage-amplitude, electrode gap, and salt concentration) were held constant. It is apparent that the wire-diameters do not vary as a function of lengthwise position along the wires. Moreover, these series of images demonstrate that the wire-diameter decreases as ω is increased from 0.5 to 3.5 MHz. This dependence is explicitly plotted in Figure VI.5d where the diameter is shown to decrease from 770 to 114 nm across this ω-range. Each point in this figure reflects the average of 10 diameter measurements made on scanning electron micrographs of 10 different wire-samples that were dried in air before being imaged. The error bars are the standard deviations.

The DENA technique is not limited to wire-growth in $In(CH_3COO)_3$ solutions. Wires composed of different metals may be grown by altering the salt solution. Figure VI.6a depicts the frequency-dependent diameter of gold wires that were grown in 20 mM

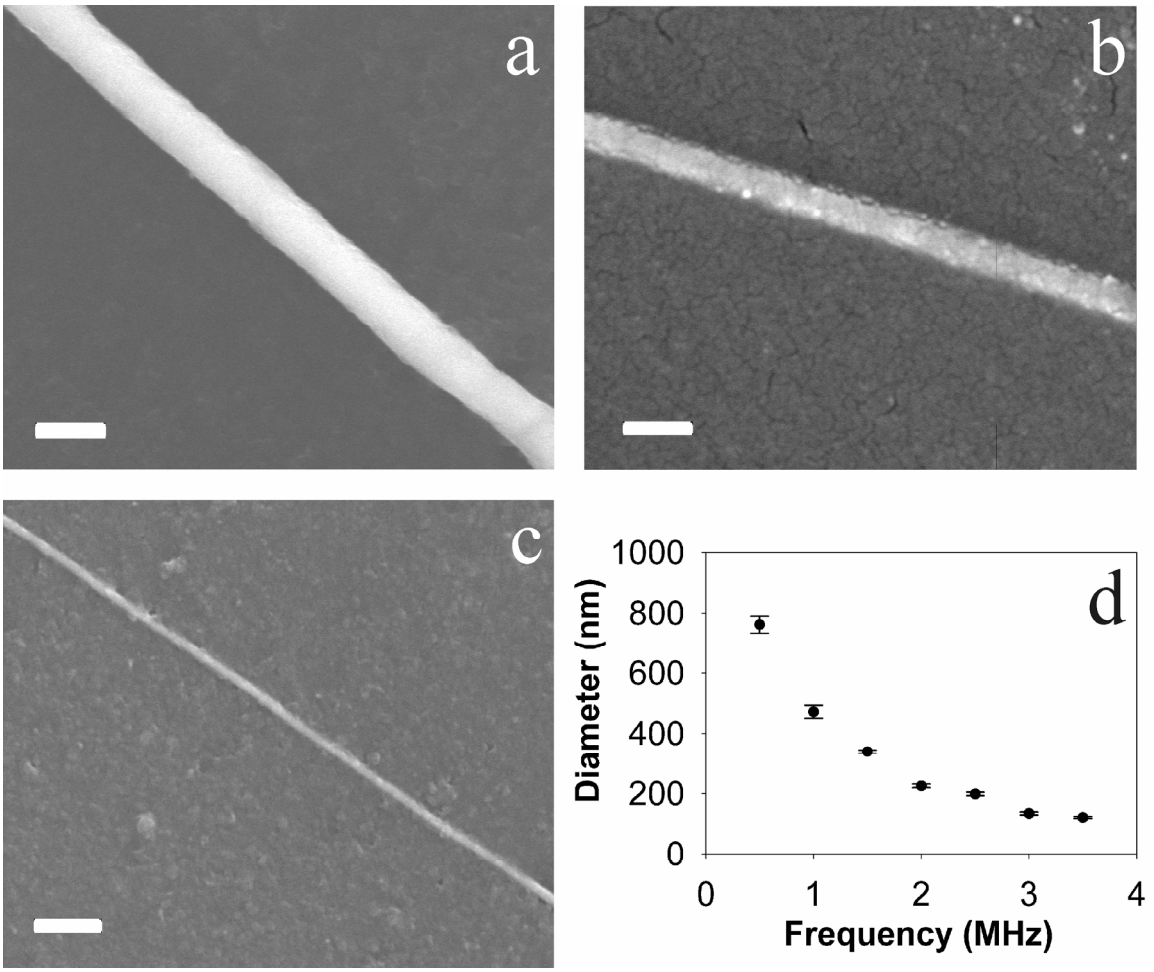

Figure VI.5. SEM micrographs of wires grown from 0.055 M $In(CH_3COO)_3$ solutions with voltage-frequencies of (a) 0.5 MHz, (b) 1.0 MHz, and (c) 3.5 MHz. The scale bars represent 1 μm. (d) Wire diameter as a function of the frequency of the alternating voltage.

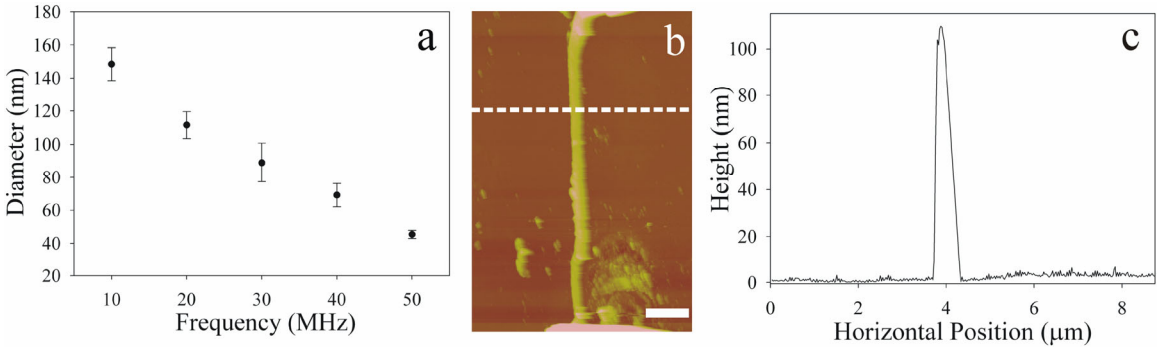

Figure VI.6. (a) Wire diameter as a function of the frequency of the alternating voltage for Au wires grown from aqueous solutions of $HAuCl_4$. (b) An atomic force micrograph of a gold wire grown across the 15 μm gap between two electrodes. (c) The height profile along the white dashed line in the topographical image in (b).

aqueous solutions of $HAuCl_4$. The diameter decreases from 150 nm to 45 nm as the voltage-frequency is increased from 10 MHz to 50 MHz. Each point in this plot reflects the average of 8 diameter-measurements made on atomic force micrographs of at least 2 different wire-samples per frequency. The error bars denote the standard deviations. These diameter-measurements were determined as follows. Figure VI.6b is a topographical image of a wire grown at 20 MHz that was collected using an atomic force microscope. Due to tip-convolution effects, the wire-dimensions in the image plane are inaccurate (*i.e.* they are too large); therefore, we obtained the diameter of the wire shown in Figure VI.6b by measuring line-cuts across the topographical image. A representative profile is shown in Figure VI.6c, indicating that the wire has a cross-sectional height of 109 nm.

VI.5 Discussion

The wire depicted in Figure VI.1a is a needle-shaped structure composed of near single crystalline indium.[190] A variety of other wire-morphologies may be produced via electrochemical deposition, and a phase diagram of DENA-produced morphologies has been published elsewhere.[190] As an example, the optical micrograph in Figure VI.1b depicts a dendritic structure grown under slightly different conditions (*i.e.* with a larger cross gap voltage) than employed for Figure VI.1a. The side-branch spacing is highly regular in this structure, looking somewhat like a TV antenna. This structure is typical of the dendritic solidification mechanism.[158, 193, 200] Therefore, it is probable that this mechanism underlies the formation of the antenna-shaped deposits shown in Figure VI.1b. Moreover, the DENA technique enables the smooth transition from needle-shaped

to highly branched deposition simply by changing the voltage amplitude. This observation suggests that the needle-shaped structures also result from dendritic solidification in the limit of suppressed side-branching. These branchless deposits are similar in appearance to the needle-shaped ice crystals that have been grown elsewhere by dendritic solidification.[149, 157, 212] Hence, we conclude that dendritic solidification plays an important role in the DENA approach.

This insight suggests that the properties of dendritic solidification may be exploited to realize precise diameter-control. As illustrated above, dendritic solidification theory implies that control over the velocities may be attained by controlling the cation concentration gradient. This relationship is explicitly shown in Equation (VI.4), where the *growth-velocity* is seen to depend directly on $\nabla c(r, t)$. Furthermore, Equation (VI.12) suggests that ω is a reasonable experimental parameter for controlling $\nabla c(r,t)$. To test the validity of this idea, the growth-velocities of needle-shaped indium wires were measured as a function of frequency. These data are plotted in Figure VI.4. In qualitative agreement with these theoretical considerations, the *growth-velocity* increases with increasing frequency across the 0.5 to 3.5 MHz range.

The solid line in Figure VI.4 is a best-fit of Equation (VI.15) to the $v_{obs}(\omega)$ data. In fitting these data, this equation has been rewritten as $v_{obs}(\omega) = a[R^{-1}(\omega) + (8\omega/\pi D)^{1/2}]$ where $a = \frac{D}{2}\left(\frac{c_o - c_{Int}}{\rho_m - c_{Int}}\right)$ is the only adjustable parameter. This figure shows that Equation (VI.15) describes the measured data reasonably well. The use of a frequency

dependent radius $R(\omega)$ in this fitting function reflects the anti-correlated relationship between v and R; the $R(\omega)$ values reported in Figure VI.5d were used. In fitting the $v_{obs}(\omega)$ data, we extracted a (unique) value of $a = 1.39 \times 10^{-3}$ $\mu m^2/s$. Using the definition for a given above and the values $c_o = 0.055$ M, $\rho_m = 7.31$ g/cm^3 = 6.37 M, and $D = 1000$ $\mu m^2/s$, the property c_{Int} was determined to be 20 mM. This value is less than c_o and, therefore, consistent with concentration profile proposed in Figure VI.2. Moreover, the good agreement between Equation (VI.15) and the experimental data shown in Figure VI.4 supports the notion that increasing ω increases v by steepening $\nabla c(r, t)$.

Qualitative agreement is really all that can be expected with this inexact analysis, which makes the following simplifying approximations: Equation (VI.15) characterizes a spherical solidification front whereas stationary dendritic fronts are known to be parabolic; a common c_{Int} is used for all frequencies, neglecting the radius-dependence of the Gibbs-Thompson effect that would yield a frequency-dependent c_{Int}; finally, Equation (VI.15) ascribes growth entirely to particle-diffusion, ignoring heat dissipation, surface attachment kinetics, and especially drift induced by the electric potential. This last assumption deserves some additional comment. The role of the electric potential in the DENA process is a complex issue. A 0.055 M In^{3+} solution has a Debye screening length of ~1 nm, indicating that a double layer will form at the interface between the solution and a negatively charged tip. This layer will screen the potential beyond a ~1 nm distance into the solution. The short range across which this potential extends compared to the diffusion length of the metal cations, estimated as $(2DT)^{1/2}$ ~ 31 nm,[213] suggests that the electric potential may be ignored in the solution. In this limit, the role of the

electric potential is simply to add negative charge density to the electrode-tip and, thereby, enable reduction of the metal cations. This reasoning is the basis for the simplified forms of the diffusion equation and the growth velocity given in Equations (VI.7) and (VI.4), respectively. However, this picture is only true before any deposition takes place. Once metal cations have begun to crystallize onto the electrode, the potential evolves in time.[197] It is possible that longer range components of the potential will arise during this process that will exceed the diffusion length. In such a case, the approximations leading to Equations (VI.7) and (VI.4) would become questionable. Nevertheless, the simplified theoretical approach employed in this study is a reasonable preliminary step towards a comprehensive understanding of the DENA technique because the main theoretical result, Equation (VI.15), provides a *non-stationary* description of diffusion limited growth. With few notable exceptions,[214, 215] most previous studies of dendritic growth have not analyzed the non-stationary form of the diffusion equation because most previous experimental work has been of a stationary nature. Hence, even though this theoretical approach is approximate, it provides a useful analysis-formalism for this study because it characterizes the dynamic nature of the concentration field: the crucial element of this nanowire fabrication approach.

The data shown in Figure VI.4 establish ω as a parameter for controlling the *growth-velocity* of the nanowires. By the *v*-*R* anti-correlation, increasing *v* is expected to reduce *R*. In dendritic solidification theory, *R* is the tip-radius, not the wire-radius. However, as illustrated by the images in Figures VI.5a-c, DENA-grown wires have lengthwise uniform diameters, indicating deposition occurs exclusively at their tips.

Hence, controlling the tip-radius is effectively the same as controlling the wire-radius. Thus, the *v-R* anti-correlation is expected to provide control over the wire-diameters. As illustrated by Figures VI.5a-d, we have found this to be true: the diameters of indium nanowires may be varied from 770 nm down to 114 nm as ω is increased from 0.5 and 3.5 MHZ. Thinner indium wires may be grown with frequencies greater than 3.5 MHz, but they dissolve upon removal of the applied voltage, possibly due to the Gibbs-Thompson effect. Conversely, gold nanowires with sub-100 nm diameters do not dissolve upon removal of the applied voltage. Figure VI.6a shows that gold nanowire-diameters may be varied from 150 nm down to 45 nm. An important challenge is to learn how material properties such as the surface tension and the diffusivities (both solution-phase and surface) dictate the range across which the diameters for a particular type of metal wire may be varied. This issue lies beyond the scope of this study. Nevertheless, it is clear that ω, an easily tunable experimental parameter, may be used to precisely tune the diameters of DENA-grown wires from the microscale down to the nanoscale.

This qualitative agreement between theory and observation regarding ω-dependent growth illustrates how the proposed non-stationary diffusion-picture provides a useful description of the DENA process. It is instructive to consider how this approach differs from stationary diffusion limited growth, which is the better characterized type of dendritic solidification. In stationary growth, the instantaneous and time-averaged velocities are equivalent. In the DENA approach, v_{obs} is constant for a given frequency, but the instantaneous growth-velocity *v(t)*, as expressed by Equation (VI.13), is not constant. Rather growth occurs during the negative half-cycles of the voltage signal;

during these periods the electrode tip carries a large negative charge density,[209] maximizing the probability that a metal cation will collide with, be reduced, and crystallize onto the tip. The fact that the wires grow as highly pure, near single crystalline indium indicates that the counter-ions are not oxidatively deposited onto the tip during the positive half-cycle of the voltage-signal;[190] what does happen to the counter-ions during these periods is an important outstanding question. During a positive half-cycle, $v(t)$ equals zero because the electrode becomes positively charged and is no longer capable of reducing cations. Thus, the wire-growth oscillates (with a frequency of ω) between periods of rapid but slowing growth and no growth.

A more detailed view is obtained by considering the amount of indium that is deposited during one cycle of the applied voltage-signal. This information can be obtained from the ω-dependent volume deposition rate, which is given by the product $v\pi R^2$ where the v and R values were taken from Figures VI.4 and VI.5d. A half cycle of a 0.5 MHz square-wave lasts 1 μs, so Figure VI.7 indicates that ~6×10^{-6} μm^3 of indium are deposited during this period. In a tetragonal crystal, an indium atom occupies a volume of 2.6×10^{-11} μm^3. Thus, ~230,000 indium atoms are deposited in one 0.5 MHz half cycle. Wires grown at 0.5 MHz have an average radius R = 0.38 μm (Figure VI.5d). By approximating (*i.e.* underestimating) the surface area of the tip by the circular cross-sectional area of the wire (πR^2), each cycle is found to generate a new layer on the tip with a surface density of ~5.0×10^5 atoms/μm^2. For comparison, the density of the {110} surface (the growth-surface of these indium wires)[190] of bulk tetragonal

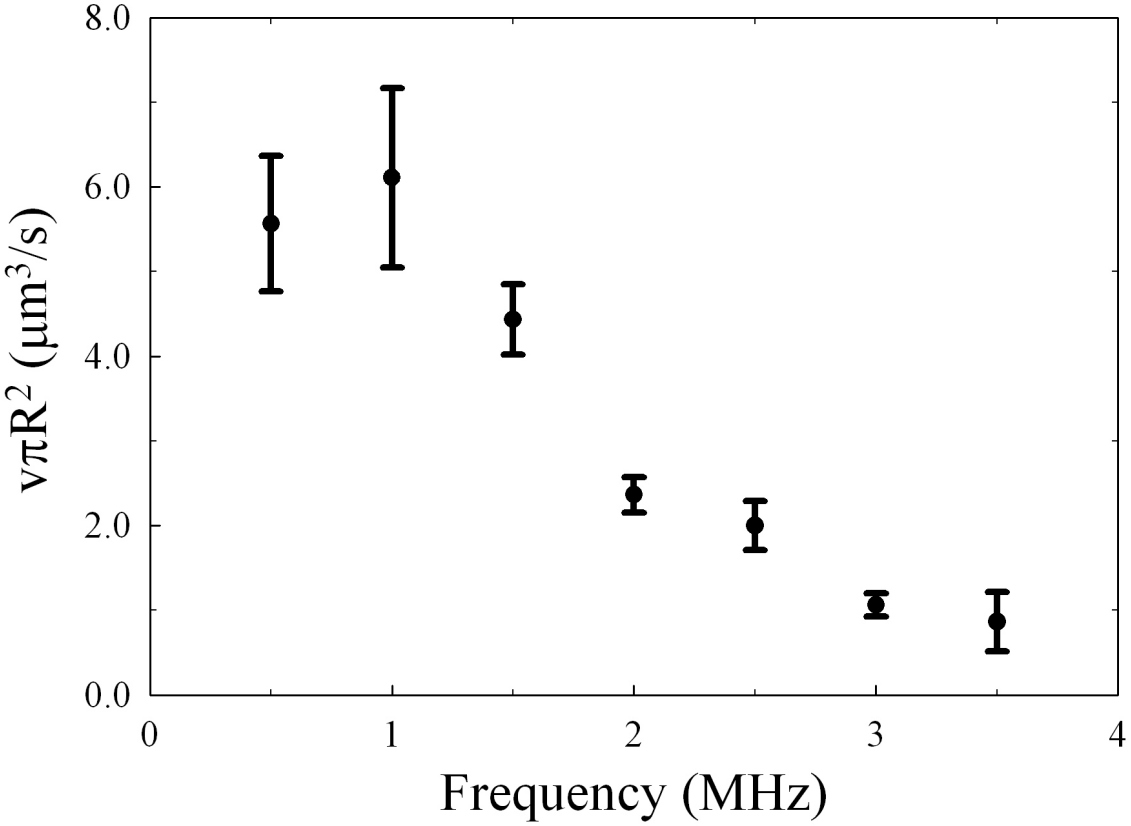

Figure VI.7. Net volume deposition rate of solid indium during wire-growth. The data points were obtained from the velocity and diameter data in Figures VI.4 and VI.5(d), respectively.

indium is ~4.4×10^6 atoms/μm^2.[153] Thus, much less than one monolayer of coverage is deposited per half cycle. The density of a newly deposited layer changes only modestly as the frequency is increased. A half cycle of a 3.5 MHz square-wave lasts 0.15 μs, so Figure VI.7 indicates that ~0.1×10^{-6} μm^3 of indium are deposited during this period; hence, ~3,800 indium atoms are deposited in one 3.5 MHz half cycle. Wires grown at 3.5 MHz have an average radius R = 0.060 μm (Figure VI.5d), so each 3.5 MHz cycle is found to generate a new layer on the tip with a surface density of ~3.4×10^5 atoms/μm^2. Therefore, this analysis indicates that sub-monolayer deposition per cycle occurs across the 0.5 to 3.5 MHz frequency range. It is not clear why the volume deposition rate decreases with increasing frequency, as shown in Figure VI.7. However, the pulsed nature of these deposition events coupled with the sub-monolayer coverage of atoms deposited per pulse may promote the growth of the (near) single crystalline wires that are observed for indium: the off-periods that punctuate the growth process provide time for the newly deposited adatom-populations to execute the attachment kinetics required for near well-ordered crystallization. This idea suggests that continuous growth or growth with shorter off-periods would be detrimental to single-crystal formation.

VI.6 Conclusions

The data presented here establish ω as a good experimental parameter for precisely controlling the growth-velocity and diameter of nanowires grown by the DENA technique. These ω-dependent behaviors are consistent with the notion that ω influences $\nabla c(r, t)$: increasing ω effectively steepens $\nabla c(r, t)$, thereby increasing v and, by the v-R

anti-correlation, reducing *R*. Thus, this work links dendritic solidification, a long-studied area of soft condensed matter physics, to metallic nanowire fabrication. In conjunction with our previous demonstration of low contact resistance interconnecting of DENA-grown wires, this study establishes a systematic approach to fabricating diameter-tunable electrode-nanowire-electrode assemblies for 1D transport studies. The preliminary results of diameter-dependent resistivity studies with DENA-grown gold nanowires are presented in Chapter VIII. Additionally, we have also demonstrated DENA-growth in $NiSO_4$, $Co(CH_3COO)_2$, $Pb(CH_3COO)_2$, and $AgNO_3$ solutions, producing wires composed of crystalline Ni, Co, Pb, and Ag, respectively; hence, this wire growth process is applicable to several different metals. We are working to broaden the types of DENA-active materials to include not only pure metals, but also alloyed and semiconducting compounds. Finally, it is reasonable to expect that this fabrication method can be further refined by exploiting the detailed understanding that the established theory for dendritic growth provides.

VI.7 Acknowledgement

This work was supported by the National Science Foundation (PHY-646966) and Oklahoma EPSCoR (EPS-132354).

Chapter VII: Single-Step Growth and Low Resistance Interconnecting of Gold Nanowires

Reprinted with permission from B. Ozturk, T. Mishima, D. R. Grischkowsky, and B. N. Flanders, *Nanotechnology*, 18, 175707, 2007.

www.iop.org/journals/nano

http://www.iop.org/EJ/abstract/0957-4484/18/17/175707

CHAPTER VII

SINGLE-STEP GROWTH AND LOW RESISTANCE INTERCONNECTING OF GOLD NANOWIRES

Abstract

We present a single-step, electrochemical approach to the growth and low contact resistance interconnecting of gold nanowires with targeted points on lithographic electrodes. Electron diffraction studies indicate that these nanowires are composed of face-centered cubic crystalline gold, and that the crystal structure is invariant along the wire-lengths. Four-point resistance-determinations of these electrode-nanowire-electrode assemblies consistently yield resistances of < 50 Ω, and the contributions from the electrode-wire contacts are of the order of 10 Ω. Atomic force microscopy was used to depict the structurally integrated nature of the electrode-wire contacts. This feature underlies the low electrode-wire contact resistances.

VII.1 Introduction

Nanowire synthesis is one of the most fundamental sub-processes of nano-device fabrication. Of the many elements and compounds from which nanowires may be made, gold is technologically important for its low resistivity (2.21 $\mu\Omega$·cm),[216] its inertness to

attack by air, and its resistance to sulfur-based tarnishing.[217] Additionally, gold is more biocompatible than most metals, rendering it suitable for implantation in[218, 219] or electrical interfacing with[220-222] cells and tissue in nano-biological applications.[223, 224] It may even prove feasible to perform novel electrophysiological characterizations of live cells by interfacing *multiple* gold nanowires with a *set* of targeted sites on a single cell, a challenging and long-standing goal.[222, 225] Finally, the well-established transport properties of *bulk* gold render the gold *nano*wire an ideal system in which to determine how metallic transport evolves with diminishing wire-diameter.[162] These research areas would benefit from a *gold* nanowire fabrication methodology that permits the targeted placement of the wires in surrounding circuitry and that attains low contact resistance interconnecting of the wires with this circuitry. This combination of features will foster predictable nanowire behavior in the assembled devices, and it will enable reliable characterization of the nanowire-transport properties.

A variety of fabrication techniques have been developed in the past decade that yield high quality nanowires. Perhaps the most widely used nanowire-synthesis is the vapor-liquid-solid method, where metallic nanodroplets catalyze the condensation, nucleation, and axial growth of vaporous growth-material.[171, 172] This technique produces pristine arrays of single crystal nanowires from a wide variety of materials,[42, 47, 160, 172-176] arrangements that have been exploited in various photonic[177] and electronic[178] applications. Recently, this approach was refined to allow for the catalyst-free growth of metal-silicide nanowires.[226] In an alternative approach, porous substrates,[182] nanotubes,[183] DNA, and other biomolecules[184] have been used as templates in the

formation of gold nanowires with very small diameters and a range of intricate shapes. Thus, the value of vapor-liquid-solid and templated growth in nanowire-fabrication is quite widely appreciated. However, a significant drawback to these established nanowire-syntheses is that connecting the individual wires with external instrumentation and with other submicron components is most often accomplished by secondary processing steps that follow the wire-synthesis. Two such approaches are known as blind sampling and piecewise-wire manipulation. These approaches limit the usefulness of the nanowires: blind sampling provides little control over the placement of the wires in the external circuitry, and piecewise manipulation is quite laborious. Furthermore, with both it is difficult to control the electrical properties of the electrode-nanowire junctions. Thus, methodology for the reproducible interconnecting of nanoscopic components with external circuitry is currently an area of intense research.[186-189]

Dielectrophoretic nanowire-assembly was developed, in part, to address this problem. This technique exploits the voltage-induced chaining and fusing of nanoparticles into wires that span the gaps between opposing electrodes; thereby, the wire-assembly and the electrode-wire contacts are accomplished in a single step.[93, 125, 137] This technique was later refined so that the wires could be grown between targeted points on the two electrodes.[138, 150] The transport properties of gold nanoparticle-based dielectrophoretic wires have been shown to have good reproducibility.[150] However, the resistivity of this material is ~2000 $\mu\Omega\cdot$cm,[93, 150] three orders of magnitude greater than that of bulk gold. The resistive nature of these wires is due in large part to their particulate structure, as evidenced by the occurrence of the Coulomb blockade at reduced

temperatures.[150] While such materials are needed for devices like variable capacitors,[147] the directed growth of more highly conductive, metallic wires is of obvious importance in nanoelectronics.

We have recently demonstrated the directed growth of indium nanowires by an innovative technique that we call *Directed Electrochemical Nanowire Assembly* (DENA). This technique induces directional electrochemical deposition in simple salt solutions to produce the metallic wires[190] and, like the dielectrophoretic approach, enables the *single-step* growth and interconnecting of the wires with targeted points in external circuitry. Unfortunately, the measured resistances of these electrode-wire-electrode assemblies varied from a low of 500 Ω to a high of 28 kΩ. These 60 μm long wires had diameters that ranged from 370 nm to 560 nm and were shown to be single-crystalline indium; thus, the resistivity of these wires should be well described by (and almost certainly not less than) that of bulk indium (8.6 $\mu\Omega\cdot$cm).[216] Using this resistivity-value, the contribution of these 60 μm long wires to the resistances of the entire electrode-wire-electrode assemblies is calculated to vary between 20 Ω and 50 Ω, depending on the wire-diameter. This resistance-range is much smaller than the measured kΩ-level resistances of these assemblies. A similar, unacceptable range of resistances was found for electrode-wire-electrode assemblies made from Pd wires that were grown by a similar electrochemical technique in an independent study.[99] The resistances of these assemblies varied from a low of 1.7 kΩ to a high of 10.2 kΩ, even though the 20 μm long, 200 nm diameter Pd wires examined in this study have a calculated resistance of only 70 Ω, where the bulk Pd resistivity (10.5 $\mu\Omega\cdot$cm) was used. Most probably, the electrode-wire-electrode

resistances are much larger than the expected resistances of these metallic wires because the electrode-wire contacts in these assemblies are very resistive.

This lack of control over the contact-resistance not only means that larger voltages are required to drive a given current through the wire, but could also qualitatively alter the electrical character of the wire. Nonmetallic transport behavior (*e. g.* a negative temperature coefficient of resistivity) occurs in a variety of disordered conductors, such as granular metals,[227] conducting polymer films,[228] and nanoparticulate nanowires.[150] The disordered junctions between metal nanowires and electrodes can induce similar behavior in metallic nanowires, as shown in a recent study of Pt nanowires interfaced with Au electrodes.[168] It is important that these interface-induced effects be minimized because they could mask temperature-dependent behavior that arises due to other basic transport processes. Of particular significance to nanoscience is the conduction of electrons through very thin wires. As the wire-diameter becomes comparable to the electronic mean free path, the resistivity is expected to increase.[163, 229] This occurs because, in addition to electron-phonon interactions (the canonical source of resistivity in metals), there is also the inelastic scattering of electrons at the surface of the conductor. As the electronic mean free path increases with decreasing temperature, the nanowire-diameter becomes the limiting length scale for electronic motion, causing electron-surface scattering to dominate over electron-phonon interactions. This effect will manifest itself as a temperature-independent resistivity for a given wire, or as a resistivity that increases with decreasing wire-diameter for a given material and temperature. Unambiguous experimental verification of this effect has yet to be reported

and is, thus, a long-standing issue in nanoscience.[165-168] Further characterization of this important process requires minimization of the electrode-wire contact resistances. Therefore, it is important that methodology for the low resistance interfacing of crystalline wires be established.

The present chapter reports on the single-step growth and interconnecting of near-single crystalline *gold* nanowires with targeted sites in on-chip circuitry. The contact resistances of the electrode-nanowire-electrode assemblies investigated in this study are of the order of 10 Ω. This accomplishment circumvents the need for the post-synthesis processing that would otherwise be required to interface the wires with external circuitry. As a result, the precise characterization of the transport behavior of such metallic nanowires is now possible.

VII.2 Experimental Details

VII.2.1 *Wire-Growth Circuitry*

Figure VII.1 shows a diagram of the wire-growth apparatus. The optical micrograph depicts a gold nanowire bridging the 10 μm gap between the tips of the electrode-pair. The electrodes are photo-lithographically deposited in 12-pair arrays on 0.5 mm thick quartz substrates and consist of a 100 nm thick base layer of Ti and a 500 nm thick top-layer of Au. The deposited metal was annealed by exposing the chip to a 425 °C argon-atmosphere in a tube furnace for 10 minutes, rendering the electrodes

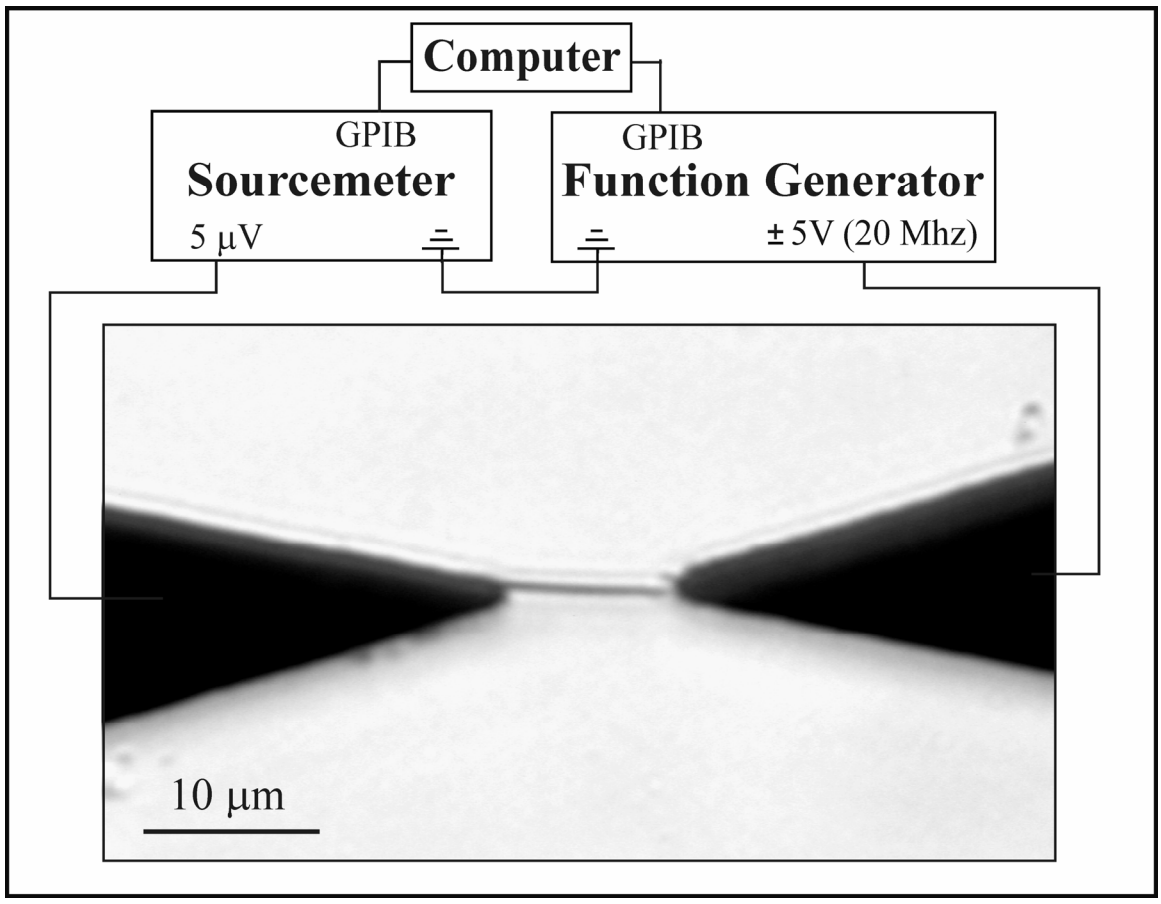

Figure VII.1. Diagram of the electrochemical wire-growth apparatus. The image is an optical micrograph of a gold wire grown between the tips of the lithographic electrodes. Each electrode tapers to a 1.5 μm wide tip and is connected via 120 μm wide conducting lines to macroscopic contact pads (not shown), enabling the interfacing of external instrumentation.

resistant to electrochemical degradation during wire-growth.[150] After depositing a 10 μl drop of 0.050 M aqueous $HAuCl_4 \cdot 3H_2O$ solution across the electrodes, an alternating voltage is applied across the gap in order to induce growth. The alternating lead of the function generator (Stanford Research Systems DS 345) is connected to the electrode from which growth is desired (the right electrode in Figure VII.1). The other electrode (*i.e.* the left electrode in Figure VII.1) is effectively grounded; that is, a very small (5 μV) voltage is applied to the left electrode (as explained below), but this signal does not affect wire-growth. A 20 MHz square-wave voltage was used to induce the growth of all the wires investigated in this study, and a Labview program (described below) was employed to actively adjust the function generator during wire-growth. This approach enabled reproducible contacts to be made between the wire and the electrodes. The wire spanning the gap shown in Figure VII.1 was imaged on an inverted microscope (Leica, IRB) equipped with a digital camera (Hamamatsu, Orca ER II).

VII.2.2 *Electronics for Attaining Low Contact Resistances*

In order to establish good contact between the wire and the electrodes, the alternating voltage-signal is actively adjusted as the wire grows across the gap. The Labview program responsible for this task rapidly terminates the alternating voltage after the nanowire bridges the gap, thus preventing excessive current from being driven through the electrode-nanowire-electrode assembly. To grow a wire, the user manually increases the amplitude of the 20 MHz voltage signal to ~5 V_{RMS}, or until wire-growth is observed (which usually takes ~30 s). As the wire grows across the gap, the user then reduces the voltage amplitude to ~2 V_{RMS} in order to suppress the tendency for these

wires to branch. The feedback signal for the control-program is a small, cross-gap direct current. The voltage source-meter (Keithley 2400) applies a small DC voltage (+5 μV) to the left electrode, as indicated in Figure VII.1. This small voltage does not perturb the wire-growth process. With this DC voltage, the source-meter can actively measure the DC current between electrodes. That is, before the wire bridges the gap, the cross-gap current is < 10 nA; however, when the wire contacts the left electrode, the feedback current increases dramatically. On reaching a specified value for the feedback current (we have found that 1 μA is a good value for 10 and 15 μm long wires), the program terminates the alternating voltage. This procedure prevents excessive alternating current from being driven through the wire when it bridges the gap, as such currents would break the electrode-wire contacts which function as electrical fuses in this circuit. As will be shown below, this automated procedure allows for consistent minimization of the contact resistance between the wires and the electrodes. This program is conceptually similar to that used previously in the dielectrophoretic growth of nanowires.[137]

VII.3 Results and Discussion

VII.3.1 *Structural Analysis*

The needle-shaped wire depicted in Figure VII.1a grows by a dendritic solidification process. For a given electrode-gap and geometry, variation of the voltage amplitude, its frequency, and the $HAuCl_4$ concentration gives rise to a range of wire-morphologies. For example, Figure VII.2a depicts a highly branched, tree-shaped structure that is typical of metallic dendrites.[193] This structure grew across the 10 μm

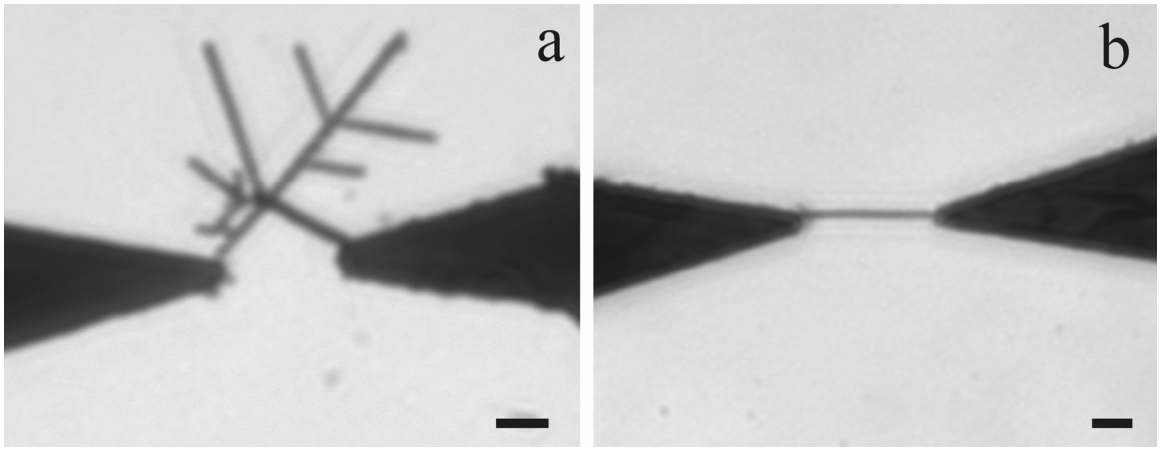

Figure VII.2. (a) An optical micrograph of a *dendritic structure* that was grown by the DENA technique when an 8 V_{RMS} signal was applied across a 0.050 M $HAuCl_4$ solution. The scale bar denotes 5 μm. (b) An optical micrograph of a *needle-shaped wire* that was grown under the same experimental conditions except that a reduced voltage-amplitude of 6 V_{RMS} was used to initiate growth, and the voltage was reduced to 2 V_{RMS} as the wire grew across the gap. The scale bar denotes 5 μm.

electrode gap upon application of an 8 V_{RMS}, 20 MHz voltage signal to a 0.050 M $HAuCl_4$ solution. This voltage signal was held constant as the wire grew across the gap. In contrast, Figure VII.2b depicts a wire that was grown under the same experimental conditions except that a reduced voltage-amplitude of 6 V_{RMS} was used to initiate growth and the voltage amplitude was reduced to ~2 V_{RMS} as the wire grew across the gap. This branchless wire has a needle-shaped morphology. Hence, this result suggests that reducing the voltage amplitude during growth either suppresses sidebranching or lengthens the side-branch spacing to a value greater than the electrode gap-length. Articulation of the mechanism underlying these behaviors lies beyond the scope of this study; however, the needle-shaped structure is a well characterized member of the many possible morphologies that may be produced via dendritic solidification.[149, 157] Furthermore, we have also observed voltage-induced suppression of dendritic sidebranching with In nanowires,[190] suggesting that this effect is a general characteristic of the DENA technique.

A 200kV transmission electron microscope (TEM) made by JEOL (JEM-2000FX) was used to obtain detailed crystallographic information of the needle-shaped wires. Because the quartz substrates of the electrode arrays are not thin enough to transmit the electron beam, it was necessary to transfer the wires to TEM grids. Transfer was accomplished by using a micromanipulator to slide a TEM grid (Ted Pella) across the wire-laden electrode gap. This process broke the wires off of the electrodes and deposited them onto the grid. Figure VII.3a shows a TEM micrograph of a single wire that was mounted in this manner. This image was collected with the electron beam

normal to the sample-plane. The wire is needle-shaped with sparse side-branching, having a diameter of 143 nm. Although much longer wires were present on the grid, this wire was chosen because it resided over a hole in the carbon netting of the grid. Hence, a clean diffraction pattern without contributions from the amorphous netting could be attained.

The composition of this wire was determined via electron diffraction. Figure VII.3b depicts a selected area electron diffraction pattern collected from the wire-segment in Figure VII.3a. Figure VII.3c shows a simulated [110] diffraction pattern that was calculated using a commercial software package (Virtual Laboratories, Desktop Microscopist), requiring as input the camera length (790.8 mm), the electron wavelength (2.51×10^{-3} nm), and the known structural parameters of crystalline gold: a face centeredcubic crystal structure, with a = b = c = 0.40786 nm, belonging to symmetry group $Fm\bar{3}m$.[153] The experimental and simulated diffraction patterns are in excellent quantitative agreement with each other. For example, on the TEM film the distances of the $\bar{1}11$ and 002 spots from the 000 spot are 8.40 mm and 9.73 mm, respectively; the angle subtended by these diffracted spots is 54.2º ± 0.4º. The corresponding calculated values are 8.43 mm, 9.73 mm, and 54.7º. The error for each of these quantities is less than 0.91%. This close quantitative agreement indicates that the wire is composed of crystalline gold. Of 10 wires examined in this manner, all were face-centered cubic crystalline gold.

To determine the structural continuity of the crystalline regions of these wires,

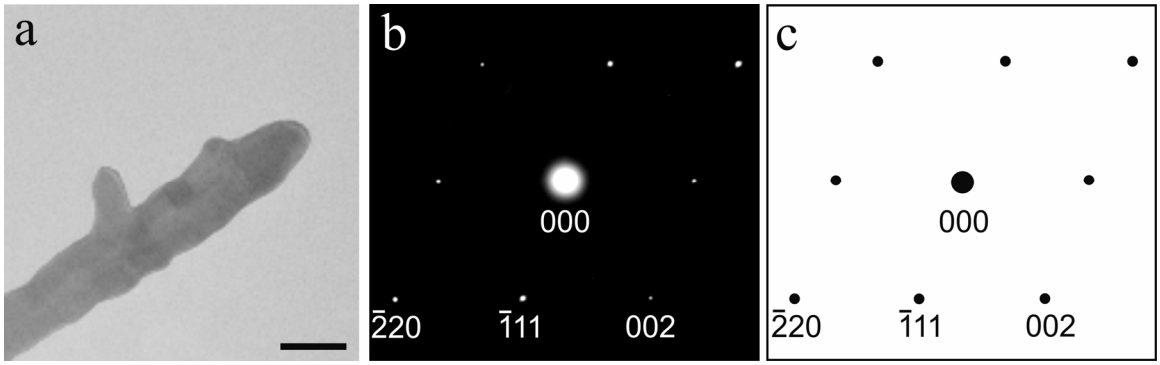

Figure VII.3. (a) TEM image of a gold wire. The scale bar denotes 100 nm. (b) The measured diffraction pattern of the wire-segment in a). For the sake of maintaining clarity during reproduction, the contrast of this pattern has been inverted. A 1.0 μm aperture was used to define the electron beam diameter for this measurement. (c) The calculated diffraction pattern of crystalline gold, observed from the [110] direction.

selected area diffraction patterns were collected from successive positions along the wire-lengths, using an area selection aperture with a 6.6 μm diameter. Figure VII.4a depicts a TEM micrograph of a 19.3 μm long gold nanowire grown by the DENA technique. The inset shows an enlarged view of the central portion of this wire. The diameter is 75.4 nm. Figures VII.4b-d represent diffraction patterns captured from the lower, middle, and upper sections of the wire shown in Figure VII.4a, respectively. Analyses of the discrete patterns in Figures VII.4b-d indicate that all three diffraction patterns result from crystalline gold observed from the $\langle 111 \rangle$ direction (confirming the compositional assignment made above). The diffuse rings in these images result from the amorphous carbon strands of the TEM grid beneath the wire-segment, which are visible in panel (a). Moreover, in each of the three images, the 6 spots positioned at the hexagonal vertices, constituting the $\langle 111 \rangle$ diffraction pattern, are identically oriented. Furthermore, they are located the same distances from the 000 spot and no double (or multiple) sets of diffracted spots are visible. These observations indicate that the crystal structure of this wire-segment does not deviate along its 19.3 μm length. Of 10 wire-segments examined in this manner, all 13 μm or greater in length, the crystal structures were found to be similarly invariant along the length of each segment. These results are consistent with the conclusion that the wires grow as *single crystals* of pure gold, as was previously observed with electrochemically grown indium wires.[190] However, one of these samples (*i.e.* that shown in Figure VII.3a) exhibited a diffraction pattern with two identical but slightly separated sets of spots when it was rotated and observed from the $[0\bar{1}1]$ direction. This observation indicates that this wire has a twinned crystal structure.

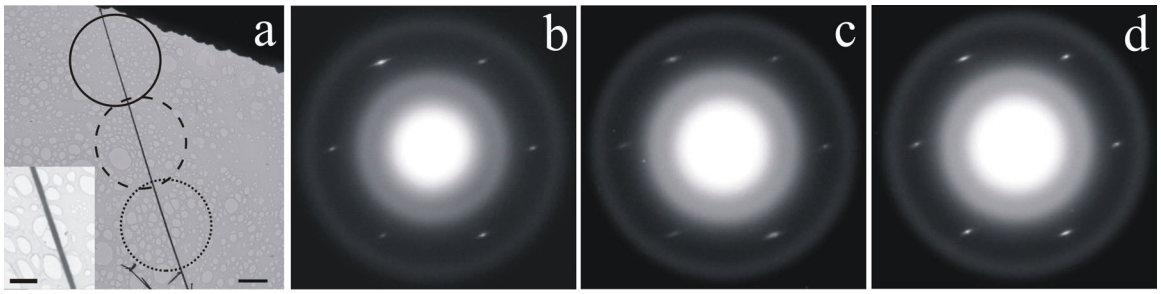

Figure VII.4. (a) A TEM micrograph of a 19.3 μm long gold wire on a TEM grid. The scale bar denotes 2 μm. The inset depicts an enlarged view of the central portion of this wire. The scale bar in the inset denotes 200 nm. The selected area diffraction patterns measured from the regions in panel a) denoted by the (b) dotted circle, (c) dashed circle, and (d) solid line circle. A 6.6 μm aperture was used to define the electron beam diameter for this study.

Determination of the extent to which twinning occurs in these wires awaits the orientationally resolved, transmission electron diffraction-based study of many wires and, therefore, lies beyond the scope of this study. Nevertheless, this study clearly demonstrates that the DENA technique produces lengthwise structurally invariant gold nanowires.

VII.3.2 *Charge-Transport Properties*

The resistances of these electrode-nanowire-electrode assemblies are very low—consistently less than 50 Ω (as compared to the kΩ resistances of electrochemically grown In and Pd nanowires); hence, the four-point method has been used to characterize the transport properties. Figure VII.5a depicts the layout for these measurements. The current was supplied by connecting the leads of a current source (Keithley 2400) to the contact pads on the electrode arrays. The on-chip distance between a contact pad and an electrode tip was 14 mm. Two high precision manipulators were used to interface submicron-sized probes (MicroManipulator) to the electrode-pairs with each contact point being ~ 100 μm from each tip. These probes served as the leads of a microvolt meter (Keithley 2400). With this set-up, the voltage difference between these contact points was measured as a function of the pad-to-pad current to generate the 4-point current-voltage profiles.

The solid lines in Figure VII.5b depict the 4-point current-voltage profiles of 8 electrode-nanowire-electrode assemblies that were grown via the feedback-controlled

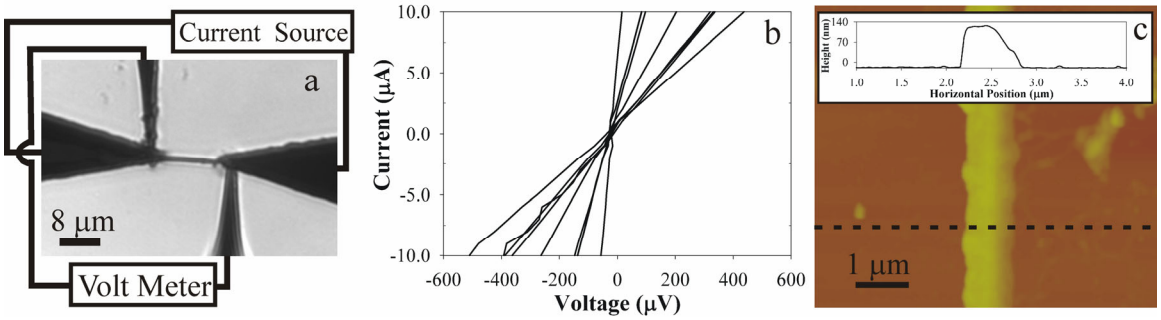

Figure VII.5. (a) Layout for a 4-point resistance measurement of a nanowire. The optical micrograph depicts a gold wire bridging a 10 μm electrode-gap. The microprobes make contact with the electrodes near the electrode-nanowire junctions. (b) 4-point current-voltage profiles (solid lines) of 8 different nanowires grown with the feedback-controlled growth procedure. (c) A topographical image of a gold nanowire. The inset depicts its height profile along the dashed line in the image. The average height of this wire along the length shown in this image is used for its diameter.

voltage application procedure. These measurements were conducted at 298 K on dried samples that were characterized by 10 μm electrode gaps. The steep slopes of these profiles indicate that all 8 electrode-wire-electrode resistances R_M are less than 50 Ω. electrode-nanowire-electrode assemblies that were grown via the feedback-controlled These measured values for R_M are 3.6 Ω, 12.2 Ω, 13.0 Ω, 23.4 Ω, 35.0 Ω, 35.8 Ω, 36.0 Ω, and 47.8 Ω. Conversely, the resistance of a typical electrode-nanowire-electrode assembly that was grown without using feedback-controlled growth is ~40 kΩ. A similar study of electrochemically grown Pd nanowires determined that a typical electrode-nanowire-electrode assembly had a resistance of 1.69 kΩ, whereas the resistance of the 20 μm long, 200 nm wide Pd wire would have been ~70 Ω were the contact resistances negligible.[99] The low values for the electrode-nanowire-electrode resistances shown in Figure VII.5b strongly suggest that the electrode-wire contacts are well-made and, therefore, the kΩ-level resistances attained previously are avoided. As we will show below, the electrode-wire contact resistance is of the order of 10 Ω.

Further analysis of the current-voltage profiles enables the wire-electrode contact resistances to be extracted. As Figure VII.5a suggests, these 4-point resistance determinations reflect five contributions: the resistance of the nanowire R_W, the two electrode-wire contact resistances expressed here as $2R_C$, and the resistances of the electrode-segments between the right and left microprobes and the nanowire; these are denoted by R_{ER} and R_{EL}, respectively. As these resistances are all in series, the measured resistance R_M may be expressed as $R_M = R_{ER} + R_{EL} + R_W + 2R_C$. (Because negligible current flows through the microprobes in this 4-point technique, the microprobe-electrode

contact resistances are not factors in these measurements).[230] As we will show, it is straight-forward to solve this equation for $2R_C$, in order to estimate the contact resistance of the electrode-nanowire-electrode assemblies.

R_{ER} and R_{EL} are determined as follows. Using a probe station, we have determined the resistance per length of the 120 μm wide conducting lines to be r_0 = 0.010 Ω/μm ± 0.001 Ω/μm. However, these lines taper to form the 1.5 μm wide tips, giving rise to a position-dependent resistance along the taper. As derived in the Appendix I, this geometry leads to the expression

$$R_E = r_0 L \ln\left(\frac{x_2}{x_1}\right) \qquad \text{(VII.1)}$$

for the resistance of the tapered electrodes. Here, the taper length L = 250 μm. x_2 is the distance between the microprobe-electrode contact point and the position of a perfectly sharp electrode tip (the apex). Due to the finite lithographic resolution that results in the 1.5 μm wide tips, the actual electrode tip is 3.1 μm nearer the microprobe-electrode contact point than the apex. x_1 is the distance between the electrode-wire contact point and the apex (taken to be 3.1 μm when the wire precisely contacts the actual 1.5 μm wide tip, as explained in the Appendix I). For the right electrode in this particular measurement, the nanowire contacted the right electrode precisely at its tip, so x_1 = 3.1 μm, and the microprobe contacted the electrode 65 μm from the (actual) tip, so x_2 = 65 μm + 3.1 μm = 68.1 μm. Thus, R_{ER} = 8 Ω. For the left electrode, this nanowire grew 5 μm past the tip before making contact with the electrode, so x_1 = 3.1 μm + 5 μm = 8.1 μm. The microprobe contacted the electrode 95 μm from the tip, so x_2 = 95 μm + 3.1 μm

= 98.1 μm. Thus, R_{EL} = 6 Ω. There is a precision ± 2 Ω associated with these R_{EL} and R_{ER} determinations due to the uncertainty in r_0.

R_W is determined as follows. We have shown that these wires grow as crystalline gold; additionally, the mean free path of room temperature gold is ~30 nm,[161] much smaller than the wire-diameters (the smallest of which is 75 nm), so size-induced effects on the resistivity of the gold wires is not expected, and the resistivity ρ of the nanowire may reasonably be equated to that of bulk gold, 2.21 $\mu\Omega$·cm. By measuring the length l and cross-sectional area A of the nanowire, R_W is determined via the equation $R_W = \rho l/A$. Atomic force microscopy (AFM) was used to determine the nanowire diameters. A typical AFM-based topographical image is shown in Figure VII.5c. (It is the R_M = 36.0 Ω wire that is depicted here). The line-cut in the inset shows that the height of this wire relative to the glass substrate is 133 nm. Moreover, the average height of this wire along the 5 μm length shown in this image is 140 nm ± 20 nm. Due to the absence of tip-convolution effects in the vertical dimension, the vertical features of AFM-based images reflect the size of nanoscale samples much more accurately than features in the image plane. Therefore, we model the wire as a cylinder with a 140 nm diameter and a 15.6 μm length; the length was determined from an optical micrograph of the wire (not shown). Hence, R_W is found to be 22 Ω. There is a precision ± 5 Ω associated with the R_W determinations due to the uncertainty in the wire diameter.

Inserting these values for R_W, R_{ER}, and R_{EL} into the equation for R_M yields a value

for the total contact resistance for this 36.0 Ω assembly of $2R_C$ = 0 Ω. As presented in Table VII.1, four other wires, *i. e.* those with R_M = 13.0 Ω, 23.4 Ω, 35.0 Ω, and 35.8 Ω, were also analyzed in this manner. This analysis indicates that the 13.0 Ω assembly had a total contact resistance of $2R_C$ = -5 Ω, the 23.4 Ω assembly had a total contact resistance of $2R_C$ = 6 Ω, the 35.0 Ω assembly had a total contact resistance of $2R_C$ = 11 Ω, and the 35.8 Ω assembly had a total contact resistance of $2R_C$ = 14 Ω. Due to the uncertainties in the wire-diameters and r_0, these determinations of $2R_C$ have a precision of ± 6 Ω; thus, the unphysical negative $2R_C$ value for the 13.0 Ω assembly reflects this uncertainty. This work demonstrates the ability of the DENA technique to establish electrode-nanowire contacts with consistently very small contact resistances. Finally, it should be noted that these estimates for $2R_C$ reflect the total contact resistance of the electrode-nanowire-electrode assembly, which contains 2 electrode-nanowire contacts. Thus, the maximum contact resistance of any individual electrode-wire junction is between R_C and $2R_C$.

The feedback-controlled voltage-termination procedure achieves continuous physical contact between both electrodes and the nanowire and, thereby, achieves low resistance interconnecting in the electrode-wire-electrode assemblies. Figure VII.6a depicts an atomic force micrograph (collected in amplitude-mode) of the junction between the *alternating* electrode and a DENA-fabricated nanowire. The electrode occupies the upper left portion of this image, and the wire extends from the electrode tip to the lower right corner of the image. This micrograph shows that the junction between the electrode and the wire is structurally well-integrated. DENA-wires grow from the alternating to the grounded electrodes, so it is not surprising that this junction is

Table VII.1. A summary of the various contributions to the measured resistances R_M of 5 different electrode-nanowire-electrode assemblies. The R_{ER} and R_{EL} values were each measured independently. The R_W values were determined by measuring the length and diameter of each of the wires and invoking the resistivity for bulk gold. The total contact resistance $2R_C$ was determined by subtracting R_{ER}, R_{EL}, and R_W from R_M.

Wire	$\mathbf{R_M}$	$\mathbf{R_{ER}}$	$\mathbf{R_{EL}}$	$\mathbf{R_W}$	$\mathbf{2R_C}$
1	13.0 Ω	9 Ω	7 Ω	2 Ω	-5 Ω
2	23.4 Ω	9 Ω	8 Ω	1 Ω	5 Ω
3	35.0 Ω	10 Ω	9 Ω	5 Ω	11 Ω
4	35.8 Ω	10 Ω	8 Ω	4 Ω	14 Ω
5	36.0 Ω	8 Ω	6 Ω	22 Ω	0 Ω

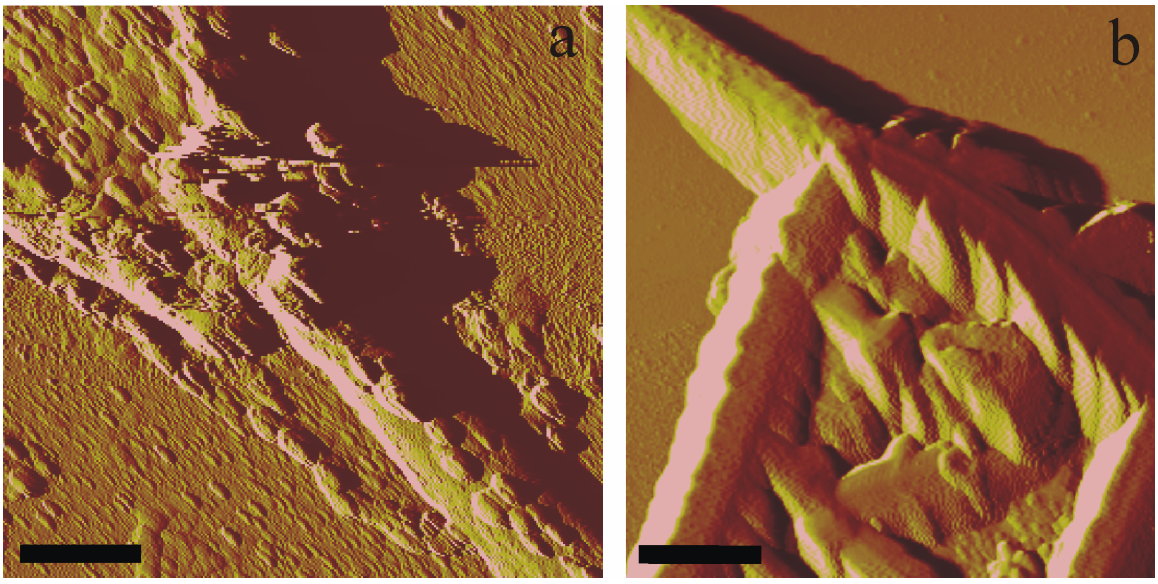

Figure VII.6. Atomic force micrographs collected in amplitude mode of (a) the junction between the alternating electrode and a DENA-fabricated gold nanowire and (b) the junction between the grounded electrode and a DENA-fabricated gold nanowire. The scale bars denote 1 μm.

structurally continuous: structural continuity establishes electrical continuity—a necessity for wire-growth in this electrochemical technique. Thus, the fact that wire-growth occurs at all suggests that good structural integrity is attained at the alternating electrode-nanowire junction. We have examined 12 alternating electrode-nanowire junctions via atomic force microscopy; all exhibited good structural integrity between the apex of the alternating electrode and the nanowire. Figure VII.6b epicts an atomic force micrograph of the junction between the *grounded* electrode and a DENA-fabricated nanowire. This is the electrode to which the wire grows in the DENA technique. The electrode occupies the lower right portion of this image, and the wire extends from the upper left corner to apex of the grounded electrode, where it branches into two segments. Each segment grows beyond the apex while maintaining direct contact with the surface of the grounded electrode. This extensive, physical contact between the branches and the electrode surface underlies the low electrode-wire contact resistance that characterizes this technique. We have used atomic force microscopy to examine 8 grounded electrode-nanowire junctions for electrode-nanowire-electrode assemblies that were fabricated using the feedback-controlled voltage-termination procedure. All were characterized by branching into multiple (2 to 4) segments at the grounded electrode apex and close physical contact between each segment and the surface of the grounded electrode. Conversely, electrode-wire-electrode assemblies that were produced without employing the feedback-controlled voltage termination procedure had large (~40 kΩ) resistances and failed to exhibit either of these structural properties at the grounded electrode-wire junction.

VII.4 Conclusions

This work establishes an innovative, electrochemical approach to growing crystalline gold nanowires between targeted sites in on-chip circuitry. Moreover, this single-step, automated procedure for growing and interconnecting nanowires reduces the electrode-wire contact resistance to the order of 10 Ω, eliminating the need for secondary processing steps that serve to interface the wires with the electrodes. It is the structurally integrated nature of the electrode-nanowire contacts that gives rise to the low electrode-wire contact resistance. As the directed growth and interfacing of wires is not easily attainable with other crystal-growth techniques, such as the vapor-liquid-solid mechanism,[159] this work is expected to prove useful in applications requiring the *in situ* growth of near-single crystalline interconnects. In particular, this capability is expected to critically facilitate future studies of diameter-dependent of charge transport in metallic nanowires.

To our best knowledge, the sub 15 Ω contact resistance of the electrode-nanowire-electrode assemblies described here is the smallest that has been attained by any *single-step* growth and interconnecting approach. We expect to reduce this resistance even more in a future effort that will focus on more extensive imaging of the electrode-wire contacts. By correlating the structure of these contacts with growth parameters such as the critical feedback current, the salt concentration, and the frequency of the alternating voltage, we expect to delineate an experimental protocol for precisely

controlling the structure of the electrode-wire junctions. This capability will allow for the consistent realization of electrode-wire interfaces with resistances of a few ohms or less.

VII.5 Acknowledgements

This work was supported by the National Science Foundation (NER-304413 and PHY-646966) and Oklahoma EPSCoR (EPS-132354). We thank Yuguang Zhao for applying his expertise towards the photolithographic fabrication of the electrode arrays, and we thank Mike Lucas for the care taken in machining the chip-transfer system required to anneal the chips in the tube furnace. We also gratefully acknowledge use of the Samuel Roberts Noble Electron Microscopy Laboratory of the University of Oklahoma.

CHAPTER VIII

DIAMETER-DEPENDENT RESISTIVITY OF DENA-GROWN GOLD NANOWIRES

Abstract

Diameter tunable gold nanowires were grown with the recently developed *directed electrochemical nanowire assembly* (DENA) method. Temperature-dependent four-point current-voltage measurements were conducted on these wires in order to investigate their diameter-dependent resistivity. Temperature-dependent resistance measurements were performed on three gold nanowires with diameters of 25 nm, 180 nm, and 491 nm. Each nanowire exhibited temperature-independent resistivity at temperatures below 50 K.

VIII.1 Introduction

The dimensions of most components in modern microchips and nanoscience fall in the range of 1-100 nm. While reducing the dimensions of these components is an attractive route, problems related to smaller feature sizes arise as new challenges. For example, thin metallic wires are widely used in microchips and unwanted Joule heating becomes more pronounced as the wire diameter gets smaller. When the diameter of a metallic nanowire is reduced to the length scales of a few tens of nanometers, the

electronic mean-free path becomes comparable to the nanowire diameter. Consequently, the electrons are expected to scatter inelastically at the surface of the nanowire in addition to the usual electron-phonon interactions. This behavior results in an increase of the nanowire-resistivity as the diameter is reduced.[231] Moreover, electronic mean-free path increases with decreasing temperature, making the diameter of the nanowire the limiting length-scale for the electronic motion. As a result, surface scattering of the electrons is expected to dominate over the electron-phonon interactions at low temperatures for a sufficiently thin nanowire. Thus, a temperature-independent behavior is expected for a very thin wire at low temperatures. While there have been many investigations on thin metallic films,[232-236] experimental verification of this issue with nanowires had yet to be demonstrated.

Several groups have investigated the diameter-dependent resistivity with metallic nanowires. Durkan and Wellend employed electron beam lithography to fabricate polycrystalline gold nanowires with rectangular cross sections where the thickness was 20 nm and the width ranged from 15 to 80 nm. An increase in resistivity with the decreasing wire width was observed and explained by a combination of surface and grain boundary scattering effects.[237] In another study, crystalline silver and copper nanowires were grown using templated growth technique and their bundles were employed in diameter-dependent resistivity experiments.[238] More recently, Penner and coworkers developed a new method for the electrodeposition of gold nanowires with rectangular cross sections by using a photolithographic undercut technique.[239] They were able to grow nanowires 18 nm in height and 40 nm in width with a ~5 nm precision. Their

temperature dependent resistivity data for an individual 20 nm thick gold nanowire showed that the resistivity of the nanowire is temperature-independent below ~180 K. While this result is impressive, a detailed theoretical analysis and structural characterization of the nanowire were not provided.

The recently developed, *directed electrochemical nanowire assembly* (DENA) technique enables the single-step growth and interconnecting of individual near single-crystalline metallic nanowires with targeted sites in external circuitry.[83, 84] The DENA-grown indium and gold nanowires were shown to be diameter tunable.[240] Electrode-nanowire-electrode assemblies of DENA-grown crystalline gold nanowires have low contact resistances, of the order of 10 Ω.[84] These properties motivated the utilization of DENA-grown gold nanowires in the diameter-dependent resistivity measurements. Here, we present preliminary data from such experiments.

VIII.2. Experimental

The gold electrodes employed in this study were prepared by standard photolithography techniques. Their characteristics and their annealing-procedure were described in Chapter VII.[84] Briefly, the electrode-arrays were mounted on an inverted optical microscope in order to observe the wire growth process. All the gold nanowires used in this study were grown from 10 mM aqueous solutions of $HAuCl_4$. After the deposition of 5 μl droplet of this solution across the lithographic electrode pair, a 50 MHz square wave signal was applied to the electrodes by using a function generator (HP 8116A). As the growth voltage amplitude was raised manually to ~5 V, the wire growth

started exclusively at the alternating electrode. The voltage amplitude was manually decreased during the wire growth in order to enable needle-shaped growth as opposed to branched growth.[84] The wire growth was stopped by manually terminating the alternating voltage just before the wire interconnects with the opposing electrode. At this point, the electrodes were connected to the previously developed LabView controlled growth voltage termination setup (see Chapter VII for details).[84] The function generator on this setup (Stanford Research Systems, DS 345) is capable of generating signals at a maximum frequency of 30 MHz. Thus, further growth and low-contact resistance interconnecting of the gold nanowire with the opposing electrode occurred with the application of a 30 MHz square wave signal.

After attaining low-contact resistance interconnecting, the growth solution was removed. The electrode tips were connected to the adjacent electrodes by using indium paste as shown in Figure VIII.1. The adjacent electrodes were used as the voltage probes in the temperature-dependent four-point current-voltage measurements. The electrode-nanowire-electrode assembly was transferred to a closed-cycle helium cryostat (Janis) for the temperature-dependent measurements. The details of the four-point resistance measurements were described elsewhere.[84] Atomic force microscopy (AFM) based topographical imaging was used to determine the nanowire diameters after the temperature-dependent resistance measurements. The lengths of the nanowires were determined from optical micrographs.

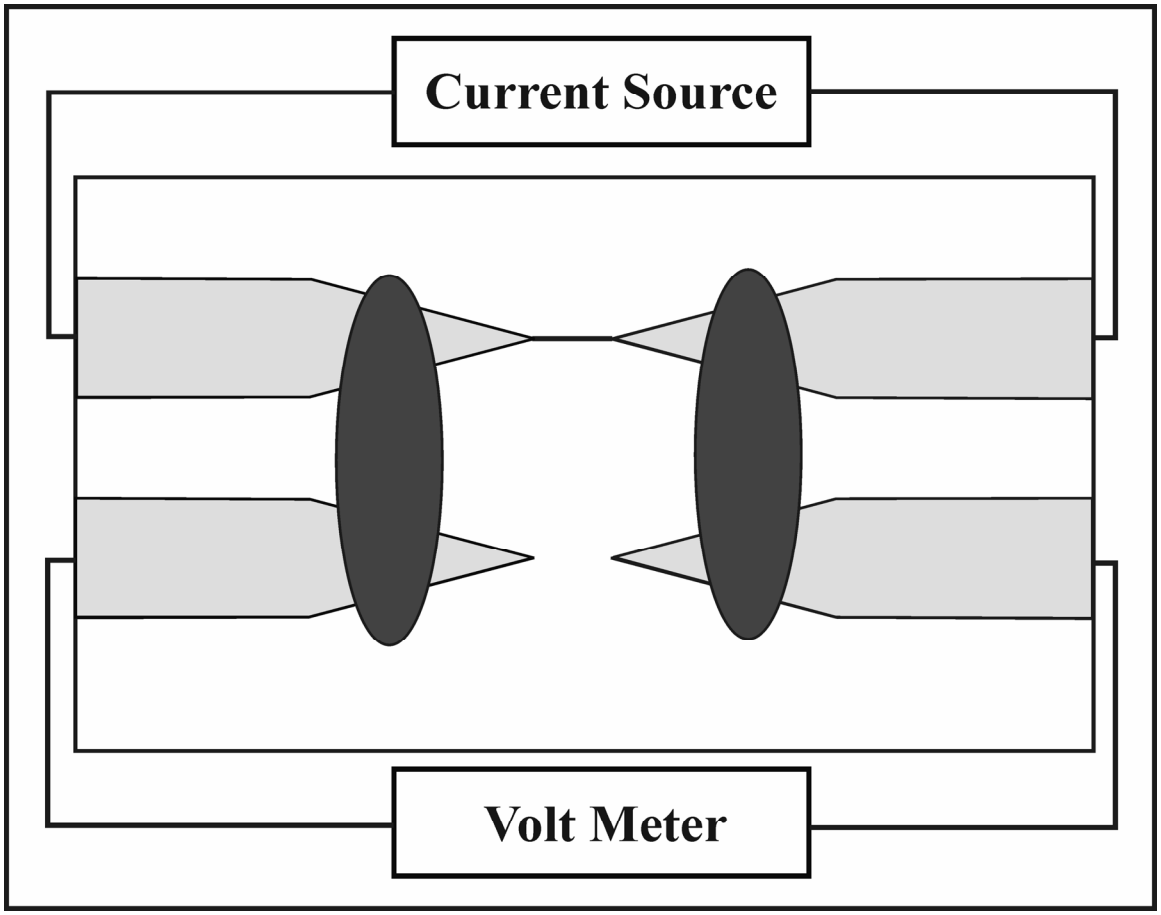

Figure VIII.1. The experimental diagram for the four-point resistance measurements. The gray protrusions represent lithographic electrodes. After the gold nanowire growth, the adjacent electrodes were connected to the wire growth electrodes using indium paste (black ellipsoids) as shown in the cartoon. The adjacent electrodes were used as probes of the volt meter.

VIII.3 Results and Discussion

Figure VIII.2 depicts the temperature-dependent resistivity data for three gold nanowires with diameters of 25 nm, 180 nm, and 491 nm. The resistivity values were calculated from the measured four-point resistance values and the nanowire dimensions. All the nanowires exhibited linear temperature-dependence in the 50-300 K range. The nanowires with diameters 491 nm (squares), 180 nm (triangles), and 25 nm (circles) exhibited nonlinearities in their temperature-dependent resistivities at temperatures of 20, 30, and 40 K, respectively: the profiles flatten at these temperatures. This behavior is suggestive of surface-scattering induced resistivity. However, the extent of the surface-scattering effect is not clear and further analysis of the data is required. In order to test the reproducibility of the data, more nanowires will be grown and measured in the near future.

In the temperature-dependent four-point resistance measurements, the voltage probes were located on the lithographic electrodes as depicted in Figure VIII.1. Thus, there are five contributions to the four-point resistance measurements: the right and left electrode segments between the indium paste and the nanowire, the two electrode-nanowire contacts, and the nanowire. The resistance contributions from these elements are denoted by R_{ER}, R_{EL}, $2R_C$, and R_W, respectively. As these resistances are all in series, the measured resistance R_M may be expressed as $R_M = R_{ER} + R_{EL} + 2R_C + R_W$. Equation VII.1 was employed in the calculation of R_{ER} and R_{EL}. The temperature-dependent resistance coefficient r_0 was required for the calculation of temperature-

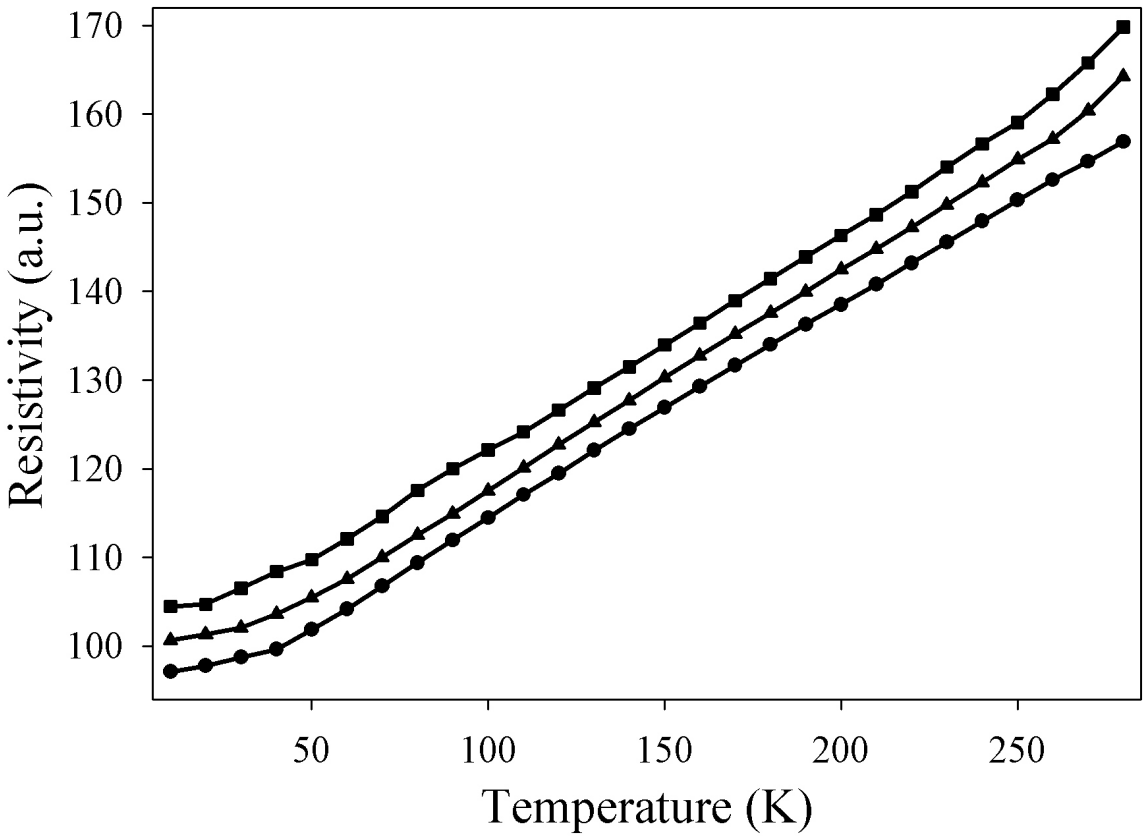

Figure VIII.2. Temperature dependent resistivity plots of gold nanowires with 491 nm (squares), 180nm (triangles), and 25 nm (circles) diameters. Resistivity values are multiplied by a factor of 27 for 25 nm diameter wire and by a factor of 1.95 for 180 nm diameter wire in order to facilitate comparison.

dependent R_{ER} and R_{EL}. To this end, an electrode gap was shorted with an indium paste and used in the temperature-dependent two-point resistance measurements in the 10-300 K range. These measurements provided r_0 values for the alloyed electrodes. The distance between the electrode-nanowire junction and the indium paste contact location (x_2) was measured for each electrode from the optical micrographs. The calculated temperature-dependent R_{ER} and R_{EL} values were subtracted from the temperature-dependent four-point resistance values for each nanowire. The resistivity values in Figure VIII.2 were calculated from these R_{ER} and R_{EL} subtracted resistance values. The four-point measurements also included two contact resistance contributions ($2R_C$) from the nanowire-electrode junctions. We determined $2R_C$ values by subtracting the nanowire resistance (R_W) and the electrode resistance contributions (R_{ER} and R_{EL}) from the measured resistance (R_M). The nanowire resistance was calculated using the measured dimensions and the resistivity of bulk gold (2.31×10^{-8} Ωm). The room temperature $2R_C$ values were determined as -273.60 Ω, 201.99 Ω, and 86.21 Ω for the wire diameters of 25 nm, 180 nm, and 491 nm, respectively. These contributions have not been subtracted from the data shown in Figure VIII.2.

Several issues need to be addressed in the future experiments. The mean-free path of gold was reported as ~30 nm at room temperature.[24] Thus, the temperature-independent resistivity behavior for the 25 nm diameter nanowire was expected to appear at higher temperatures. The contact resistances of the nanowire-electrode junctions were not analyzed in this study. The temperature-dependent behavior of these junctions may prevent the efficient characterization of the diameter-dependent resistivity of the

nanowires. The electrode-nanowire contact resistances and electrode resistance contributions can be avoided by depositing the voltage measurement electrodes on the nanowires by using electron beam lithography. Previously, the DENA-grown gold nanowires were shown to be near-single crystalline.[84] However, the crystal structure of the nanowires that are used in this study were not determined. Their structural characterization may provide further insight into the analysis of the resistivity data.

In conclusion, this chapter presents the results of the preliminary diameter-dependent resistivity studies where DENA-grown gold nanowires with different diameters were employed. The results are consistent with the predicted diameter-dependent resistivity.

CHAPTER IX

CONCLUSIONS AND FUTURE DIRECTIONS

IX.1 Summary of Results and Conclusions

The series of the projects covered in this work represents a systematic study on the assembly and characterization of nanostructures. As described in Chapter II, we initially employed quantitative film balance studies to probe the interparticle potential in the Langmuir films of CdSe nanoparticles. The dispersions of nanoparticles contained excess amounts of TOPO surfactant, whereas trace amounts of these molecules disrupt the interparticle potential-induced organization of CdSe nanoparticles at the air-water interface. We established a simple cleaning method to diminish the excess TOPO content to negligible levels of surface activity. The clean populations of nanoparticles ranging from 2.08 to 2.91 nm were used in the preparation of Langmuir films. The pressure-area isotherms of these films were fitted to the Carnahan-Starling expansion of the pressure of a 2D system of disks. The analysis showed that the CdSe nanoparticles of a given diameter behave like hard-disks with significantly smaller diameters which was possibly due to an attractive contribution to the interparticle potential, such as the dipolar potential. This information provides an insight into the interactions of the nanoparticles, thereby facilitating the development of assembly strategies. Dielectrophoresis is one such method frequently employed for the directed assembly of nanostructures.

We applied dielectrophoresis to the fabrication of interconnects from nanostructured building blocks between targeted points in the external circuitry. As semiconductors play an essential role in modern electronic devices, dielectrophoretic fabrication of low-dimensional semiconductor interconnects composed of nanoparticles may prove useful for fundamental research and viable device applications. To this end, we used clean populations of CdSe nanoparticles as stock solutions for dielectrophoretic interconnect formation. While we were not able to form dielectrophoretic interconnects from CdSe nanoparticles, we succeeded fabricating interconnects from 3.7 nm diameter semiconductor CdS nanoparticles. However, our analysis showed that interconnect formation from these small diameter particles was not feasible and an intermediate step was required. Particle sizing characterization of the stock solutions indicated the aggregation of 3.7 nm nanoparticles into 100 nm particles while preserving their nanoparticulate properties. Calculations showed that the interconnect formation was possible with these aggregates. Moreover, we observed electroluminescent flashes from the CdS nanoparticle interconnects as we further continued the application of AC voltage. The highest intensity peak in the optical spectrum of these flashes coincided with the fluorescence emission spectrum of CdS crystals. This observation indicated that the nanoparticulate CdS converts to bulk CdS during interconnect formation. Furthermore, the close match between the lower intensity electroluminescence peak and the CdS nanoparticle photoluminescence spectrum was attributed to the existence of CdS nanoparticles in the interconnect.

In another application of dielectrophoretic interconnect formation, gold nanorods were used as building blocks. The use of lithographic electrodes with well defined gaps enabled the fabrication of gold nanorod interconnects with reproducible resistance characteristics. However, the measured resistance values were in the order of kilohms and the analysis showed that the electrode-interconnect contact resistances were negligible in the kilohm range. High resolution TEM imaging of these interconnects indicated the presence of extensively fused islands of nanorods which are separated by a single nanorod. Temperature dependent current-voltage measurements showed that there is a threshold to charge conduction at low temperatures. These observations demonstrated the significance of Coulomb blockade as the conductance-limiting factor in these gold nanorod interconnects. Further analysis of the experimental data showed good agreement of the barrier energy with the calculated values. In conclusion, dielectrophoretic interconnects lack structural uniformity mostly due to their nanoparticulate composition. Consequently, their charge-transport characteristics do not represent the core materials of these nanostructures. While the observed characteristics may prove useful in various applications, fabrication of structurally uniform nanowires is desirable for most applications and fundamental research.

The limited charge transport properties of dielectrophoretic interconnects motivated us to develop an alternative approach for the growth of structurally uniform metallic nanowires between targeted points in external circuitry. This approach enabled facile fabrication of crystalline, metallic nanowires from simple salt solutions between protruded electrodes with the application of AC voltage, hence, we named this new

technique d*irected electrochemical nanowire assembly* (*DENA*). DENA was initially applied to the growth of indium interconnects from $In(CH_3COO)_3$ solutions. A good control over the nanowire morphology such as amorphous, dendritic, and needle shaped was established through the control of the growth voltage amplitude and stock solution concentration. High resolution transmission electron diffraction analysis showed that the nanowires were single-crystal indium which indicated high structural uniformity. However, most of the indium nanowire resistance measurements were in the range of several kilohms. As the wires were composed of single crystal indium, the high resistance values were attributed to the resistive nature of the electrode-nanowire junctions.

A mechanistic understanding of the DENA technique was required in order to better control and exploit its attractive properties. Dendritic solidification was identified as an important process in the growth mechanism of DENA nanowires, due to morphological resemblance. The anti-correlation between the growth velocity and the tip-radius is a characteristic of the dendritic solidification. The theoretical analysis predicted an increase in the wire growth velocity with the increasing frequency of the growth voltage. The increasing velocity is expected to reduce the tip-radius due to anti-correlation. In the DENA approach, nanowires were shown grow with fixed diameters, enabling direct control over the wire diameter by changing the tip-radius. Thus, increasing growth voltage frequency is expected to increase wire growth velocity and reduce the wire diameter. This behavior was experimentally observed in the DENA growth of nanowires. That is, indium nanowires were shown to grow faster with the

increasing growth voltage frequency. Also, both indium and gold nanowire diameters were observed to decrease with the increasing growth voltage frequency. As a result, the growth voltage frequency was established as an experimental parameter to control the nanowire diameter in the DENA technique.

We have demonstrated DENA nanowire growth with other metals such as gold, nickel, lead, cobalt, copper, and silver by using their simple salt solutions. Due to their ease of fabrication and structural uniformity, these DENA grown electrode-nanowire-electrode assemblies can be used in transport measurements such as diameter-dependent resistivity, Kondo effect and 1D superconductivity. The high contact resistance values obtained for the indium nanowires prevented the effective measurement of inherent transport properties of these nanowires. This issue motivated us to develop a feedback controlled voltage termination technique in order achieve low-contact resistance interconnecting of DENA grown nanowires with the lithographic electrodes. We applied this feedback controlled DENA technique to the growth of gold nanowires from aqueous $HAuCl_4$ solutions. The structure of these gold nanowires was shown to be near-single crystalline by electron diffraction analysis. A detailed investigation of the four-point resistance measurements of the gold nanowires indicated that the electrode-contact resistances are of the order of ~10 Ω. To our best knowledge, this value is the smallest that has been attained by any single-step growth and interconnecting technique.

In conjunction with other attractive properties, the low-contact resistance interconnecting capability motivated the use of DENA-grown nanowires in 1D transport

experiments. Recently, we employed DENA-grown gold nanowires in diameter-dependent resistivity measurements. When the nanowire diameter becomes comparable to mean-free path, the surface scattering of electrons are expected to dominate canonical electron-phonon interactions at low temperatures. This happens because the electronic mean-free path increases with decreasing temperature, and the nanowire diameter becomes the limiting factor for the electronic motion. As a result, a temperature-independent resistivity effect is expected at low temperatures. The preliminary data from a set of gold nanowires showed a weak effect below 50 K.

In conclusion, this work presents examples of self and directed assembly studies of nanostructures. Detailed information on the characterization of the nanostructures and their assembled forms was provided. The interparticle potential and charge transport properties of different nanostructured assemblies were discussed. DENA was developed as a new nanowire growth technique. This technique enabled single-step growth and low-resistance interconnecting of metallic nanowires with external circuitry. DENA grown nanowires were shown to be crystalline and diameter-tunable. Recent results of diameter-dependent resistivity measurements with the DENA-grown gold nanowires were also presented.

IX.2 Future Directions

DENA-grown gold nanowires were employed in diameter-dependent resistivity studies. While a weak effect was observed in our preliminary experiments, the data is not conclusive. We plan to grow gold nanowires with reproducible and smaller diameters. We expect to observe an enhanced effect with smaller diameter nanowires in the temperature dependent resistance measurements. The lithographic electrode contributions will be minimized with a new electrode design, where voltage measurements will be carried out at the electrode-nanowire contacts in the four-point measurements. A detailed theoretical analysis of the current and future data is necessary to probe the extent of resistivity contribution due to scattering of electrons at wire surfaces.

As described in Chapter VI, the frequency of the growth voltage has to be increased in order to reduce the diameters of DENA-grown nanowires. In the recent diameter-dependent resistivity measurements with gold nanowires, we employed a growth voltage frequency of 50 MHz. In our previous electron diffraction based structural analysis of gold nanowires that are grown at this frequency, one nanowire exhibited twinning defect. Thus, this type of crystal defects may hinder the diameter-dependent resistivity effect. In order to determine crystal structure of nanowires that are used in the diameter-dependent resistivity measurements, nanowires can be grown on special TEM grids with silicon nitride (SiN) windows. The lithographic electrodes can be fabricated such that the electrode gaps will coincide with the 100 nm thick window. This configuration will enable the observation of wire growth with optical microscope

and electron diffraction based structural analysis of the nanowires with TEM. Consequently, the structural information will assist the interpretation of the data from the transport experiments.

In addition to gold nanowires, we observed low-contact resistance interconnecting of DENA-grown nickel nanowires with external electrodes. Thus, their electrode-nanowire-electrode assemblies can be also employed in the future diameter-dependent resistivity studies. We also demonstrated DENA growth of cobalt, zinc, lead, silver and copper nanowires. As a part of future studies, crystal structure of these nanowires can be characterized. Electrode-nanowire-electrode assemblies of these nanowires can be also used in the future 1D transport experiments, provided that their low-resistance interconnecting with external electrodes is possible. For example, DENA-grown lead nanowires may exhibit superconducting behavior below 7 K as bulk lead does at such temperatures.

The extent of the magnetic characteristics of the DENA grown nickel and cobalt wires had yet to be demonstrated. Previously, we performed simple experiments and observed the movement of nickel nanowires with the application of external magnetic fields. Magnetic force microscopy (MFM) enables high resolution imaging of nanoscale magnetic domains that are buried beneath a topographically flat surface. Thus, nickel and cobalt nanowires can be covered with thin polymer films with spin coating. The polymer coating is expected to avoid tip-nanowire interactions which may cause imaging artifacts. MFM imaging of these polymer covered nanowires will provide information

about their inherent magnetism. A nanowire image should be obtained in the MFM mode if the nanowires possess inherent magnetism. In order to qualitatively characterize the extent of inherent magnetism in nickel and cobalt nanowires, very sensitive equipment is required due to their reduced dimensions. To this end, superconducting quantum interference device (SQuID) can be employed in order to make qualitative measurements for investigating the extent of magnetism in nickel and cobalt nanowires.

BIBLIOGRAPHY

1. G.E. Moore, *Cramming more components onto integrated circuits.* Electronics, 1965. **38**(8).

2. B. Ozturk, G. Behin-Aein, and B.N. Flanders, *Hard-disk behavior and beyond in Langmuir films of CdSe Nanoparticles.* Langmuir, 2005. **21**: p. 4452-4457.

3. T. Jhaveri, R. Cottle, Y. Zhang, and C. Progler, *Investigation of viable approaches to AAPSM intensity imbalance reduction for 65-nm lithography.* Proceedings of SPIE-The International Society for Optical Engineering, 2005. **5754(Pt. 2, Optical Microlithography XVIII)**: p. 978-985.

4. P. A. Packan, *Pushing the limits.* Science, 1999. **285**(5436): p. 2079,2081.

5. Y.-K. Choi L. Chang, D. Ha, P. Ranade, J. Bokor, C. Hu, T.-J. King, *Extremely Scaled Silicon Nano-CMOS Devices.* Proceedings of the IEEE, 2003. **91**(11): p. 1860-1873.

6. Y. Huang, X. Duan, Q. Wei, and C. M. Lieber, *Directed Assembly of One-Dimensional Nanostructures into Functional Networks.* Science, 2001. **291**(5504): p. 630-633.

7. Y. Cui and C. M. Lieber, *Functional nanoscale electronic devices assembled using silicon nanowire building blocks.* Science, 2001. **291**(5505): p. 851-853.

8. D. Wang, B. A. Sheriff, and J. R. Heath, *Complementary Symmetry Silicon Nanowire Logic: Power-Efficient Inverters with Gain.* Small, 2006. **2**(10): p. 1153-1158.

9. F. Patolsky, G. Zheng, and C.M. Lieber, *Nanowire-Based Biosensors.* Anal. Chem., 2006. **78**: p. 4260-4269.

10. Q. Wan, Q. H. Li, Y. J. Chen, T. H. Wang, X. L. He, J. P. Li, and C. L.Lin, *Fabrication and ethanol sensing characteristics of ZnO nanowire gas sensors.* Appl. Phys. Lett., 2004. **84**(18): p. 3654-3656.

11. M. M. J. Treacy, T. W. Ebbesen, and J. M. Gibson, *Exceptionally high Young's modulus observed for individual carbon nanotubes.* Nature, 1996. **381**: p. 678-680.

12. O. Lourie M-F Yu, M. J. Dyer, K. Moloni, T. F. Kelly, R. S. Ruoff *Strength and Breaking Mechanism of Multiwalled Carbon Nanotubes Under Tensile Load.* Science, 2000. **287**(5453): p. 637-640.

13. J. W. Mintmire, B. I. Dunlap, and C. T. White, *Are Fullerene Tubules Metallic?* Phys. Rev. Lett., 1992. **68**(5): p. 631-634.

14. R. Saito, M. Fujita, G. Dresselhaus, and M. S Dresselhaus, *Electronic structure of chiral graphene tubules.* Appl. Phys. Lett., 1992. **60**(18): p. 2204-2206.

15. C.T. White and J. W. Mintmire, *Fundamental Properties of Single-Wall Carbon Nanotubes.* J. Phys. Chem. B, 2005. **109**: p. 52-65.

16. L. Dai, *Light-emitting polymers and carbon nanotube electron emitters for optoelectronic displays.* Smart Materials and Structures, 2002. **11**(5): p. 645-651.

17. A. Bachtold, P. Hadley, T. Nakanishi, and C. Dekker, *Logic Circuits with Carbon Nanotube Transistors.* Science, 2001. **294**(5545): p. 1317-1320.

18. Z. Chen, J. Appenzeller, Y.-M. Lin, J. Sippel-Oakley, A. G. Rinzler, J. Tang, S. J. Wind, P. M. Solomon, and P. Avouris, *An Integrated Logic Circuit Assembled on a Single Carbon Nanotube* Science, 2006. **311**(5768): p. 1735.

19. M. Zhang, K. A. Atkinson, and R. H. Baughman, *Multifunctional Carbon Nanotube Yarns by Downsizing an Ancient Technology* Science, 2004. **306**(5700): p. 1358-1361.

20. M. Zhang, S. Fang, A. A. Zakhidov, S. B. Lee, A. E. Aliev, C. D. Williams, K. R. Atkinson, and R. H. Baughman, *Strong, Transparent, Multifunctional, Carbon Nanotube Sheets.* Science, 2005. **309**(5738): p. 1215-1219.

21. A. J. Rosengarta, M. D. Kaminskib, H. Chena, P. L. Cavinessa, A. D. Ebnerc, and J. A. Ritter, *Magnetizable implants and functionalized magnetic carriers: A novel approach for noninvasive yet targeted drug delivery.* Journal of Magnetism and Magnetic Materials, 2005. **293**(1): p. 633-638.

22. F. Patolsky, B. P. Timko, G. Yu, Y. Fang, A. B. Greytak, G. Zheng, and C. M. Lieber, *Detection, Stimulation, and Inhibition of Neuronal Signals with High-Density Nanowire Transistor Arrays.* . Science, 2006. **313**(5790): p. 1100-1104.

23. M. Valden, X. Lai, and D. W. Goodman, *Onset of Catalytic Activity of Gold Clusters on Titania with the Appearance of Nonmetallic Properties.* Science, 1998. **281**(5383): p. 1647-1650.

24. R. B. Dingle, *The electrical conductivity of thin wires.* Proc. Roy. Soc. London A, 1950. **201**: p. 545-560.

25. Z. Tang, B. Ozturk, Y. Wang, and N. A. Kotov, *Simple Preparation Strategy and One-Dimensional Energy Transfer in CdTe Nanoparticle Chains.* Journal of Physical Chemistry B, 2004. **108**(22): p. 6927-6931.

26. Z. Tang, N. A. Kotov, S. Magonov, and B. Ozturk, *Nanostructured artificial nacre.* Nature Materials, 2003. **2**: p. 413-418.

27. Z. Tang, N. A. Kotov, and M. Giersig, *Spontaneous Organization of Single CdTe Nanoparticles into Luminescent Nanowires* 2002, 2002. **297**(5579): p. 237-240.

28. X. M. Lin, C. M. Sorensen, and K. J. Klabunde, *Ligand-Induced Gold Nanocrystal Superlattice Formation in Colloidal Solution.* Chem. Mater., 1999. **11**(2): p. 198-202.

29. X. M. Lin, H. M. Jaeger, C. M. Sorensen, and K. J. Klabunde, *Formation of Long-Range-Ordered Nanocrystal Superlattices on Silicon Nitride Substrates.* J. Phys. Chem. B, 2001. **105**(17): p. 3353-3357.

30. T. B. Tran, I. S. Beloborodov, X. M. Lin, V. M. Vinokur, and H. M. Jaeger, *Multiple Cotunneling in Large Quantum Dot Arrays.* Phys. Rev. Lett., 2005. **95**: p. 076806.

31. B. Ozturk, C. Blackledge, D. R. Grischkowsky, and B. N. Flanders, *Reproducible interconnects assembled from gold nanorods.* Applied Physics Letters, 2006. **88**: p. 073108.

32. J. Zhang J.H. Zhang, Z.L. Wang, J. Liu, S. Chen, G.Y. Liu, *Self-Assembled Nanostructures.* 2003: Springer.

33. B. Ozturk, I. Talukdar, and B. N. Flanders, *The directed-assembly of CdS interconnects between targeted points in a circuit.* Applied Physics Letters, 2005. **86**(18): p. 183105/1-183105/3.

34. W.-X. Fang, Z.-H. He, X.-Q. Xu, Z.-Q. Mao, and H. Shen, *Magnetic-field-induced chain-like assembly structures of Fe3O4 nanoparticles.* Europhys. Lett., 2007. **77**(6): p. 68004.

35. M. F. Islam, D. E. Milkie, C. L. Kane, A. G. Yodh, and J. M. Kikkawa, *Direct Measurement of the Polarized Optical Absorption Cross Section of Single-Wall Carbon Nanotubes.* Phys. Rev. Lett., 93. **93**: p. 037404.

36. T. S. Jespersen, M. Aagesen, C. Sørensen, P. E. Lindelof, and J. Nygård, *Kondo physics in tunable semiconductor nanowire quantum dots.* Phys. Rev. B, 2006. **74**: p. 233304.

37. M. L. Tian, J. G. Wang, J. Snyder, J. Kurtz, Y. Liu, P. Schiffer, T. E. Mallouk, and M. H. W. Chan, *Synthesis and characterization of superconducting single-crystal Sn nanowires.* Appl. Phys. Lett., 2003. **83**(8): p. 1620-1622.

38. Y. Ji, A. Hoffmann, J. S. Jiang, and S. D. Bader, *Spin injection, diffusion, and detection in lateral spin-valves.* Appl. Phys. Lett., 2004. **85**(25): p. 6218.

39. X. Duan and C.M. Lieber, *General Synthesis of Compound Semiconductor Nanowires.* Adv. Mater., 2000. **12**: p. 298-302.

40. L. Hong, Z. Liu, X. T. Zhang, and S. K. Hark, *Self-catalytic growth of single-phase AlGaN alloy nanowires by chemical vapor deposition.* Appl. Phys. Lett., 2006. **89**: p. 193105-193108.

41. A. M. Morales and C. M. Lieber, *A laser ablation method for the synthesis of crystalline semiconductor nanowires.* Science, 1998. **279**(5348): p. 208-211.

42. C. C. Tang, S. S. Fan, H. Y. Dang, P. Li, and Y. M. Liu, *Simple and high-yield method for synthesizing single-crystal GaN nanowires.* Appl. Phys. Lett., 2000. **77**(13): p. 1961-1963.

43. Y. Wang, L. Zhang, C. Liang, G. Wang, and X. Peng, *Catalytic growth and photoluminescence properties of semiconductor single-crystal ZnS nanowires.* Chem. Phys. Lett., 2002. **357**(3-4): p. 314-318.

44. D. Whang, S. Jin, and C. M. Lieber, *Nanolithography Using Hierarchically Assembled Nanowire Masks.* Nano Letters, 2003. **3**(7): p. 951-954.

45. Z. L. Wang, Z. R. Dai, R. P. Gao, Z. G. Bai, and J. L. Gole, *Side-by-side silicon carbide–silica biaxial nanowires: Synthesis, structure, and mechanical properties.* Appl. Phys. Lett., 2000. **77**(21): p. 3349-3351.

46. Y. Wu and P Yang, *Direct Observation of Vapor-Liquid-Solid Nanowire Growth.* J. Am. Chem. Soc., 2001. **123**(13): p. 3165-3166.

47. Y. Xia, P. Yang, Y. Sun, Y. Wu, B. Mayers, B. Gates, Y. Yin, F. Kim, and H. Yan, *One-dimensional nanostructures: synthesis, characterization, and applications.* Adv. mater., 2003. **15**(5): p. 353-389.

48. M. B. Mohamed, Z. L. Wang, and M. A. El-Sayed, *Temperature-Dependent Size-Controlled Nucleation and Growth of Gold Nanoclusters.* J. Phys. Chem. A., 1999. **103**(49): p. 10255-10259.

49. C. B. Murray, S. Sun, W. Gaschler, H. Doyle, T. A. Betley, and . Kagan C. R, *Colloidal synthesis of nanocrystals and nanocrystal superlattices* Journal of Research and Development 2001. **45**(1): p. 47-56.

50. T. Thurn-Albrecht, J. Schotter, G. A. Kästle, N. Emley, T. Shibauchi, L. Krusin-Elbaum, K. Guarini, C. T. Black, M. T. Tuominen, and T. P. Russell, *Ultrahigh-Density Nanowire Arrays Grown in Self-Assembled Diblock Copolymer Templates* Science, 2000. **290**(5499): p. 2126-2129.

51. W. C. Ellis R. S. Wagner, *Vapor-liquid solid mechanism of single crystal growth.* Appl. Phys. Lett., 1964. **4**(5): p. 89-90.

52. C. Li, D. Zhang, S. Han, X. Liu, T. Tang, and C. Zhou, *Diameter-Controlled Growth of Single-Crystalline In2O3 Nanowires and Their Electronic Properties.* Adv. Mater., 2003. **15**(2): p. 143-146.

53. B. S. Simpkins, P. E. Pehrsson, M. L. Taheri, and R. M. Stroud, *Diameter control of gallium nitride nanowires.*

54. Jr. R. J. Barsotti, J. E. Fischer, C. H. Lee, J. Mahmood, C. K. W. Adu, P. C. Eklund, *Imaging, structural, and chemical analysis of silicon nanowires.* Appl. Phys. Lett., 2002. **81**(15): p. 2866-2868.

55. C.R. Martin M. Wirtz, *Template-Fabricated Gold Nanowires and Nanotubes.* Adv. Mater., 2003. **15**(5): p. 455-458.

56. A. Bora A. Bid, A. K. Raychaudhuri, *Temperature dependence of the resistance of metallic nanowires of diameter 15 nm: Applicability of Bloch-Grüneisen theorem.* Phys. Rev. B, 2006. **74**: p. 035426.

57. Y. Eichen E. Braun, U. Sivan, G. Ben-Yoseph, *DNA-templated assembly and electrode attachment of a conducting silver wire* Nature, 1998. **391**: p. 775-778.

58. M. Mertig J. Richter, W. Pompe, H. Vinzelberg *Low-temperature resistance of DNA-templated nanowires.* Appl. Phys. A, 2002. **74**(6): p. 725-728.

59. C. E. Flynn C. Mao, A. Hayhurst, R. Sweeney, J. Qi, G. Georgiou, B. Iverson, A. M. Belcher, *Viral assembly of oriented quantum dot nanowires.* PNAS, 2003. **100**(12): p. 6946-6951.

60. C. M. Niemeyer, *Nanoparticles, Proteins, and Nucleic Acids:Biotechnology Meets Materials Science.* Angew. Chem. Int. Ed., 2001. **40**: p. 4128-4158.

61. H. Muramatsu, K. Homma, N. Yamamoto, J. Wang, K. Sakata-Sogawa, and N. Shimamoto, *Imaging of DNA molecules by scanning near-field microscope* Mater. Sci. Eng., 2000. **12**(1-2): p. 29-32.

62. T. K. Sau D. Andreescu, D. V. Goia, *Stabilizer-free nanosized gold sols* Journal of Colloid and Interface Science 2006. **298**(2): p. 742-751.

63. S. H. Kim, G. Markovich, S. Rezvani, S. H. Choi, K. L. Wang, and J. R. Heath, *Tunnel diodes fabricated from CdSe nanocrystal monolayers.* Appl. Phys. Lett., 1999. **74**(2): p. 317-319.

64. S. I. Shopova, G. Farca, A. T. Rosenberger, W. M. S. Wickramanayake, and N. A. Kotov, *Microsphere whispering-gallery-mode laser using HgTe quantum dots.* Appl. Phys. Lett., 2004. **85**(25): p. 6101-6103.

65. C. B. Murray, D. J. Norris, and M. G. Bawendi, *Synthesis and characterization of nearly monodisperse CdE (E = sulfur, selenium, tellurium) semiconductor nanocrystallites* J. Am. Chem. Soc., 1993. **115**(19): p. 8706-8715.

66. G. Zheng, W. Lu, S. Jin, and C. M. Lieber, *Synthesis and fabrication of high-performance n-type silicon nanowire transistors.* Advanced Materials, 2004. **16**(21): p. 1890-1893.

67. C. Baur, A. Bugacov, B. E. Koel, A. Madhukar, N. Montoya, T. R. Ramachandran, A. A. G. Requicha, and P. Will R. Resch, *Nanoparticle manipulation by mechanical pushing: underlying phenomena and real-time monitoring.* Nanotechnology, 1998. **9**(4): p. 360-364.

68. J. Y. Kim C. Y. Nam, J. E. Fischer *Focused-ion-beam platinum nanopatterning for GaN nanowires: Ohmic contacts and patterned growth.* Appl. Phys. Lett., 2005. **86**: p. 193112.

69. R. Resch, A. Bugacov, C. Baur, B. E. Koel, A. Madhukar, A. A. G. Requicha, and P. Will, *Manipulation of nanoparticles using dynamic force microscopy: simulation and experiments.* Applied Physics A, 1998. **67**(3): p. 265-271.

70. B. A. Korgel T. Hanrath, *Germanium nanowire transistors: a comparison of electrical contacts patterned by electron beam lithography and beam-assisted chemical vapour deposition* Journal of Nanoengineering and Nanosystems,, 2004. **N1**: p. 25-34.

71. S.E. Mohney, Y. Wang, M.A. Cabassi, K.K. Lew, S. Dey, J.M. Redwing, and T.S. Mayer, *Measuring the specific contact resistance of contacts to semiconductor nanowires* Solid-State Electronics, 2005. **49**(2): p. 227-232.

72. J. S. Hwang, D. Ahn, S. H. Hong, H. K. Kim, S. W. Hwang, B.-H. Jeon, and J.-H. Choi, *Effect of Ti thickness on contact resistance between GaN nanowires and Ti/Au electrodes* Appl. Phys. Lett., 2004. **85**(9): p. 1636-1638.

73. M.-H. Ham, J.-H. Choi, W. Hwang, C. Park, W.-Y. Lee, and J.-M. Myoung, *Contact characteristics in GaN nanowire devices.* Nanotechnology, 2006. **17**: p. 2203-2206.

74. D. Iacopino G. De Marzi, A. J. Quinn, G. Redmond *Probing intrinsic transport properties of single metal nanowires: Direct-write contact formation using a focused ion beam.* J. Appl. Phys., 2004. **96**(6): p. 3458-3462.

75. D. Tham K. Byon, J. E. Fischer, A. T. Johnson, *Systematic study of contact annealing: Ambipolar silicon nanowire transistor with improved performance.* Appl. Phys. Lett., 2007. **90**: p. 143513-143515.

76. H. A. Pohl, *Dielectrophoresis.* 1978, Cambridge: Cambridge University Press.

77. The author is thankful to Dr. Necati Kaval and Dr. Barry Lavine for providing the polymer particles.

78. A. Bezryadin, R. M. Westervelt, and M. Tinkham, *Self-assembled chains of graphitized carbon nanoparticles.* Appl. Phys. Lett., 1999. **74**(18): p. 2699-2701.

79. K. D. Hermanson, S. O. Lumsdon, J. P. Williams, E. W. Kaler, and O. D. Velev, *Dielectrophoretic assembly of electrically functional microwires from nanoparticle suspensions.* . Science, 2001. **294**(5544): p. 1082-1086.

80. R. Kretschmer and W. Fritzsche, *Pearl Chain Formation of Nanoparticles in Microelectrode Gaps by Dielectrophoresis.* Langmuir, 2004. **20**(26): p. 11797-11801.

81. C. Cheng, R. K. Gonela, Q. Gu, and D. T. Haynie, *Self-Assembly of Metallic Nanowires from Aqueous Solution.* Nano Letters, 2005. **5**(1): p. 175-178.

82. P. Seneor, N. Lidgi, J. Carrey, H. Jaffres, F. NguyenVanDau, A. Friederich, and A. Fert, *Principle of a variable capacitor based on Coulomb blockade of nanometric-size clusters.* . Europhys. Lett., 2004. **65**(5): p. 699-704.

83. I. Talukdar, B. Ozturk, T. D. Mishima, and B. N. Flanders, *Directed growth of single-crystal indium wires.* Applied Physics Letters, 2006. **88**: p. 221907.

84. B. Ozturk, T. D. Mishima, D. R. Grischkowsky, and B. N. Flanders, *Single-Step Growth and Low Resistance Interfacing of Gold Nanowires.* Nanotechnology, 2007. **18**: p. 175707.

85. S. J. Tans, A. R. M. Verschueren, and C. Dekker, *Room-temperature transistor based on a single carbon nanotube.* Nature, 1998. **393**: p. 49-52.

86. R. Martel, T. Schmidt, H. R. Shea, T. Hertel, and Ph. Avouris, *Single- and multi-wall carbon nanotube field-effect transistors.* Appl. Phys. Lett., 1998. **73**(17): p. 2447-2449.

87. S. H. Kim, G. Markovich, S. Rezvani, S. H. Choi, K. L. Wang, and J. R. Heath, *Tunnel diodes fabricated from CdSe nanocrystal monolayerrs.* Appl. Phys. Lett., 1999. **74**(2): p. 317-319.

88. Y. Huang, X. Duan, Q. Wei, and C. M. Lieber, *Directed assembly of one-dimensional nanostructures into functional networks.* Science, 2001. **291**: p. 630-633.

89. Y. Huang, X. Duan, Y. Cui, L. J. Lauhon, K. Kim, and C. M. Lieber, *Logic gates and computation from assembled nanowire building blocks.* Science, 2001. **294**: p. 1313-1317.

90. P. He, N. Hu, and J. F. Rusling, *Driving forces for layer-by-layer self-assembly of films of SiO_2 nanoparticles and heme proteins.* Langmuir, 2004. **20**(3): p. 722-729.

91. S. I. Shopova, G. Farca, A. T. Rosenberger, W. M. S. Wickramanayake, and N. A. Kotov, *Microsphere whispering-gallery-mode laser using HgTe quantum dots.* Appl. Phys. Lett., 2004. **85**: p. 6101-6103.

92. A. L. Rogach, D. S. Koktysh, M. Harrison, and N. A. Kotov, *Layer-by-layer assembled films of HgTe nanocrystals with strong infrared emission.* Chem. Mater., 2002. **12**: p. 1526-1528.

93. K. D. Hermanson, S. O. Lumsdon, J. P. Williams, E. W. Kaler, and O. D. Velev, *Dielectrophoretic assembly of electrically functional microwires from nanoparticle suspensions.* Science, 2001. **294**: p. 1082-1086.

94. X. Duan, Y. Huang, Y. Cui, J. Wang, and C. M. Lieber, *Indium phosphide nanowires as building blocks for nanoscale electronic and optoelectronic devices.* Nature, 2001. **409**: p. 66-69.

95. S. A. Blanton, R. L. Leheny, M. A. Hines, and P. Guyot-Sionnest, *Dielectric dispersion measurements of CdSe nanocrystal colloids: observation of a permanent dipole moment.* Phys. Rev. Lett., 1997. **79**(5): p. 865-868.

96. M. Shim and P. Guyot-Sionnest, *Permanent dipole moment and charges in colloidal semiconductor quantum dots.* J. Chem. Phys, 1999. **111**(15): p. 6955-6964.

97. K. H. Bhatt and O. D. Velev, *Control and modeling of the dielectrophoretic assembly of on-chip nanoparticle wires.* Langmuir, 2004. **20**: p. 467-476.

98. B. Ozturk, I. Talukdar, and B. N. Flanders, *The self-assembly of CdS interconnects between targeted points in a circuit.* Submitted to Appl. Phys. Lett., 2004.

99. C. Cheng, R. K. Gonela, Q. Gu, and D. T. Haynie, *Self-assembly of metallic nanowires from aqueous solution.* Nano Lett., 2005. **5**(1): p. 175-178.

100. W. M. Gelbart, R. P. Sear, J. R. Heath, and S. Chaney, *Array formation in nano-colloids: theory and experiment in 2D.* Faraday Discuss., 1999. **112**: p. 299-307.

101. X. M. Lin, H. M. Jaeger, C. M. Sorensen, and K. J. Klabunde, *Formation of long-range-ordered nanocrystal superlattices on silicon nitride substrates.* J. Phys. Chem. B, 2001. **105**: p. 3353-3357.

102. R. Parthasarathy, X. Lin, and H. M. Jaeger, *Electronic transport in metal nanocrystal arrays: the effect of structural disorder on scaling behavior.* Phys. Rev. Lett., 2001. **87**(18): p. 186807.

103. R. Parthasarathy, X. Lin, K. Elteto, T. F. Rosenbaum, and H. M. Jaeger, *Percolating through networks of random thresholds: finite temperature electron tunneling in metal nanocrystal arrays.* Phys. Rev. Lett., 2004. **92**(7): p. 076801.

104. T. D. Krauss and L. E. Brus, *Charge, polarizability, and photoionization of single semiconductor nanocrystals.* Phys. Rev. Lett., 1999. **83**(23): p. 4840-4843.

105. Z. Tang, N. A. Kotov, and M. Giersig, *Spontaneous organization of single CdTe nanoparticles into luminescent nanowires.* Science, 2002. **297**: p. 237-240.

106. I. A. Greene, F. Wu, J. Z. Zhang, and S. Chen, *Electronic conductivity of semiconductor nanoparticle monolayers at the air|water interface.* J. Phys. Chem. B, 2003. **107**: p. 5733-5739.

107. Y. Tian and J. H. Fendler, *Langmuir-Blodgett Film Formation from Fluorescence-Activated, Surfactant-Capped, Size-Selected CdS Nanoparticles Spread on Water Surfaces.* Chem. Mater., 1996. **8**: p. 969-974.

108. D. Chandler, *Introduction to Modern Statistical Mechanics*. 1987, New York: Oxford University Press.

109. H. Shiku and R. C. Dunn, *Near-field scanning optical microscopy studies of dipalmitoylphosphatidylcholine monolayers at the air-liquid interface.* J. Microscopy, 1998. **194**: p. 461-466.

110. V. M. Kaganer, H. Möhwald, and P. Dutta, *Structure and phase transitions in Langmuir monolayers.* Rev. Mod. Phys., 1999. **71**(3): p. 779-819.

111. K. Y. C. Lee, J. Majewski, T. L. Kuhl, P. B. Howes, K. Kjaer, M. M. Lipp, A. J. Waring, J. A. Zasadzinski, and G. S. Smith, *Synchrotron x-ray study of lung surfactant-specific protein SP-B in lipid monolayers.* Biophys. J., 2001. **81**: p. 572-585.

112. D. Poupinet, R. Vilanove, and F. Rondelez, *Molecular weight dependence of the second virial coefficient for flexible polymer chains in two dimensions.* Macromolecules, 1989. **22**: p. 2491-2496.

113. Z. A. Peng and X. Peng, *Formation fo high-quality CdTe, CdSe, and CdS nanocrystals using CdO as precursor.* J. Am. Chem. Soc., 2001. **123**: p. 183-184.

114. L. Qu, Z. A. Peng, and X. Peng, *Alternative routes toward high quality CdSe nanocrystals.* Nano Lett., 2001. **1**(6): p. 333-337.

115. C. B. Murray, D. J. Norris, and M. G. Bawendi, *Synthesis and characterization of nearly monodisperse CdE (E = S, Se, Te) semiconductor nanocrystallites.* J. Am. Chem. Soc., 1993. **115**: p. 8706-15.

116. W. Yu, L. Qu, W. Guo, and X. Peng, *Experimental determination of the size dependent extinction coefficients of high quality CdTe, CdSe and CdS nanocrystals.* Chem. Mater., 2003. **15**: p. 2845-2852.

117. W. W. Yu, L. Qu, W. Guo, and X. Peng, *Erratum: Experimental determination of the extinction coefficient of CdTe, CdSe, and CdS nanocrystals.* Chem. Mater., 2004. **16**: p. 560.

118. D. Henderson, *A simple equation of state for hard discs.* Molec. Phys., 1975. **30**(3): p. 971-972.

119. E. J. JansevanRensburg, *Virial coefficients for hard discs and hard spheres.* J. Phys. A, 1993. **26**: p. 4805-4818.

120. B. J. Ackerson, X. L. Lei, and P. Tong, *Subtle order in settling suspensions.* Pure Appl. Chem., 2001. **73**(11): p. 1679-1688.

121. X. M. Lin, C. M. Sorensen, and K. J. Klabunde, *Ligand-induced gold nanocrystal supperlattice formation in colloidal solution.* Chem. Mater., 1999. **11**: p. 198-202.

122. A. Bachtold, P. Hadley, T. Nakanishi, and C. Dekker, *Logic circuits with carbon nanotube transistors.* Science, 2001. **294**: p. 1317-1320.

123. A. Bezryadin and C. Dekker, *Electrostatic trapping of single conducting nanoparticles between nanoelectrodes.* Appl. Phys. Lett., 1997. **71**(9): p. 1273-1275.

124. I. Amlani, A. M. Rawlett, L. A. Nagahara, and R. K. Tsui, *An approach to transport measurements of electronic molecules.* Appl. Phys. Lett., 2002. **80**(15): p. 2761-2763.

125. A. Bezryadin, R. M. Westervelt, and M. Tinkham, *Self-assembled chains of graphitized carbon nanoparticles.* Appl. Phys. Lett., 1999. **74**(18): p. 2699-2701.

126. M. Shim and P. Guyot-Sionnest, *n-type colloidal semiconductor nanocrystals.* Nature, 2000. **407**: p. 981-983.

127. M. Shim and P. Guyot-Sionnest, *Organic-capped ZnO nanocrystals: synthesis and n-type character.* J. Am. Chem. Soc., 2001. **123**: p. 11651-11654.

128. Y. Yang, J. Shi, H. Chen, S. Dai, and Y. Liu, *Enhanced off-resonant optical nonlinearity of Au-CdS core-shell nanoparticles embedded in $BaTiO_3$ thin films.* Chem. Phys. Lett., 2003. **370**(1): p. 1-6.

129. L. E. Brus, *Electron-electron and electron-hole interactions in small semiconductor crystallites: The size dependence of the lowest excited electronic state.* J. Chem. Phys., 1984. **80**(9): p. 4403-4409.

130. J. E. Stangroom, *Electrorheological fluids.* Phys. in Technol., 1983. **14**: p. 290-296.

131. T. C. Halsey and W. Toor, *Structure of electrorheological fluids.* Phys. Rev. Lett., 1990. **65**(22): p. 2820-2823.

132. P. G. deGennes and P. A. Pincus, *Pair correlations in a ferromagnetic colloid.* Phys. Kondens. Materie, 1970. **11**: p. 189-198.

133. P. C. Jordan, *Association phenomena in a ferromagnetic colloid.* Molec. Phys., 1973. **25**(4): p. 961-973.

134. J. Israelachvili, *Intermolecular & Surface Forces*. 1992, London: Academic Press.

135. A. Chaudhari, N. M. more, and S. C. Mehrotra, *Static dielectric constant and relaxation time for the binary mixture of water, ethanol, N,N-dimethylformamide, dimethylsulphoxide, and N,N dimethylacetamide with 2-methoxyethanol.* Bull. Korean Chem. Soc., 2001. **22**(4): p. 357-361.

136. L. A. Nagahara, I. Amlani, J. Lewenstein, and R. K. Tsui, *Directed placement of suspended carbon nanotubes for nanometer-scale assembly.* Appl. Phys. Lett., 2002. **80**(20): p. 3826-3828.

137. R. Kretschmer and W. Fritzsche, *Pearl chain formation of nanoparticles in microelectrode gaps by dielectrophoresis.* Langmuir, 2004. **20**: p. 11797-11801.

138. B. Ozturk, I. Talukdar, and B. N. Flanders, *The directed-assembly of CdS interconnects between targeted points in a circuit.* Appl. Phys. Lett., 2005. **86**: p. 183105.

139. T. K. Sau and C. J. Murphy, *Seeded High Yield Synthesis of Short Au Nanorods in Aqueous Solution.* Langmuir, 2004. **20**: p. 6414-6420.

140. M. B. Mohamed, Z. L. Wang, and M. A. El-Sayed, *Temperature-dependent size-controlled nucleation and growth of gold nanoclusters.* J. Phys. Chem. A, 1999. **103**: p. 10255-10259.

141. I. Giaever and H. R. Zeller, *Superconductivity of small tin particles measured by tunneling.* Phys. Rev. Lett., 1968. **20**: p. 1504-1507.

142. J. Lambe and R. C. Jaklevic, *Charge quantization studies using a tunnel capacitor.* Phys. Rev. Lett., 1969. **22**: p. 1371-1375.

143. T. Kleimann, M. Sassetti, B. Kramer, and A. Yacoby, *Charge and spin addition energies of a one-dimensional quantum dot.* Phys. Rev. B, 2000. **62**(12): p. 8144-8153.

144. J. G. Hou, B. Wang, J. Yang, X. R. Wang, Q. Zhu, and X. Xiao, *Nonclassical behavior in the capacitance of a nanojunction.* Phys. Rev. Lett., 86. **86**(23): p. 5321-5324.

145. D. Yu, C. Wang, B. L. Wehrenberg, and P. Guyot-Sionnest, *Variable range hopping conduction in semiconductor nanocrystal solids.* Phys. Rev. Lett., 2004. **92**(21): p. 216802.

146. M. Amman, R. Wilkins, E. Ben-Jacob, P. D. Maker, and R. C. Jaklevic, *Analytic solution for the current-voltage characteristic of two mesoscopic tunnel junctions coupled in series.* Phys. Rev. B, 1991. **43**(1): p. 1146-1149.

147. P. Seneor, N. Lidgi, J. Carrey, H. Jaffres, F. NguyenVanDau, A. Friederich, and A. Fert, *Principle of a variable capacitor based on Coulomb blockade of nanometric-size clusters.* Europhys. Lett., 2004. **65**(5): p. 699-704.

148. J. Tang, B. Gao, H. Geng, O. D. Velev, L. C. Qin, and O. Zhou, *Assembly of 1D nanostructures into sub-micrometer diameter fibrils with controlled and variable length by dielectrophoresis.* Adv. Mater., 2003. **15**(15): p. 1352-1355.

149. K. G. Libbrecht and V. M. Tanusheva, *Electrically induced morphological instabilities in free dendritic growth.* Phys. Rev. Lett., 1998. **81**(1): p. 176-179.

150. B. Ozturk, C. Blackledge, D. R. Grischkowsky, and B. N. Flanders, *Reproducible interconnects assembled from gold nanorods.* Appl. Phys. Lett., 2006. **88**: p. 073108.

151. Y. Sawada, A. Dougherty, and J. P. Gollub, *Dendritic and fractal patterns in electrolytic metal deposits.* Phys. Rev. Lett., 1986. **56**(12): p. 1260-1263.

152. D. Grier, E. Ben-Jacob, R. Clarke, and L. M. Sander, *Morphology and microstructure in electrochemical deposition of zinc.* Phys. Rev. Lett., 1986. **56**(12): p. 1264-1267.

153. H. E. Swanson, R. K. Fuyat, and G. M. Ugrinic, *Data for 34 inorganic substances.* National Bureau of Standards Circular 539, 1954. **3**: p. 3.

154. A. Zangwill, *Physics at Surfaces*. 1988, New York: Cambridge University Press.

155. J. C. Heyraud and J. J. Métois, *Surface free energy anisotropy measurement of indium.* Surface Science, 1986. **177**: p. 213-220.

156. J. S. Langer, *Instabilities and pattern formation in crystal growth.* Rev. Mod. Phys., 1980. **52**(1): p. 1-28.

157. K. G. Libbrecht and V. M. Tanusheva, *Cloud chambers and crystal growth: effects of electrically enhanced diffusion on dendrite formation formation from neutral molecules.* Phys. Rev. E, 1999. **59**: p. 3253-3261.

158. M. E. Glicksman and A. O. Lupulescu, *Dendritic crystal growth in pure materials.* J. Crystal Growth, 2004. **264**: p. 541-549.

159. W. G. Miao, Y. Wu, and H. P. Zhou, *Morphologies and growth mechanisms of aluminum nitride whiskers.* J. Mater. Sci., 1997. **32**: p. 1969-1975.

160. A. M. Morales and C. M. Lieber, *A laser ablation method for the synthesis of crystalline semiconductor nanowires.* Science, 1998. **279**: p. 208-211.

161. J. Vancea, H. Hoffmann, and K. Kastner, *Mean free path and effective density of conduction electrons in polycrystalline metal films.* Thin Solid Films, 1984. **121**: p. 201-216.

162. R. B. Dingle, *The electrical conductivity of thin wires.* Proc. Roy. Soc. A, 1950. **201**(1067): p. 545-560.

163. E. R. Andrew, *The size-variation of resistivity for mercury and tin.* Proc. Phys. Soc. A, 1949. **62**(2): p. 77-88.

164. C. Kittel, *Introduction to Solid State Physics*. 7th ed. 1996, New York: John Wiley & Sons.

165. C. Durkan and M. E. Welland, *Size effects in the electrical resistivity of polycrystalline nanowires.* Phys. Rev. B, 2000. **61**(20): p. 14215.

166. P. A. Smith, C. D. Nordquist, T. N. Jackson, T. S. Mayer, B. R. Martin, J. Mbindyo, and T. E. Mallouk, *Electric-field assisted assembly and alignment of metallic nanowires.* Appl. Phys. Lett., 2000. **77**(9): p. 1399-1401.

167. M. E. T. Molares, E. M. Höhberger, C. Schaeflein, R. H. Blick, R. Neumann, and C. Trautmann, *Electrical characterization of electrochemically grown single copper nanowires.* Appl. Phys. Lett., 2003. **82**(13): p. 2139-2141.

168. G. DeMarzi, D. Iacopino, A. J. Quinn, and G. Redmond, *Probing intrinsic transport properties of single metal nanowires: direct-write contact formation using a focused ion beam.* Appl. Phys. Lett., 2004. **96**(6): p. 3458-3462.

169. M. Tian, N. Kumar, S. Xu, J. Wang, J. S. Kurtz, and M. H. W. Chan, *Supression of superconductivity in zinc nanowires by bulk superconductors.* Phys. Rev. Lett., 2005. **95**: p. 076802.

170. M. Tian, J. Wang, J. S. Kurtz, Y. Liu, M. H. W. Chan, T. S. Mayer, and T. E. Mallouk, *Dissipation in quasi-one-dimensional superconducting single-crystal Sn nanowires.* Phys. Rev. B, 2005. **71**: p. 104521.

171. R. S. Wagner and W. C. Ellis, *Vapor-liquid-solid mechanisms of single crystal growth.* Appl. Phys. Lett., 1964. **4**(5): p. 89-90.

172. Y. Wu and P. Yang, *Direct observation of vapor-liquid-solid nanowire growth.* J. Am. Chem. Soc., 2001. **123**: p. 3156-3166.

173. Z. L. Wang, Z. R. Dai, R. P. Gao, Z. G. Bai, and J. L. Gole, *Side-by-side silicon carbide-silica biaxial nanowires: synthesis, structure, and mechanical properties.* Appl. Phys. Lett., 2000. **77**(21): p. 3349-3351.

174. X. Duan and C. M. Lieber, *General synthesis of compound semiconductor nanowires.* Adv. Mater., 2000. **12**(4): p. 298-302.

175. Y. Wang, L. Zhang, C. Liang, G. Wang, and X. Peng, *Catalytic growth and photoluminescence properties of semiconductor single-crystal ZnS nanowires.* Chem. Phys. Lett., 2002. **357**: p. 314-318.

176. L. Hong, Z. Liu, X. T. Shang, and S. K. Hark, *Self-catalytic growth of single-phase AlGaN alloy nanowires by chemical vapor deposition.* Appl. Phys. Lett., 2006. **89**: p. 193105.

177. M. H. Huang, S. Mao, H. Feick, H. Yan, Y. Wu, H. Kind, E. Weber, R. Russo, and P. Yang, *Room-temperature ultraviolet nanowire nanolasers.* Science, 2001. **292**: p. 1897-1899.

178. J. Goldberger, A. I. Hochbaum, R. Fan, and P. Yang, *Silicon vertically integrated nanowire field effect transistors.* Nano Lett., 2006. **6**(5): p. 973-977.

179. Y. Cui, L. J. Lauhon, M. S. Gudiksen, J. Wang, and C. M. Lieber, *Diameter-controlled synthesis of single-crystal silicon nanowires.* Appl. Phys. Lett., 2001. **78**(15): p. 2214-2216.

180. Y. Wu, Y. Cui, L. Huynh, C. J. Barrelet, D. C. Bell, and C. M. Lieber, *Controlled growth and structures of molecular-scale silicon nanowires.* Nano Lett., 2004. **4**(3): p. 433-436.

181. V. Schmidt, S. Senz, and U. Gösele, *Diameter-dependent growth direction of epitaxial silicon nanowires.* Nano Lett., 2005. **5**(5): p. 931-935.

182. M. Wirtz and C. R. Martin, *Template-fabricated gold nanowires and nanotubes.* Adv. Mater., 2003. **15**(3).

183. T. C. Wong, C. P. Li, R. Q. Zhang, and S. T. Lee, *Gold nanowires from silicon nanowire templates.* Appl. Phys. Lett., 2004. **84**(3): p. 407-409.

184. R. Takahashi and T. Ishiwatari, *Preparation of helical gold nanowires on surfactant tubules.* Chemical Communications, 2004. **12**: p. 1406-1407.

185. J. Zhang, J. Du, B. Han, Z. Liu, T. Jiang, and Z. Zhang, *Sonochemical formation of single-crystalline gold nanobelts.* Angew. Chem. Int. Ed. , 2006. **45**: p. 1116-1119.

186. J. Shi, Y. F. Lu, K. J. Yi, Y. S. Lin, S. H. Liou, J. B. Hou, and X. W. Wang, *Direct synthesis of single-walled carbon nanotubes bridging metal electrodes by laser-assisted chemical vapor deposition.* Appl. Phys. Lett., 2006. **89**: p. 083105.

187. D. Whang, S. Jin, Y. Wu, and C. M. Lieber, *Large-scale hierarchical organization of nanowire arrays for integrated nanosystems.* Nano Lett., 2003. **3**(9): p. 1255-1259.

188. S. Jin, D. Whang, M. C. McAlpine, R. S. Friedman, Y. Wu, and C. M. Lieber, *Scalable interconnection and integration of nanowire devices without registration.* Nano Lett., 2004. **4**(5): p. 915-919.

189. J. Goldberger, A. I. Hochmaum, R. Fan, and P. Yang, *Silicon vertically integrated nanowire field effect transistors.* Nano Lett., 2006. **6**(5): p. 973-977.

190. I. Talukdar, B. Ozturk, T. D. Mishima, and B. N. Flanders, *Directed growth of single crystal indium wires.* Appl. Phys. Lett., 2006. **88**: p. 221907.

191. B. Ozturk, T. Mishima, D. R. Grischkowsky, and B. N. Flanders, *Single step growth and low resistance interconnecting of gold nanowires.* Nanotechnology, 2007. **18**: p. 175707.

192. W. W. Bentley and W. J. Humphries, *Snow Crystals*. 1931, New York: McGraw-Hill.

193. R. D. Doherty, *Dendritic Growth*, in *Crystal Growth*, B. R. Pamplin, Editor. 1975, Pergamon Press: New York.

194. D. K. Tschernoff, *Investigations on the structure of cast ingots.* Proc. Inst. Mech. Engrs., 1880.

195. H. S. Hele-Shaw, *The flow of water.* Nature, 1898. **58**: p. 34-36.

196. L. J. Paterson, *Radial fingering in a Hele Shaw cell.* Fluid Mechanics, 1981. **113**: p. 513-529.

197. D. A. Kessler, J. Koplik, and H. Levine, *Pattern selection in fingered growth phenomena.* Adv. Phys., 1988. **37**(3): p. 255-339.

198. L. J. Paterson, *Diffusion-limited aggregation and two fluid displacements in porous media.* Phys. Rev. Lett., 1984. **52**: p. 1621-1625.

199. G. P. Ivantsov, *Temperature field around spherical, cylindrical and needle-shaped crystals which grow in supercooled melt.* Dokl. Akad. Nauk USSR, 1947. **58**: p. 567.

200. S. C. Huang and M. E. Glicksman, *Fundamentals of dendritic solidification.* Acta Metall., 1981. **29**: p. 701-715.

201. M. Muschol, D. Liu, and H. Z. Cummins, *Surface-tension-anisotropy measurements of succinonitrile and pivalic acid: Comparison with microscopic solvability theory.* Phys. Rev. A, 1992. **46**(2): p. 1038-1050.

202. J. P. Franck and J. Jung, *Dendritic crystal growth in pure helium-4.* J. Low Temp. Phys., 1986. **64**: p. 165-186.

203. J. M. Liu, *In-Situ observations of dendritic growth of ammonium chloride crystals from an aqueous solution system.* Scripta Metal. Mat., 1995. **32**(3): p. 445-450.

204. A. Dougherty and J. P. Gollub, *Steady-state dendritic growth of NH_4Br from solution.* Phys. Rev. A, 1988. **38**(6): p. 3043-3053.

205. E. Ben-Jacob and P. Garik, *The formation of patterns in non-equilibrium growth.* Nature, 1990. **343**: p. 523-530.

206. E. Ben-Jacob, N. D. Goldenfield, B. G. Kotliar, and J. S. Langer, Phys. Rev. Lett., 1984. **53**: p. 2110-2113.

207. E. Brener, *Needle-crystal solution in three-dimensional dendritic growth.* Phys. Rev. Lett., 1993. **71**: p. 3653.

208. R. C. Brower, *Geometrical models of interface evolution.* Phys. Rev. A, 1984. **29**: p. 1335.

209. J. D. Jackson, *Classical Electrodynamics*. 1999, New York: John Wiley & Sons.

210. J. S. Langer and H. Müller-Krumbhaar, *Theory of dendritic growth-I. Elements of a stability analysis.* Acta Metallurgica, 1978. **26**: p. 1681-1687.

211. E. A. Brener and V. I. Mel'nikov, *Pattern selection in two-dimensional dendritic growth.* Adv. Phys., 1991. **40**(1): p. 53-97.

212. K. G. Libbrecht, T. Crosby, and M. Swanson, *Electrically enhanced free dendrite growth in polar and non-polar systems.* J. Crystal Growth, 2002. **240**: p. 241-254.

213. N. Ibl, *Some theoretical aspects of pulse electrolysis.* Surface Tech., 1980. **10**: p. 81-104.

214. Y. Saito, G. Goldbeck-Wood, and H. Müller-Krumbhaar, *Dendritic crystallization:numerical study of the one-sided model.* Phys. Rev. Lett., 1987. **58**(12): p. 1541-1543.

215. T. Ihle and H. Müller-Krumbhaar, *Diffusion-limited fractal growth morphology in thermodynamical teo-phase systems.* Phys. Rev. Lett., 1993. **70**(20): p. 3083-3086.

216. D. R. Lide, ed. *Handbook of Chemistry and Physics*. 74th ed. 1994, The Chemical Rubber Publishing Company: Boca Raton.

217. N. N. Greenwood and A. Earnshaw, *Chemistry of the Elements*. 1984, New York: Pergamon.

218. N. A. Kouklin, W. E. Kim, A. D. Lazareck, and J. M. Xu, *Carbon nanotube probes for single-cell experimentation and assays.* Appl. Phys. Lett., 2005. **87**: p. 173901.

219. I. Obataya, C. Nakamura, S. W. Han, N. Nakamura, and J. Miyake, *Nanoscale operation of a living cell using an atomic force microscope with a nanoneedle.* Nano Lett., 2005. **5**: p. 27-30.

220. C. A. Thomas, P. A. Springer, G. E. Loeb, Y. Berwald-Netter, and L. M. Okun, *A miniature microelectrode array to monitor the bioelectric activity of cultured cells.* Exp. Cell Res., 1972. **74**: p. 61-66.

221. J. Pine, *Recording action potentials from cultured neurons with extracellular microcircuit electrodes.* J. Neuroscience Meth., 1980. **2**: p. 19-31.

222. G. W. Gross, W. Y. Wen, and J. W. Lin, *Transparent indium-tin oxide electrode patterns for extracellular, multisite recording in neuronal cultures.* J. Neurosci. Meth., 1985. **15**: p. 243-252.

223. B. D. Chithrani, A. A. Ghazani, and W. C. W. Chan, *Determining the size and shape dependence of gold nanoparticle uptake into mammalian cells.* Nano Lett., 2006. **6**(4): p. 662-668.

224. N. L. Rosi, D. A. Giljohann, C. S. Thaxton, A. K. R. Lytton-Jean, M. S. Han, and C. A. Mirkin, *Oligonucleotide-modified gold nanoparticles for intracellular gene regulation.* Science, 2006. **312**: p. 1027-1030.

225. F. Patolsky, B. P. Timko, G. Yu, Y. Fang, A. B. Greytak, G. Zhang, and C. M. Lieber, *Detection, stimulation, and inhibition of neuronal signals with high-density nanowire transistor arrays.* Science, 2006. **313**: p. 1100-1104.

226. A. L. Schmitt, M. J. Bierman, D. Schmeisser, F. J. Himpsel, and S. Jin, *Synthesis and properties of single-crystla FeSi nanowires.* Nano Lett., 2006. **6**(8): p. 1617-1621.

227. R. C. Dynes and J. P. Garno, *Metal-insulator transition in granular aluminum.* Phys. Rev. Lett., 1981. **46**(2): p. 137-140.

228. M. Reghu, Y. Cao, D. Moses, and A. J. Heeger, *Counterion-induced processibility of polyaniline: Transport at the metal-insulator boundary.* Phys. Rev. B, 1993. **47**(4): p. 1758-1764.

229. R. B. Dingle, *The electrical conductivity of thin wires.* Proc. Roy. Soc. London A, 1950. **201**(1067): p. 545-560.

230. J. E. Keithley, *Low Level Measurements Handbook*. 2002, Cleveland: Keithley Instruments.

231. J. M. Ziman, *Electrons and Phonons*. 1960, Oxford: Clarendon Press.

232. J. R. Sambles, K. C. Elsom, and D. J. Jarvis, *The Electrical Resistivity of Gold Films.* Phil. Trans. R. Soc. A, 1982. **304**(1486): p. 365-396.

233. P. M. Th. M. van Attekum, P. H. Woerlee, G. C. Verkade, and A. A. M. Hoeben, *Influence of grain boundaries and surface Debye temperature on the electrical resistance of thin gold films.* Phys. Rev. B, 1984. **29**(2): p. 645-651.

234. R. C. Munoz, G. Vidal, G. Kremer, L. Moraga, C. Arenas, and A. Concha, *Surface roughness and surface-induced resistivity of gold films on mica: influence of roughness modelling.* J. Phys. Cond. Mat., 2000. **12**: p. 2903-2912.

235. J. Ederth, L. B. Kish, A. Olsson, and C. G. Granqvist, *Temperature dependent electrical resistivity in nanocrystalline gold films made by advanced gas deposition.* J. Appl. Phys., 2000. **88**(11): p. 6578-6582.

236. W. Zhang, S. H. Brongersma, O. Richard, B. Brijs, R. Palmans, L. Froyen, and K. Maex, *Influence of the electron mean free path on the resistivity of thin metal films.* Microelectronic Engineering, 2004. **76**: p. 146-152.

237. C. Durkan and M. E. Wellend, *Size effects in the electrical resistivity of polycrystalline nanowires.* Phys. Rev. B, 2000. **61**: p. 14215-14218.

238. A. Bid, A. Bora, and A. K. Raychaudhuri, *Temparature dependence of resistance of metallic nanowires of diameter > 15 nm: Applicability of Bloch-Gruneisen theorem.* Phys. Rev. B, 2006. **74**: p. 035426-035434.

239. E. J. Menke, M. A. Thompson, C. Xiang, L. C. Yang, and R. M. Penner, *Lithographically patterned nanowire electrodeposition.* Nature Materials, 2006. **5**: p. 914-919.

240. B. Ozturk, I. Talukdar, and B. N. Flanders, *Directed growth of diameter-tunable nanowires.* . Nanotechnology, 2007. **In Press**.

APPENDIX I

RESISTANCE OF TAPERED ELECTRODES

A derivation of Equation (VI.1), the expression for the resistance of a tapered electrode, is provided in this appendix. We calculate the resistance of the tapered electrodes, R_{ER} and R_{EL} as follows. A scaled diagram of a tapered electrode is depicted in Figure A1a. The untapered conducting lines have a width $2W$ of 120 μm, and the taper occurs over distance L of 250 μm, such that the width linearly decreases from 120 μm to a tip-width of 1.5 μm. The resistance per length r_0 of the untapered portion of the electrodes is 0.010 Ω/μm. However, because the cross-sectional area A of a line decreases as it tapers, its resistance increases, in accordance with the formula $R(x) = \rho l/A(x)$, where x is defined in Figure A1a, and $A(x) = w(x)t$, where $w(x)$ is the width of the electrode and t is its thickness, which we assume to be constant. The lines taper linearly, so $w(x)$ varies with a slope of $m = W/L$. Therefore, the width of the electrode at any given position x along the taper is

$$w(x) = 2mx\,. \tag{A1}$$

$R(x)$ is inversely proportional to $w(x)$, so the resistance per length $r(x)$ at any point x along the taper is

$$r(x) = r_0 \frac{2W}{w(x)}\,, \tag{A2}$$

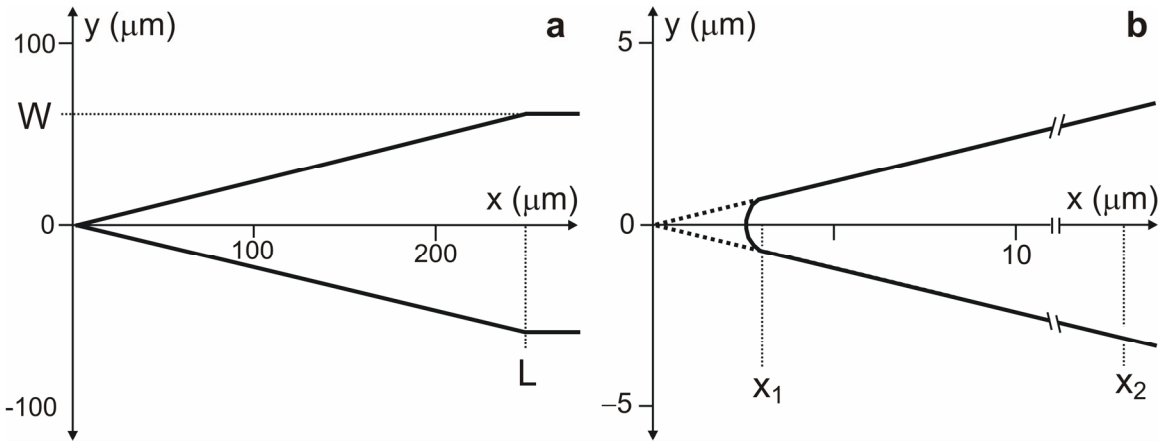

Figure A1: (a) Diagram of the electrode geometry, showing the uniformly wide conducting line tapering to a sharp tip. (b) An expanded view of the tip region of the electrode. The dashed line denotes the profile of a perfectly sharp tip, while the solid line designates the blunter profile of an actual tip.

where r_0 = 0.010 Ω/μm. We obtain the resistance R_E of the electrode region that exists between the microprobe and wire contact points by integrating Equation (A2) over the electrode length of interest:

$$R_E = \int_{x_1}^{x_2} r(x)dx\,, \tag{A3}$$

where x_1 and x_2 are the positions at which the nanowire and the microprobe make contact with the electrodes, respectively. On substitution of Equations (A1) and (A2) into Equation (A3), the electrode resistance is found to be

$$R_E = r_0 L \ln\left(\frac{x_2}{x_1}\right). \tag{A4}$$

It should be noted that because the tips taper to a finite width of 1.5 μm, x_1 is at least 3.1 μm, so Equation (A.4) is never divergent; as Figure A1b shows, this minimum value is the horizontal distance from the electrode position where the width is 1.5 μm to the theoretical apex of a perfectly sharp tip. In practice, x_1 and x_2 are determined by optical microscopy.

VITA

Birol Ozturk

Candidate for the Degree of

Doctor of Philosophy

Thesis: STRUCTURAL AND TRANSPORT PROPERTIES OF DIRECTLY ASSEMBLED NANOWIRES

Major Field: Photonics

Biographical:

Personal Data: Born in Samsun, Turkey, on March 1, 1975, the son of Ramazan and Melahat Öztürk

Education: Received Bachelor of Science degree in Physics from Bogazici University, Istanbul, Turkey in July 1999; received a Master of Science degree in Natural and Applied Science from Oklahoma State University, Stillwater, Oklahoma in December 2003. Completed the requirements for the Doctor of Philosophy degree with a major in Photonics at Oklahoma State University in July, 2007.

Experience: Employed by Oklahoma State University, Department of Physics as a graduate research assistant and graduate teaching assistant August 2000 to present.

Professional Membership: American Physical Society

Name: Birol Ozturk Date of Degree: July, 2007

Institution: Oklahoma State University Location: Stillwater, Oklahoma

Title of Study: STRUCTURAL AND TRANSPORT PROPERTIES OF DIRECTLY ASSEMBLED NANOWIRES

Pages in Study: 170 Candidate for the Degree of Doctor of Philosophy

Major Field: Photonics

Scope and Method of Study: In this work, we present a systematic study on the assembly and characterization of nanostructures. We employed self and directed assembly methods in order to organize nanostructures. Quantitative film balance studies of self-assembled semiconductor nanoparticles enabled the determination of their effective interparticle potential. As a directed-assembly method, dielectrophoresis was used in the fabrication of interconnects from dispersions of nanostructures between targeted points in external circuitry. Directed electrochemical nanowire assembly (DENA) was developed and used in the fabrication of metallic nanowires from simple salt solutions. The structural and charge transport properties of the assembled nanostructures and the DENA-grown nanowires were characterized.

Findings and Conclusions: The CdSe nanoparticles of a given diameter were found to behave like hard-disks with significantly smaller diameters. This behavior was attributed to an attractive contribution to the interparticle potential, such as the dipolar potential. We found that nanoparticulate CdS converts to bulk CdS during dielectrophoretic interconnect fabrication. We demonstrated that the dielectrophoretic interconnects fabricated from gold nanorods are nanostructured, limiting their conductivity. DENA technique enabled the single-step growth and low-resistance interconnecting of crystalline diameter-tunable metallic nanowires. The preliminary results of the diameter-dependent resistivity studies with the DENA-grown gold nanowires were consistent with the predicted behavior.

Advisor's Approval: Dr. Bret N. Flanders